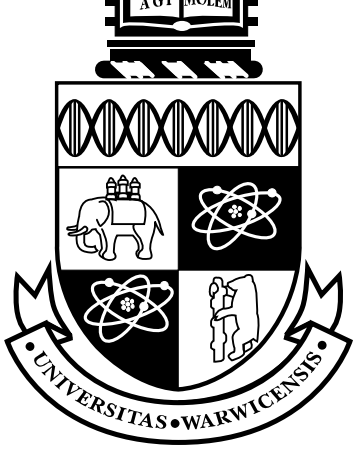

Characterisation of fully nonlinear Berk-Breizman phenomenonology

by

R. G. L. Vann

Thesis

Submitted to the University of Warwick

for the degree of

Doctor of Philosophy

Physics

....

Contents

List of Figures

Acknowledgments

Principally I should like to thank my various supervisors for all their assistance and support over the duration of my PhD, to guide me when I was lost and to encourage me when I was stuck.
Officially I have been supervised by Prof. Richard Dendy and Dr. Nick d'Ambrumenil. Despite not being a plasma specialist, Nick has been steadfast in his support of me throughout the PhD, and in particular the writing of this thesis, chiding me when I seem to be playing too much hockey and encouraging me when I produce something of worth. Richard, on the other hand, is very much the plasma specialist, and has managed (I hope) to instil a bit of the plasma physicist into someone with a very definite mathematical background.
Unofficially I have been "supervised" by several other members of the Warwick theory and astrophysics groups. In particular I should like to thank Prof. George Rowlands and Dr. Tony Arber. In the first place, George played a critical rôle in my getting to Warwick; since then from him I have learnt the fundamentals of nonlinear science and had many fascinating discussions on a range of scientific and non-scientific topics. Tony introduced me to doing numerical work properly and rigorously. Only by working with Tony have I learnt how to be confident that the data coming from numerical simulations is not garbage. Furthermore, I should like to thank Professors Berk and Breizman for hosting me at the University of Texas at Austin during August 2001 and the useful conversations that we have had before, during and after that visit.
I should also like to thank my sponsors. EPSRC and UKAEA/Euratom sponsored me under a joint CASE scheme. The University of Warwick American Studies Exchange Committee provided me with some travel money for the aforementioned trip to Texas.

Declarations

Except where otherwise indicated, this thesis contains an account of my own independent research in the Department of Physics, University of Warwick, between October 1999 and September 2002 under the supervision of Dr. N. d'Ambrumenil. I have also collaborated on a daily basis with Prof. G. Rowlands and Dr. T. D. Arber (also both of the Department of Physics, University of Warwick) and Prof. R. O. Dendy (of UKAEA Fusion, Culham, but also an Honourary Professor at Warwick).
Some of this work has appeared in the scientific literature in the following joint publications:

Publications

1. T. D. Arber and R. G. L. Vann 2002. "A critical comparison of Eulerian grid based Vlasov solvers" *J. Comput. Phys.* **180** (1) 339-357
2. R. G. L. Vann, R. O. Dendy, G. Rowlands, T. D. Arber and N. d'Ambrumenil. "Fully nonlinear phenomenology of the Berk-Breizman augmentation of the Vlasov-Maxwell system" *Phys. Plasmas* **10** (3) 623-630

Presentations

1. Colloquium at the Institute of Fusion Studies, University of Texas at Austin, U.S.A., 8th August 2001.
2. Oral presentation to the *7th IAEA Technical Committee Meeting on Energetic Particles in Magentic Confinement Systems*, Göteborg, Sweden, 8th-11th October 2001.

Abstract

The Berk-Breizman augmentation of the Vlasov-Maxwell system (henceforth the VM(BB) system) is widely used to model nonlinear resonant excitation and damping of wave fields by energetic particles in magnetic fusion plasmas. A code, based on the Piecewise Parabolic Method, is used to integrate the fully nonlinear Berk-Breizman system of equations across the whole parameter space. The present work provides, for the first time, numerical solutions to the fully nonlinear set of model equations. By considering the time evolution of the electric field energy, we show that the system behaviour can be classified into four types, namely damped, steady state, periodic and chaotic. Each type of behaviour occurs in well-defined regions of parameter space. We present a diagram in parameter space that shows how the model's behaviour changes as key parameters are varied. Moreover we demonstrate, by consideration of diagrams in (x, v) phase space, that the underlying process generic to the parameter values is the competition between the (re)formation of the spatially uniform equilibrium distribution and the formation of a phase space hole.

The development of the aforementioned code is a major component of this project. A common problem with direct Vlasov solvers is ensuring that the distribution function remains positive. A related problem is to guarantee that the numerical scheme does not introduce false oscillations in velocity space. We use a variety of schemes to assess the importance of these issues and to determine an optimal strategy for Eulerian split approaches to Vlasov solvers. From these tests we conclude that maintaining positivity is less important than correctly dissipating the fine-scale structure which arises naturally in the solution to many Vlasov problems. Furthermore we show that there are distinct advantages to using high order schemes, i.e. third order rather than second. A natural choice which satisfies all of these requirements is the Piecewise Parabolic Method (PPM) This time splitting scheme is capable of solving many Vlasov-type systems. In this thesis we generate, systematically test, and demonstrate the high performance of an algorithm designed specifically for solving the VM(BB) system.

Chapter 1

Introduction

Containment of the kinetic energy of alpha particles produced in deuterium-tritium reactions is critical to the success of magnetic confinement fusion experiments with burning plasmas. The 3.5 MeV kinetic energy of each fusion-produced alpha particle is required to heat electrons collisionally, which in turn heat deuterium and tritium ions to the temperature required to sustain thermonuclear reactions. Classically the containment of the alpha particles can be achieved if the size of the plasma is large compared to the banana width of trapped alpha particle orbits. However, even if they are initially contained within the plasma, the alpha particles may undergo radial transport as a result of resonant interaction with MHD modes, and in particular modes such as toroidal Alfvén eigenmodes (TAEs) which the alpha particles themselves excite. A major theoretical and experimental effort is aimed at understanding resonant alpha particle interaction with collective magnetohydrodynamic (MHD) modes.

The Berk-Breizman augmentation of the Vlasov-Maxwell system [BB90a,BB90b, BB90c, BBY92, BBY93, BBP96, BBP95] (described in this thesis in Chapter 2) reflects an effort to develop a numerically or algebraically tractable model for the self-consistent interaction between energetic particles and wave fields in fusion plasmas. It can be considered as a generalization of the theory of the electrostatic bump-on-tail instability, and is widely used as a basis for interpreting the interaction of energetic particles with collective modes in tokamak experiments [BBY92, FBB$^+$98, HFS00, W$^+$97].

We cast the VM(BB) system of equations for the particle distribution function, $f(x, v, t)$, which depends on time t, position x and particle velocity v and for the electric field, $E(x, t)$, in the following form

$$\frac{\partial f}{\partial t} + v\frac{\partial f}{\partial x} + E\frac{\partial f}{\partial v} = Q(v) - \nu_a(v)f \tag{1.1}$$

$$\frac{\partial E}{\partial t} + \int v\,(f - f_0)\,dv = -\gamma_d E \tag{1.2}$$

The addition of the terms on the right hand sides of these equations constitutes the BB augmentation of the original Vlasov-Maxwell system. Here $F_0(v)$ denotes the particle source function (usually bump-on-tail), $f_0\,(v)$ the spatially averaged distribution, $\nu_a(v)$ the particle annihilation rate and γ_d the combined effect of all background damping mechanisms that act on the electric field. Quantities are normalised to the inverse plasma frequency, the Debye length and the plasma thermal speed.

Previous theoretical work has been constrained to particular weakly nonlinear limiting parameter regimes, such as the case of weak damping [BBY93] or slow linear growth [BBP96, FBB$^+$98]. Moreover, previous work [BBY93, BBP96] contained a simplifying assumption that the bulk of the plasma is cold. Our study is free from this constraint.

Only with a technique that allows investigation across the whole of parameter space can one move towards a full description of the wealth of physics that arises from the Berk-Breizman model described by Eqs. (1.1) and (1.2). The present work provides, for the first time, numerical solutions to the fully nonlinear set of model equations. Our results are presented in Chapter 3. By considering the time evolution of the electric field energy, we show that the system behaviour can be qualified into four types, namely damped, steady state, periodic and chaotic. Each time series is categorised into one of these four types using the algorithm described in Appendix B. The results of this categorisation are displayed in the bifurcation diagram Figure 3.2, which shows how the model's behaviour changes as the key parameters γ_d and ν_a are varied. (The uniform steady-state solution $F_0(v) = Q(v)/\nu_a(v)$ is fixed throughout this diagram; the robustness of the diagram to a change in $F_0(v)$ is discussed in Sec. 3.5.) We find that each type of behaviour occurs in well-defined regions of (γ_d, ν_a) parameter space. Moreover we demonstrate in Section 3.4.2, by

consideration of diagrams in (x, v) phase space, that the underlying process generic to all parameter values is the competition between the (re)formation of the spatially uniform equilibrium bump-on-tail distribution and the formation of a phase space hole.

An investigation of this sort requires a sophisticated computer code. The development of this code is described in Chapter 4. It constitutes the backbone on which much of the work in this project is built. We begin by designing a solver of the Vlasov-Poisson system (for which there are known results against which one can benchmark) and then proceed to adapt the algorithm to solve the full Berk-Breizman augmentation of the Vlasov-Maxwell system.

Our technique rests on splitting the Vlasov solver into separate spatial and velocity space updates and has the advantage that each of these updates can then be treated as simple advections at constant speed. Since the original, ground-breaking publication [CK76] most attention on fixed grid Vlasov solvers has concentrated on improving the accuracy of the advection sweeps. Recent examples have included use of MacCormack's method [HF01] and conservative schemes [FSB01]. A common problem with all Vlasov solvers is that the solutions to Vlasov's equation often involve a fine-scale filamentation which increases in time. For example the solution to the linear Landau damping problem has a perturbed distribution function which varies as $\exp(ikvt)$. Higher order schemes have a tendency to produce Gibbs overshoot when this occurs unless some additional averaging is applied. A related problem is that there is no guarantee, except for first order schemes, that the numerical solution has not introduced regions of negative distribution function. Both of these problems are identical to the problems encountered in the treatment of shocks in computational fluid mechanics. Ways of avoiding the restrictions imposed on the order of the scheme by Godunov's theorem in fluid dynamics have a direct analogy in the solution of Vlasov problems. In Chapter 4 we concentrate on studying the importance of positivity, order and monotonicity in the advection steps by comparing a variety of codes with different properties. The original time stepping algorithm is then adapted to solve the displacement current equation (DCE) in place of Poisson's equation. It is then further adapted to solve the full model equations. We extensively benchmark the code to show that, not only is it a computationally

efficient code, but also that the results it produces are trustworthy.

Chapter 2

Berk-Breizman theory

Berk-Breizman theory is built upon Vlasov's equation (for the particle distribution f) and Maxwell's equations (for the electric field E). In this Chapter we derive the electrostatic Vlasov equation (2.23), discuss how to obtain the electric field from the relevant Maxwell's equations (2.27) and (2.28), and thence develop the Berk-Breizman model equations (2.33) and (2.39).

2.1 The electrostatic Vlasov-Maxwell equations

2.1.1 Normalisation of variables

Throughout this thesis we are concerned with the motion of many particles, each with charge q_s and mass m_s, moving in one spatial dimension and one velocity dimension, in the presence of an electric field, but in the absence of any magnetic field.

It is convenient to work in dimensionless quantities and so we scale physical variables as follows:

$$x = \frac{1}{\lambda_D} \times \text{displacement} \tag{2.1}$$

$$v = \frac{1}{v_\theta} \times \text{velocity} \tag{2.2}$$

$$t = \omega_p \times \text{time} \tag{2.3}$$

$$E(x,t) = \frac{q_s}{m_s v_\theta \omega_p} \times \text{electric field} \tag{2.4}$$

where the Debye length λ_D, the thermal velocity v_θ, and the plasma frequency ω_p

are defined by

$$\lambda_D^2 = \frac{\epsilon_0 k_B T_s}{n_0 q^2} \tag{2.5}$$

$$v_\theta^2 = \frac{k_B T_s}{m} \tag{2.6}$$

$$\omega_p^2 = \frac{n_0 q_s^2}{m_s \epsilon_0} \tag{2.7}$$

The quantity T_s does not represent the temperature of the particles (which is not well-defined for a strongly non-Maxwellian distribution) but instead is some typical temperature of the system in the context of particle speeds. Similarly, v_θ is merely a normalisations speed related to the typical temperature T_s and in general does not characterise the particle speed distribution. We take the spatial coordinate to be periodic with period length L.

2.1.2 Aside: representation of derivatives

Throughout this thesis we occasionally use what might be considered an unorthodox notation for full and partial derivatives. We sometimes write full derivatives

$$\frac{dQ}{dx} \equiv d_x Q \tag{2.8}$$

and similarly for partial derivatives

$$\frac{\partial P}{\partial v} \equiv \partial_v P \tag{2.9}$$

This notation is more concise and no less precise than conventional notation.

2.1.3 Derivation of the electrostatic Vlasov equation

The dynamics of N particles moving in one spatial dimension under the influence of an electric field, where the i-th particle has position x_i and velocity v_i (in the dimensionless units defined above), are governed by

$$\dot{x_i} = v_i \tag{2.10}$$

$$\dot{v_i} = E_i \tag{2.11}$$

where the electric field experienced by the i-th particle

$$E_i = \sum_{j=1, j\neq i}^{N} \Psi(x_j - x_i) \tag{2.12}$$

for some function $\Psi(x)$ which satisfies Newton's third law $\Psi(x) = -\Psi(-x)$. In a typical physical system, $N \sim 10^{23}$, which makes it impossible in practice to solve directly Eqs. (2.10) and (2.11). We therefore seek to make an approximation of these equations which is tractable but also retains the important physics.

Eqs. (2.10) and (2.11) correspond to the Hamiltonian

$$H = \sum_{i=1}^{N} \left[\frac{v_i^2}{2} + \sum_{j=1, j\neq i}^{N} \Phi(x_j - x_i) \right] \tag{2.13}$$

where the function Φ satisfies

$$\frac{d\Phi}{dx} = \Psi \tag{2.14}$$

Since the dynamics of the particles is Hamiltonian, we can apply Liouville's theorem. This tells us that the density of systems in the $2N$-dimensional phase space satisfies

$$\frac{\partial P}{\partial t} + \dot{\xi} \cdot \nabla_\xi P = 0 \tag{2.15}$$

where $\xi = (x_1, x_2, \ldots, x_N, v_1, v_2, \ldots, v_N)$

$$\Leftrightarrow \frac{\partial P}{\partial t} + \boldsymbol{v} \cdot \nabla_{\boldsymbol{x}} P + \boldsymbol{E} \cdot \nabla_{\boldsymbol{v}} P = 0 \tag{2.16}$$

Now consider the dynamics of the first particle. We denote by $f_j(x, v)$ the probability of finding the j-th particle with position x and velocity v. Then

$$f_1(x_1, v_1) = \int dx_2 \int dv_2 \int dx_3 \int dv_3 \ldots \int dx_N \int dv_N \; P(\xi) \tag{2.17}$$

which gives

$$\frac{\partial f_1}{\partial t} + v_1 \frac{\partial f_1}{\partial x_1} + \sum_{j=2}^{N} \int \Psi(x_j - x_1) \; \frac{\partial P_{1j}}{\partial v} \; dx_j = 0 \tag{2.18}$$

where

$$P_{1j} \equiv P_{1j}(x_1, x_j, v_1) = \int dv_j \left(\prod_{m=2, m\neq j}^{N} \int dx_m \int dv_m \right) \; P(\xi) \tag{2.19}$$

is the probability of finding both the first particle at position x_1 with velocity v_1 and the j-th particle at position x_j.

We now make the assumption that there is no correlation between the orbits of the particles i.e. that there is no correlation between (x_i, v_i) and (x_j, v_j), $i \neq j$. Then

$$P_{1j} = f_1(x_1, v_1) \; n_j(x_j) \tag{2.20}$$

where

$$n_j(x) = \int f_j(x,v)\ dv \tag{2.21}$$

is the probability of finding the j-th particle at position x. The expectation value of the electric field acting upon the first particle

$$\langle E_1(x_1)\rangle = \sum_{j=2}^{N} \int \Psi(x_j - x_1)\ n_j(x_j)\ dx_j \tag{2.22}$$

Dropping the subscript 1's and the angled brackets gives us the Vlasov equation for $f(x,v,t)$ and $E(x,t)$:

$$\frac{\partial f}{\partial t} + v\frac{\partial f}{\partial x} + E\ \frac{\partial f}{\partial v} = 0 \tag{2.23}$$

Note that, considering f as a probability, we have implicitly normalised

$$f(x,v,t) = \frac{1}{n_0} \times \text{particle number distribution} \tag{2.24}$$

where n_0 is the mean number density.

It is the custom in the literature that the particles associated with a single-species problem are positively charged. We follow that custom in this thesis and so problems modelling the flow of either only alpha particles or only electrons assume the relevant species to have positive charge.

In general we are concerned with the dynamics of more than one particle species. Wherever this is the case we carry the true physical signs of the charges. So for example the electronic charge is taken to be negative in a multi-species problem. For each particle species we have a distribution f_s, with mass m_s and charge q_s; the electric field felt by the particles is independent of their species. Suppose we model the dynamics of two species, ions and electrons, labelled by subscripts i and e respectively, and that the two species have opposite charges of equal magnitude (then the q_s and m_s in the normalisation of the electric field Eq. (2.4) refer to the charge on the ion and the mass of the electron, respectively). The ion-electron mass ratio is denoted by M_r; in practice $M_r \sim 1000$. Then we have two Vlasov equations given by

$$\frac{\partial f_i}{\partial t} + v\frac{\partial f_i}{\partial x} + \frac{1}{M_r}E\ \frac{\partial f_i}{\partial v} = 0 \tag{2.25}$$

$$\frac{\partial f_e}{\partial t} + v\frac{\partial f_e}{\partial x} - E\ \frac{\partial f_e}{\partial v} = 0 \tag{2.26}$$

2.1.4 Equations for the electric field

Maxwell's equations tell us about the electric field. Poisson's equation gives

$$\nabla \cdot \boldsymbol{E} = \rho, \tag{2.27}$$

while the displacement current equation (DCE) gives

$$\nabla \times \boldsymbol{B} = \boldsymbol{J} + \frac{\partial \boldsymbol{E}}{\partial t} \tag{2.28}$$

where the magnetic field $\boldsymbol{B}$ and current $\boldsymbol{J}$ are normalised appropriately.

We consider only the electrostatic case, and take $\boldsymbol{B} = 0$ for simplicity. We work in one dimension, so vectors become scalars. Now let us cast these two equations of Maxwell in terms of particle distributions. If we are considering the dynamics of two species, then the particle distributions of the ions and electrons, denoted by f_i and f_e respectively, are governed by Eqs. (2.25) and (2.26). Poisson's equation (2.27) becomes

$$\frac{\partial E}{\partial x} = \int_{-\infty}^{+\infty} (f_i - f_e)\, dv \tag{2.29}$$

However if instead we consider the motion of electrons only, then we assume that there is a background ion population which

- is spatially uniform with a number density that ensures global neutrality, and
- has a constant and uniform drift velocity that ensures that there is zero total current.

It now becomes convenient to follow the custom in the literature and take the electronic charge to be positive. Then the evolution of the electron distribution (denoted simply by f) is governed by Eq. (2.23). Poisson's equation (2.27) becomes

$$\frac{\partial E}{\partial x} = \int_{-\infty}^{+\infty} f\, dv - 1 \tag{2.30}$$

where f_0 denotes the spatially averaged (electron) distribution function.

Now let us consider how to cast the DCE in terms of particle distributions. We consider only the electrostatic case and again take the magnetic field $B = 0$. The current is the total number of particles passing a point in unit time and so is given by the first velocity moment of the distribution. For two species this corresponds to

$$\frac{\partial E}{\partial t} = \int_{-\infty}^{+\infty} v\,(f_e - f_i)\, dv \tag{2.31}$$

For electrons only with an ion background, we again take the electronic charge to be positive and obtain

$$\frac{\partial E}{\partial t} = \int_{-\infty}^{+\infty} v\,(f_0 - f)\,dv \tag{2.32}$$

We remark that the DCE requires an initial condition of the form $E(x, t = 0) = E_0(x)$; the appropriate E_0 may be obtained from Poisson's equation.

2.2 The VM(BB) model equations

Recall that the objective of Berk-Breizman theory is to provide a heuristic description of the nonlinear interaction between particles and wave modes in plasmas. This is achieved by augmenting Vlasov's equation (2.23) to include terms describing particle injection and relaxation, and the DCE to include a term for background wave damping. Together these equations, the Berk-Breizman augmentation of the Vlasov-Maxwell equations, will be referred to as the VM(BB) model equations.

2.2.1 The modified Vlasov equation: particle source and loss

We wish to model the interaction between energetic particles (particularly alpha particles) and collective wave modes. This requires the addition of a particle source term to the Vlasov equation (2.23). We wish to simulate the injection of particles with high energies and so the source must have a strong velocity dependence. However, we do not wish there to be an unbounded number of particles in the system and so we also introduce a particle loss term. This loss term is taken to be a linear relaxation operator. It corresponds to the addition of a friction in the system.

The Berk-Breizman modification to the Vlasov equation occurs historically early in the literature. To quote from Sec. III of Ref. [BB90a]:
The simplest problem we can pose is to consider an electrostatic plasma wave (or acoustic wave) in one dimension. In addition to the background plasma, we inject a hot species with an injection velocity distribution $Q(v)$. These particles are assumed to annihilate (through some physical mechanism such as charge exchange) at a rate ν_a. The kinetic equation for the distribution function f is

$$\frac{\partial f}{\partial t} + v\frac{\partial f}{\partial x} + E\frac{\partial f}{\partial v} = -\nu_a(v)f + Q(v) \tag{2.33}$$

There exists a uniform equilibrium solution

$$f(x, v, t) = F_0(v) \equiv \frac{Q(v)}{\nu_a(v)} \tag{2.34}$$

Henceforth, unless otherwise specified, we treat ν_a as a constant independent of v. As described below by Eq. (2.45), the initial distribution that we use is always a spatial modulation of the uniform equilibrium solution. The quantity $F_0(v)$ therefore denotes both the equilibrium solution and the spatial mean of the initial distribution.

The mean particle number density, given by

$$n_0 = \frac{1}{L} \int_0^L dx \int_{-\infty}^{+\infty} f \, dv \, dx \tag{2.35}$$

relaxes at a rate ν_a to the number of particles in the equilibrium distribution $F_0(v)$, given by

$$N_0 = \int_0^L dx \int_{-\infty}^{+\infty} F_0 \, dv \tag{2.36}$$

If there exists a time for which $n_0 = N_0$, then the mean number density is conserved.

2.2.2 The external wave damping equation

In the original papers [BB90a, BB90b, BB90c], the power transfer between the electrostatic wave mode and the distribution (consisting both of particles trapped in the potential of the wave mode and passing particles) is considered without any external wave damping. Later, *the dissipation rate γ_d of the excited wave caused by the background plasma* is introduced [BBY92]. Moreover, when the distribution has flattened in the region of the wave mode's phase velocity so that there is no linear drive, the wave mode energy changes as [BBY92]

$$\frac{d\mathcal{E}_{\text{wave}}}{dt} = -\gamma_d \, \mathcal{E}_{\text{wave}} \tag{2.37}$$

In [BBY93] an additional term is added to Eq. (2.37):

$$\frac{d\mathcal{E}_{\text{wave}}}{dt} = 2\gamma \, \mathcal{E}_{\text{wave}} - \gamma_d \, \mathcal{E}_{\text{wave}} \tag{2.38}$$

Here the term involving γ *describes the wave excitation by energetic particles, while the second term takes into account background damping.* So the γ introduced here is not a fixed parameter of the model. It is the nonlinear growth rate of the mode dependent in a nontrivial fashion on the distribution function. When the electric

field energy $\mathcal{E}$ is small, this γ corresponds to the growth rate as calculated from the linearised dispersion relation Eq. (2.53) below.

The terms in γ_d on the right hand side of equations (2.37) and (2.38) differ by a factor of two from the corresponding equations in [BBY92] and [BBY93]. This change makes them consistent with the work in [VDR+03] and the remainder of this thesis. This thesis therefore is internally consistent, but differs in its definition of γ_d compared to much of the existing literature. For example, contrast my equation (2.56) with the corresponding equation $\gamma \equiv \gamma_L - \gamma_d$ in [BBP96].

The introduction of field damping means that we are not able to use a modification of Poisson's equation: Poisson's equation gives the electric field as a function of the current phase space distribution. Instead we augment the DCE with an Ohmic dissipative term as follows:

$$\frac{\partial E}{\partial t} = -\int v\,(f - f_0)\,dv - \gamma_d E \tag{2.39}$$

where f_0 is the spatially averaged distribution function. The nonlinear growth rate of Eq. (2.38) is now described by the first term on the right hand side of Eq. (2.39). The dissipative term is the simplest Ansatz (equivalent to Ohm's law) to account for the interaction with modes and excitations not treated explicitly in the 1D Vlasov-Maxwell equations, whose effect is to absorb energy out of the 1D plasma. In the case $\gamma_d = 0$, of course, Eq. (2.39) reduces to the DCE.

2.2.3 Boundedness of the total energy

We show here that the total system energy has an upper bound. The spatially averaged total energy density in the system $H = T + A$, where the kinetic contribution is given by

$$T(t) = \frac{1}{L}\int_0^L \int_{-\infty}^{+\infty} v^2 f(x,v,t)\; dv\; dx \tag{2.40}$$

and the mean electric field energy density is given by

$$A(t) = \frac{1}{L}\int_0^L E(x,t)^2 dx \tag{2.41}$$

The rate of change of the spatially averaged total energy density can be found

from Eqs. (2.33) and (2.39):

$$\begin{aligned} d_t H &= K - \nu_a T - 2\gamma_d A && (2.42) \\ &\leq K - \min(\nu_a, 2\gamma_d)\, H && (2.43) \end{aligned}$$

where $K \geq 0$ is a constant determined by the injection distribution. Therefore

$$H > H_{\max} \equiv \frac{K}{\min(\nu_a, 2\gamma_d)} \implies d_t H < 0 \qquad (2.44)$$

So, for $\nu_a > 0$ and $\gamma_d > 0$, an upper bound on the total energy exists.

Berk, Breizman and Pekker [BBP96] have shown that under particular simplifying assumptions the VM(BB) model permits explosive solutions. The mathematical singularity in these solutions is by itself an indication that the solution eventually fails to meet its applicability conditions, as formulated in [BBP96]. The energy bound calculated above gives a quanititative upper bound for the time over which the explosive solution is meaningful.

2.3 The electrostatic bump-on-tail VM(BB) problem

We recall that the main objective of the Berk-Breizman theory is to model the interaction between energetic particle beams and collective modes. In particular, the theory is targeted towards a self consistent understanding of the interaction between energetic fusion alpha particles and Alfvén eigenmodes. This is made tractable by applying the mathematical system outlined in Sec. 2.2 to consider the paradigmatic electrostatic bump-on-tail problem; it has been argued [BBY92] that this approach contains the essential physics .

2.3.1 Initial distribution

In the fully nonlinear self consistent calculations described below, we always specify an initial distribution that is a spatial modulation of the equilibrium distribution F_0 defined by Eq. (2.34):

$$f(x, v, t = 0) = (1 + \alpha \cos kx)\, F_0(v) \qquad (2.45)$$

where $k = 2\pi/L$ and $\alpha \ll 1$ is the amplitude of the small perturbation

The initial electric field is calculated from Poisson's equation (2.30):

$$\partial_x E = \int_{-\infty}^{+\infty} f(v)\ dv - 1 \tag{2.46}$$

which implies

$$E(x, t=0) = \alpha \cos kx \int_{-\infty}^{+\infty} F_0(v)\ dv \tag{2.47}$$

despite the system not necessarily satisfying Poisson's equation for $t > 0$.

Motivated by a study of beam-plasma interactions, we choose the equilibrium distribution $F_0(v)$ to be the bump-on-tail distribution

$$F_0(v) = F_{\text{bulk}} + F_{\text{beam}} \tag{2.48}$$

where

$$F_{\text{bulk}} = \frac{\eta}{v_c\sqrt{2\pi}}\ \text{Exp}\left(-\frac{1}{2}\left(\frac{v}{v_c}\right)^2\right) \tag{2.49}$$

$$F_{\text{beam}} = \frac{1-\eta}{v_t\sqrt{2\pi}}\ \text{Exp}\left(-\frac{1}{2}\left(\frac{v-v_b}{v_t}\right)^2\right) \tag{2.50}$$

An example bump-on-tail distribution of this form is shown in Fig. 2.1. We note that the quantities v_c and v_t are the thermal velocities characterising the two Maxwellians; a thermal velocity v_T corresponds to a temperature $m_s v_T^2/2k_B$.

Previous work has been constrained to work with a particular limiting case of bump-on-tail distribution; namely one with a cold bulk ($v_c \to 0$) and warm beam ($v_t \to \infty$). Our direct numerical treatment permits us to specify particular finite values for the temperatures of the beam and bulk. The fully nonlinear solution then includes by construction the beam-bulk interaction, which previously has had to be omitted.

One may then rewrite Eq. (2.33) as

$$\frac{\partial f}{\partial t} + v\frac{\partial f}{\partial x} + E\frac{\partial f}{\partial v} = \nu_a F_{\text{beam}} - \nu_a (f - F_{\text{bulk}}) \tag{2.51}$$

where the first term on the right hand side is the injected beam and the second term is mathematically similar to a Krook collision operator (Cf. Ref. [BGK] Eq. (3)).

2.3.2 Linear stability

Whilst our objective is to study the fully nonlinear system, we first address the linear stability of the initial distribution. We consider a small perturbation from

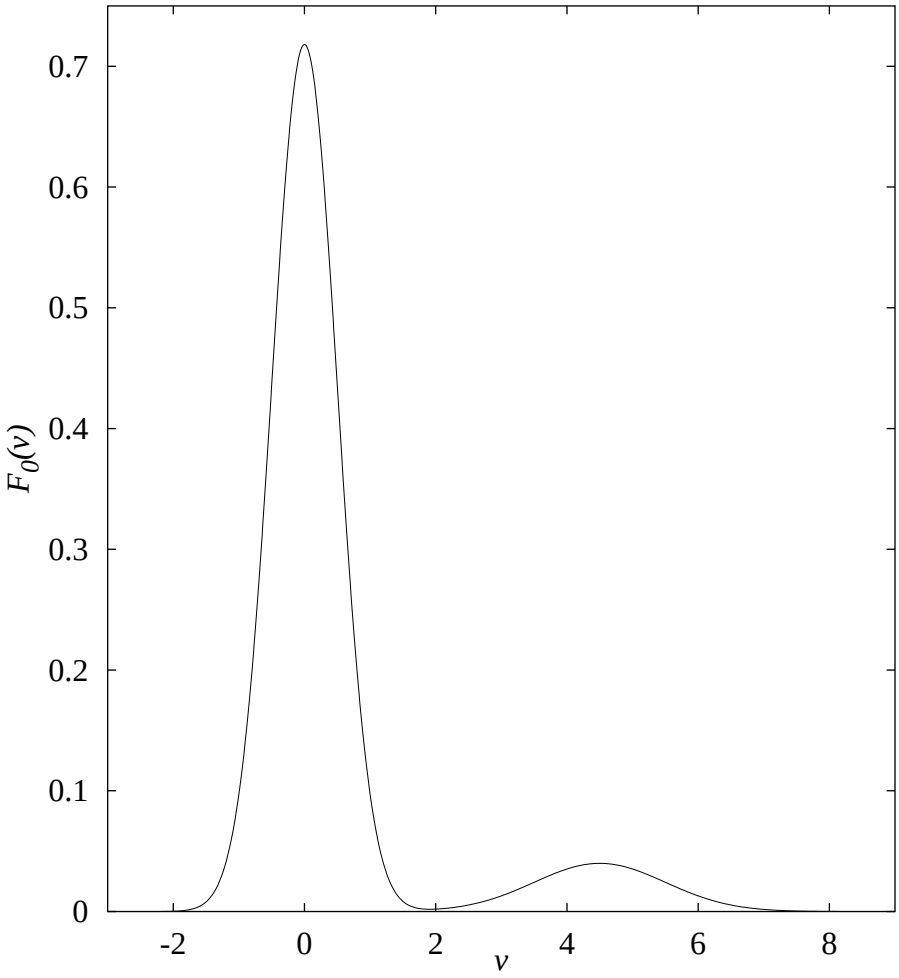

Figure 2.1: Bump-on-tail velocity distribution of the form given in Eq. (2.48), with the parameters that are used in the main simulations described below: $\eta = 90\%$, $v_c = 1.0$, $v_t = 0.5$, and $v_b = 4.5$.

this uniform steady state solution $F_0(v)$ as prescribed by Eq. (2.45), and make the ansatz that the perturbed quantities are of the form

$$f_1, E_1 \sim \mathrm{Exp}\left[i\left(kx - \omega' t\right) + \gamma' t\right] + \text{c.c.} \tag{2.52}$$

where the wavenumber k, frequency ω', and growth rate γ' are all purely real. Linearizing Eqs. (2.33) and (2.39), we derive the Landau-type dispersion relation

$$\gamma' + \gamma_d - iw = \int_\Gamma \frac{v\, d_v F_0}{(\gamma' + \nu_a) + i\,(kv - \omega')}\, dv \tag{2.53}$$

where Γ is the appropriate Landau contour: for $\gamma' + \nu_a > 0$, the contour is the real axis; for $\gamma' + \nu_a \leq 0$, the contour stretches in a keyhole from the real axis around the pole. (Refer to the treatment of Landau damping by Clemmow and Dougherty [CD69] Sec. 8.2.)

The implicit dispersion relation (2.53) may have more than one solution for (γ', ω'). We define the *linear growth rate* γ (which is a function of γ_d and ν_a, and depends on the distribution $F_0(v)$) as the most positive γ' (or equivalently the least negative, if the system is damped) for which the linearized dispersion relation Eq. (2.53) can be satisfied; the frequency ω' corresponding to the growth rate $\gamma' = \gamma$ is denoted by ω. An algorithm for calculating γ and ω is presented in Appendix C.1. A spatially uniform distribution $F_0(v)$ is considered to be *linearly stable* with respect to small perturbations of the form given in Eq. (2.52) if the linear growth rate γ is less than zero. If the distribution F_0 is linearly stable, then as t increases, $E \to 0$ and $f \to F_0$. If F_0 is linearly unstable, then the electric field and spatial perturbation initially grow exponentially, at a rate approximately given by γ. For a particular initial distribution $F_0(v)$, we define γ_L to be the linear growth rate of the system in the absence of background damping or particle injection, that is, for the case $\nu_a = \gamma_d = 0$.

Berk, Breizman and co-workers [BBY93, BBP96] have taken the bulk plasma to be cold ($v_c \to 0$ in Eq. (2.49)) and the beam to be warm ($v_t \gg 1$ in Eq. (2.50)). In addition, in Refs. [BBY93, BBP96], $\nu_a, \gamma \ll \omega$, and ν_a is a function of velocity that acts only on the beam ($\nu_a(v) = 0$ for $|v| \ll 1$). In this case the linearized dispersion relation reduces from the complicated implicit equation (2.53) to a simple explicit algebraic equation, which yields the linearized dispersion relation equations

(cf. Ref. [BBY93] Eq. (22)):

$$\omega^2 = \eta \tag{2.54}$$

$$2\gamma_L = \pi\omega k^{-2} \left(d_v F_0\right)_{\omega/k} \tag{2.55}$$

$$2\left(\gamma_L - \gamma\right) = \gamma_d \tag{2.56}$$

Note that in this approximation ω is independent of γ_d and ν_a. As a result, the resonant phase velocity $v_{\rm res} = \omega/k$ and the linear growth rate γ_L depend only on the choice of distribution function $F_0(v)$. Note also that in this approximation γ depends linearly on γ_d and is independent of ν_a. So the linear stability threshold for a particular $F_0(v)$ is the line $\gamma_d = 2\gamma_L$ in (γ_d, ν_a) parameter phase space.

2.3.3 Stability threshold analysis

Given the initial distribution $F_0(v)$, we wish to know the linear stability threshold, i.e. the curve $\gamma = 0$ in (γ_d, ν_a) parameter space. Moreover, as we are usually concerned with the regime $\nu_a \ll 1$, we will look for a linear approximation for the parameter interdependence of the form

$$\omega(\nu_a) = \omega_0 + \nu_a\,\omega_0' + \mathcal{O}(\nu_a^2) \tag{2.57}$$

$$\gamma_d(\nu_a) = \gamma_{d0} + \nu_a\,\gamma_{d0}' + \mathcal{O}(\nu_a^2) \tag{2.58}$$

Given we are considering the case $\gamma = 0$, then for $\nu_a > 0$ Eq. (2.53) reduces to

$$\mathcal{I} \equiv \int_{-\infty}^{+\infty} \frac{g(u)}{u - i\epsilon}\,du = k(\omega + i\gamma_d) \tag{2.59}$$

where

$$g(u) = \left(u + \frac{\omega}{k}\right)\ F_0'\left(u + \frac{\omega}{k}\right) \tag{2.60}$$

$$\epsilon = \frac{\nu_a}{k} \tag{2.61}$$

We perform this integral by use of the contour C_R in the complex plane shown in Fig. 2.2. We note that, since the integrand is analytic within C_R, we have by Cauchy's theorem

$$\oint_{C_R} \frac{g(u)}{u - i\epsilon}\,du = 0 \tag{2.62}$$

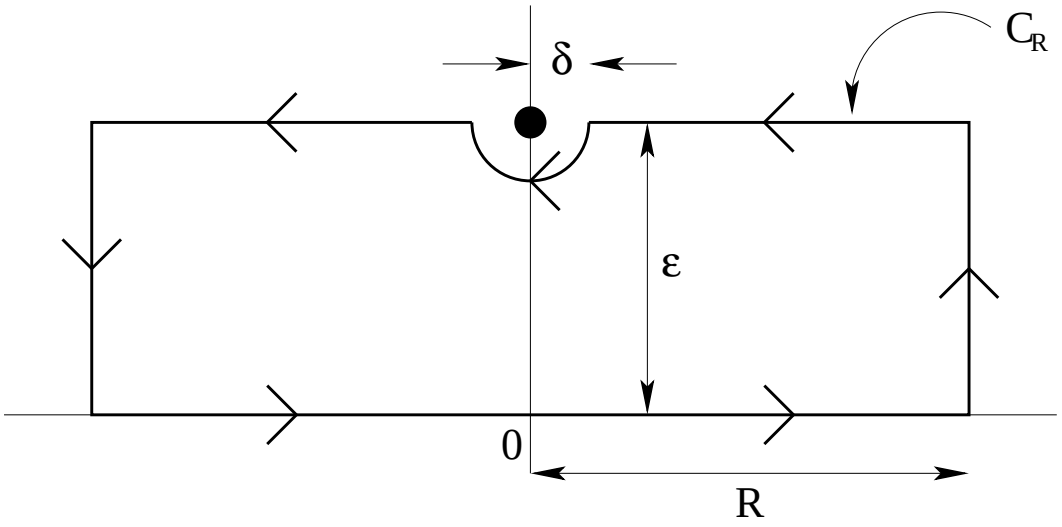

Figure 2.2: Contour for the evaluation of γ'_{d0}

As $R \to \infty$, $g(u) \to 0$, and so the contribution over the ends disappears; we also let $\delta \to 0$ and obtain

$$\begin{aligned}
\mathcal{I} &= \mathcal{P}\int_{-\infty}^{+\infty} \frac{g(u+i\epsilon)}{u}\,du + i\pi g(i\epsilon) && (2.63)\\
&= \mathcal{P}\int_{-\infty}^{+\infty} \frac{g(u)}{u}\,du + i\pi g(0) - \epsilon\pi g'(0) + i\epsilon\mathcal{P}\int_{-\infty}^{+\infty} \frac{g'(u)}{u}\,du + \mathcal{O}(\epsilon^2) && (2.64)\\
&= k(\omega + i\gamma_d) && (2.65)
\end{aligned}$$

for $\epsilon \ll 1$. Taking zeroth order terms we find

$$\begin{aligned}
\omega_0 &= \mathcal{P}\int_{-\infty}^{+\infty} \frac{v d_v F_0}{k\,v - \omega_0} dv && (2.66)\\
\gamma_{d0} &= \frac{\pi\omega_0}{k^2}\, d_v F_0\left(\frac{\omega_0}{k}\right) && (2.67)
\end{aligned}$$

We assume that we can solve the implicit Eq. (2.66).

Differentiating with respect to ν_a, we obtain expressions for ω'_0 and γ_{d0} (using some of the identities given in Appendix A):

$$\begin{aligned}
w'_0 &= K\left(\frac{1}{k}\mathcal{P}\int_{-\infty}^{+\infty}\left(F'_0(v) + \frac{w_0}{k}F''_0(v)\right)\frac{dv}{k\,v-\omega_0} - 1\right)^{-1} && (2.68)\\
\gamma'_{d0} &= \omega'_0\,K + \frac{1}{k}\mathcal{P}\int_{-\infty}^{+\infty}\left(F'_0(v) + v\,F''_0(v)\right)\frac{dv}{k\,v-\omega_0} && (2.69)
\end{aligned}$$

where

$$K = \frac{\pi}{k^2}\left(F'_0\left(\frac{\omega_0}{k}\right) + \frac{\omega_0}{k}F''_0\left(\frac{\omega_0}{k}\right)\right) \qquad (2.70)$$

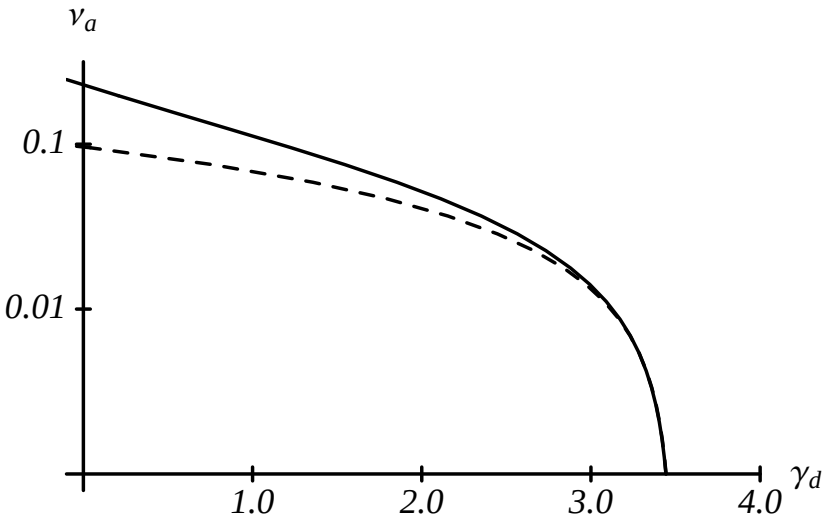

Figure 2.3: The linear stability threshold curve $\gamma = 0$, with the bump-on-tail parameters that are used in the main simulations below: $\eta = 90\%$, $v_c = 1.0$, $v_t = 0.5$, and $v_b = 4.5$. The exact numerical solution is shown by the solid line; the linear approximation given by Eq. (2.67) is shown by the dashed line. We note that there is good agreement.

To evaluate $\gamma_d(\nu_a)$ we observe that it is necessary to compute both w_0' and γ_{d0}'; evaulation of $\omega(\nu_a)$ does not require any knowledge of γ_d. A comparison between this approximation and the exact solution is shown in Fig. (2.3). The agreement is good. We note that the level of agreement may be better or worse than shown here depending on the choice of distribution $F_0(v)$.

Long wavelength expansion

For small k we can expand Eq. (2.66) and integrate by parts (cf. [CD69] §8.3.2) to obtain:

$$\begin{aligned}
\omega_0^2 &= -\int_{-\infty}^{+\infty} v \frac{dF_0}{dv} \left[1 - \frac{k\,v}{\omega_0}\right]^{-1} dv && (2.71)\\
&= -\int_{-\infty}^{+\infty} v \frac{dF_0}{dv} \left[1 + \frac{k\,v}{\omega_0} + \left(\frac{k\,v}{\omega_0}\right)^2 + \ldots\right] dv && (2.72)\\
&= \int_{-\infty}^{+\infty} F_0 \left[1 + 2\frac{k\,v}{\omega_0} + 3\left(\frac{k\,v}{\omega_0}\right)^2 + \ldots\right] dv && (2.73)\\
&= n_0 + \frac{2k\,j_0}{\omega_0} + \frac{3k^2\,T_0}{\omega_0^2} + \mathcal{O}(k^4) && (2.74)
\end{aligned}$$

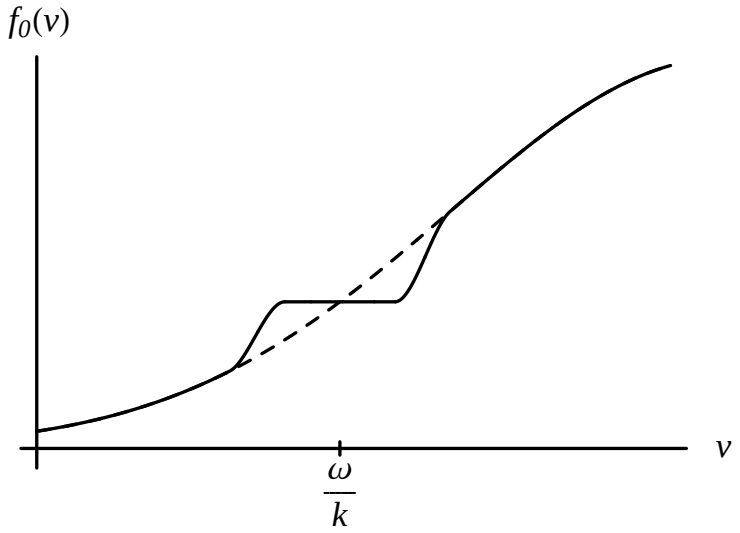

Figure 2.4: Plot of a portion of the spatially averaged distribution function $f_0(v)$. The dashed line represents the initial distribution $F_0(v)$; the solid line shows how the distribution flattens at the mode's phase velocity as a result of particle trapping.

where n_0, j_0, and T_0 are the zeroth, first, and second moments of F_0 respectively. (If $j_0 = 0$ then we have the Langmuir dispersion relation; refer to Clemmow and Dougherty [CD69] Eq. (8.22).) Unfortunately the expansion is only valid if $|kv| < \omega_0$, which is not true for the bump-on-tail distributions which we consider.

2.3.4 Qualitative description of time evolution

Recall our initial conditions given by Eqs. (2.45) and (2.47). If the distribution F_0 is linearly stable, then as t increases, $E \to 0$ and $f \to F_0$. If F_0 is linearly unstable, then the electric field and spatial perturbation initially grow exponentially, at a rate defined approximately by the linear growth rate γ obtained from the linearized dispersion relation (2.53). This linear phase continues until the spatially averaged distribution function $f_0(v)$ begins to flatten in the velocity region $v \approx \omega/k$, as shown in Fig. 2.4. This flattening decreases the growth rate of both the electric field and the spatial perturbation. As the effect of the beam drive decreases, the external damping (at a rate γ_d) becomes significant. Meanwhile, however, the distribution is being reconstituted at a rate ν_a. These two processes compete. We showed in Section 2.2.3 that, for positive γ_d and ν_a, the total system energy is bounded.

Therefore the wave energy must either oscillate (perhaps nonperiodically) or reach a steady state. Berk, Breizman and Ye [BBY93] make an energy balance argument that, in the case of weak damping (γ_d, ν_a small), the system undergoes relaxation oscillations for $\nu_a < \gamma_d$ and saturates to a steady state for $\nu_a > \gamma_d$. Near marginal stability $\gamma \to 0$, Berk, Breizman and Pekker [BBP96] have developed a perturbative description which allows the oscillation/saturation threshold to be calculated as $\nu = \nu_{\rm cr} \equiv 4.38\gamma$.

While the weak damping and marginal stability results provide a valuable guide to some aspects of the system's behaviour, no quantitative description has previously been obtained to describe the system's fully nonlinear behaviour over large regions of (γ_d, ν_a) space. In the present work, we provide a quantitative treatment that can be applied for any choice of $F_0(v)$ and across the whole of parameter space. For various choices of initial distribution, we find that there certainly do exist regions of steady state and oscillatory behaviour as previously predicted. However, we also find that there exist distinct regions of periodic and nonperiodic behaviour, and are even able to demonstrate, via the computation of the most positive Lyapunov exponent, that the aperiodicity is chaotic. We are able to draw quantitatively accurate boundaries between these various regions, and, within each region, measure system statistics such as damping rate or time period. These results are described in detail in the next Chapter.

Chapter 3

Solution of the VM(BB) model

We recall that our objective is to develop a fully nonlinear self consistent model for the interaction between energetic particle populations and collective wave modes using the one-dimensional bump-on-tail problem as a paradigmatic model that captures the essential physics. We begin by choosing an appropriate initial distribution and proceed to describe how the time evolution of the system depends, both qualitatively and quantitatively, on the choice of the electric field damping γ_d and the distribution relaxation rate ν_a. In Section 3.3 we present a bifurcation diagram in (γ_d, ν_a) space for the VM(BB) system. (Recall that a bifurcation is a point in parameter space at which the qualitative nature of solutions changes; refer to [Gle94] for an introduction to the theory of bifurcations.) This diagram is the climax of our work, demonstrating that we are now capable, given an initial distribution F_0, of classifying the model's behaviour throughout the entirety of (γ_d, ν_a) parameter space. We conclude this Chapter by asking how robust these results are to changes in the choice of the initial distribution.

We recall that the VM(BB) model is described by the two partial differential equations (2.33) and (2.39) for the particle distribution f and electric field E:

$$\frac{\partial f}{\partial t} + v\frac{\partial f}{\partial x} + E\frac{\partial f}{\partial v} = -\nu_a(v)f + Q(v) \tag{3.1}$$

$$\frac{\partial E}{\partial t} = -\int v\,(f - f_0)\,dv - \gamma_d E \tag{3.2}$$

Our numerical methods for solving the model are based on a Vlasov-DCE solver we have developed. The algorithms are applicable to advection-type problems in

general and should not be seen as specific to the VM(BB) model. We therefore give a self-contained account of the method in Chapter 4 rather than incorporate it into our discussion of the VM(BB) model.

3.1 Choice of problem

As is usually the case when numerically modelling physical systems, we have to achieve a balance between the level of realism represented by our choice of physical parameters and computational feasibility. In part, we maximise what is computationally possible by developing methods that are both computationally cheap and numerically accurate.

However, we can also maximise the usefulness of available computing resources by understanding the relationship between our choice of physical parameters and the computational cost of modelling the resulting system. Few particles in the beam (hence large η) and a large beam temperature (large v_t/v_b) imply a small linear bump-on-tail drive $\gamma_L \propto (\partial_v F_0)_{\omega/k}$. As a result, the width of the region in velocity space over which the distribution function is flattened is small, as is the amplitude of any wave mode. It is numerically problematic that the qualitative nature of the system's behaviour depends on $(\partial_v f)_{v=\omega/k}$: since any numerical scheme is dissipative, it causes regions of the distribution that are flattened on account of particle trapping to possess a gradient which is nearer than it should be to the gradient of the surrounding distribution. In particular, in the bump-on-tail problem this effect can cause a steady state system to acquire an artificial linear drive. A cold bulk (with small v_c) has a similar numerical problem - specifically that numerical diffusion causes artificial heating of the bulk.

The initial distribution parameters in Eqs. (2.45), (2.49) and (2.50) are chosen as $\eta = 90\%$, $v_c = 1.0$, $v_t = 0.5$, $v_b = 4.5$, $\alpha = 1\%$. This velocity distribution is plotted in Fig. 2.1. This initial distribution is chosen because there are no large gradients in velocity space, and the bulk and beam are well defined. In Section 3.5, we consider the effect of changing the initial distribution. We show in Sec. 4.8.3 that, for this choice of initial distribution, the system is restricted to $|v| < v_{\max} = 8$ (indicated by particle conservation to within one part in 10^{12}) and that $N_x = 128$

points in x, with corresponding grid spacing $\Delta x = L/128$, and $N_v = 1025$ points in v, with grid spacing $\Delta v = 2v_{\max}/N_v$, are sufficient to capture the system's structure. We have also chosen the timestep at each time to be the largest such that $\Delta t \leq 0.1$ and the Courant number $\lambda \leq \lambda_{\max} = 3$.

It is worth asking how one would fit the distribution parameters to experiment, but this cannot be done until the model has been solved. (We discuss in Chapter 5 how this work could be extended to enable connections to be made between Berk-Breizman type models and experimental data.)

3.2 Categorisation of types of behaviour

3.2.1 Definition of categories

We aim to identify and then study a quantity that reflects the state of the system described by Eqs. (3.1) and (3.2), compute its evolution with time, and characterize the resultant time series. We wish to study a quantity that is one dimensional, yet tells us as much as possible about the state of the entire system. So, for example, one might choose to consider the maximum phase space density as a function of time. This quantity is clearly scalar, but does not tell us much about the rest of the system. At the other extreme, we might consider the entirety of (x, v) phase space. This clearly contains a large amount of information about the state of the system, but is extremely difficult to categorise. We believe that achieving a sensible balance between these two extremes is provided by the spatially averaged electric field energy density

$$A(t) = \frac{1}{L}\int_0^L E(x,t)^2 dx \tag{3.3}$$

As we shall see, one can categorise the behaviour of A with time t as being in one of four categories in the limit $t \to \infty$:

1. Damped: $A(t) \to 0$.
2. Steady state: $A(t) \to A_\infty > 0$.
3. Periodic: there exists $T > 0$ such that $A(\tau + T) \to A(\tau)$ for all $\tau \in [t, t + T]$.
4. Chaotic: A is bounded, but does not fall into one of the previous categories.

Appendix B describes the algorithm by which we categorise the computed time series into one of these four types.

We showed in Sec. 2.2.3 that, for $\nu_a, \gamma_d \neq 0$, the total system energy is bounded. This implies that $A(t)$ is also bounded and therefore the list of categories for $A(t)$ is complete. However, we need to justify labelling category (4) as "chaotic" as opposed to the weaker "nonperiodic".This question is addressed in the following.

3.2.2 Chaotic or merely nonperiodic?

We note that it is possible that the system might display nonperiodic bounded behaviour that is phase space filling and yet is not chaotic; motion on a torus for irrational winding number is of this type. To distinguish between these two types of behaviour, it is helpful to study the Lyapunov spectrum of the system: specifically, chaos requires that nearby trajectories diverge exponentially, or equivalently, that there exists at least one positive Lyapunov exponent. The boundedness of the system implies that the Poincaré map at any point has a "fold" in addition to a "stretch". We regard the scalelength that implies that two points are different sides of a fold line as the "system size" because it gives an indication of the spatial extent of the set invariant under the Poincaré map.

We have applied the method of Rosenstein *et al.* [RCL93] to the time series $A(t)$ for $(\gamma_d, \nu_a) = (1.0, 0.01)$, which, as we shall see below, is within a region of nonperiodic behaviour in (γ_d, ν_a) parameter space. The simulation to generate the time series is extremely long: the end time is $t = 3 \times 10^4$. We ignore the data for $t < 5000$ to neglect any transient behaviour. We calculate the reconstruction time as the time delay taken for the autocorrelation function to decay to $1 - 1/e$ of its initial value; this is calculated to be $J = 6.9$. We choose the embedding dimension to be $m = 100$. Having calculated J and chosen m, the analysis was performed using an adaptation of the `L1D2` code [Ros].

A plot of the logarithm of orbit divergence against time is shown in Fig. 3.1. In a chaotic system, we would expect there to be a time interval, after the influence of other exponents has decayed, but before the divergence approaches the system size, in which the behaviour is dominated by the most positive Lyapunov exponent; during that interval the plot would be a straight line. Our data broadly follows this

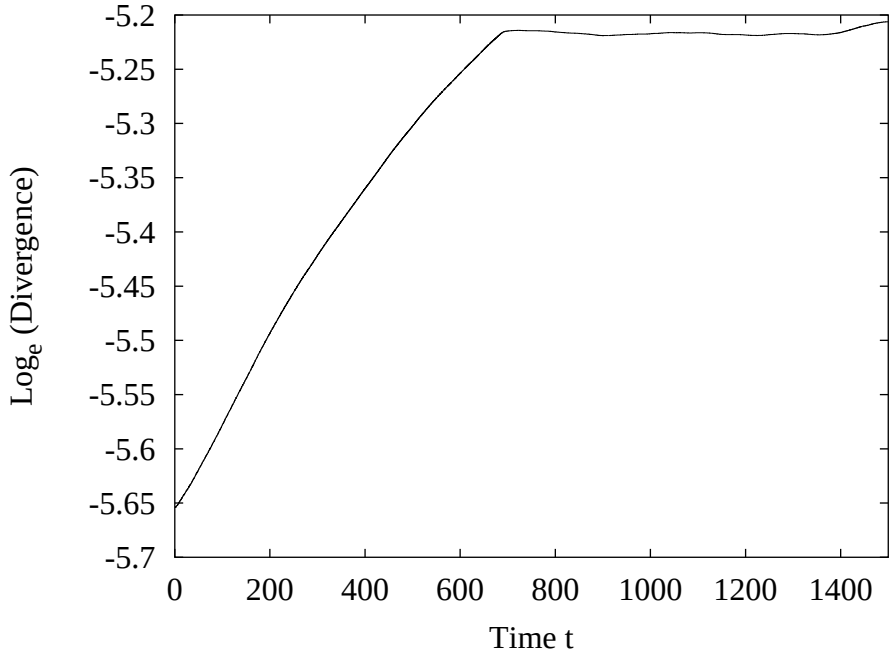

Figure 3.1: Plot of the logarithm of orbit divergence against time for $A(t)$ for $(\gamma_d, \nu_a) = (1.0, 0.01)$. A positive slope indicates the existence of a positive Lyapunov exponent and therefore chaos. The time series saturates when the orbit divergence approaches the system size.

pattern. However, preliminary work that is beyond the scope of this thesis suggests that the observed slope depends to at least some extent on the choice of embedding dimension. The VM(BB) system is driven by the $Q(v)$ term and damped by the ν_a and γ_d terms. This driving and damping may explain the dependence of observed Lyapunov exponent on embedding dimension.

3.3 Bifurcation diagram in (γ_d, ν_a) parameter space

Armed with the theory that we have developed above and the numerical algorithms described in Chapter 4, we are now ready to solve the VM(BB) system of equations given by Eqs. (3.1) and (3.2). Recall that the initial condition that we use is a spatial perturbation of the equilibrium solution $F_0(v)$ (refer to Eqs. (2.34), (2.45) and (2.48)), using the distribution parameters specified in Sec. 3.1 (see Fig. 2.1). We have performed runs of length $3000\omega_p^{-1}$ in the parameter region $0 \leq \gamma_d < 3.5$, $0.01 \leq \nu_a < \nu_{\max}$, where $\nu_{\max} = \min(0.35, \exp(-\gamma_d))$ is chosen to be above the linear stability threshold as computed by direct numerical solution of the dispersion relation (2.53).

The computed behaviour of the fully nonlinear Berk-Breizman system (Eqs. (3.1) and (3.2)) can then be characterised across the whole of (γ_d, ν_a) parameter space as shown in Figure 3.2. The linear stability threshold, shown by a solid line, is calculated using the method presented in Appendix C.1.

The bifurcation diagram shown in Fig. 3.2 summarises the complete solution of the VM(BB) system for these parameter values. That we are able to obtain such a diagram demonstrates that we have achieved a key objective of this project - namely the categorisation of Berk-Breizman phenomenology. This has been made possible only by our development of novel algorithms as described in Chapter 4. Furthermore, by our algorithm work, we have made diagrams of this sort immediately accessible for any choice of initial distribution $F_0(v)$. It is worthy of note that this is without use of a supercomputer, but rather merely with the computational power of ordinary desktop workstations.

The range of applicability of previous work is restricted by the analytical ordering schemes [BBY93, BBP96] to regions of (γ_d, ν_a) parameter space near the origin $\nu_a = \gamma_d = 0$ or near the linear stability threshold $\gamma = 0$. Both regimes are relevant to present day experiments [FBB$^+$98, HFS00] and therefore so is the intervening region. We note that the four types of behaviour occur mainly in well defined regions in parameter space, although there are some outliers, primarily on the borders of the periodic region. These points are a result of the numerical limitations placed on time series correlation outlined towards the end of Appendix B. We conjecture that the regions are simply connected and that this would be confirmed by longer computations.

The linear stability threshold is a local bifurcation because it is where the state $f(x, v, t) = F_0(v), E(x, t) = 0$ changes stability with respect to spatial perturbations. The steady state to periodic and periodic to chaotic boundaries are lines of global bifurcation at which the topological nature of the system's solution changes.

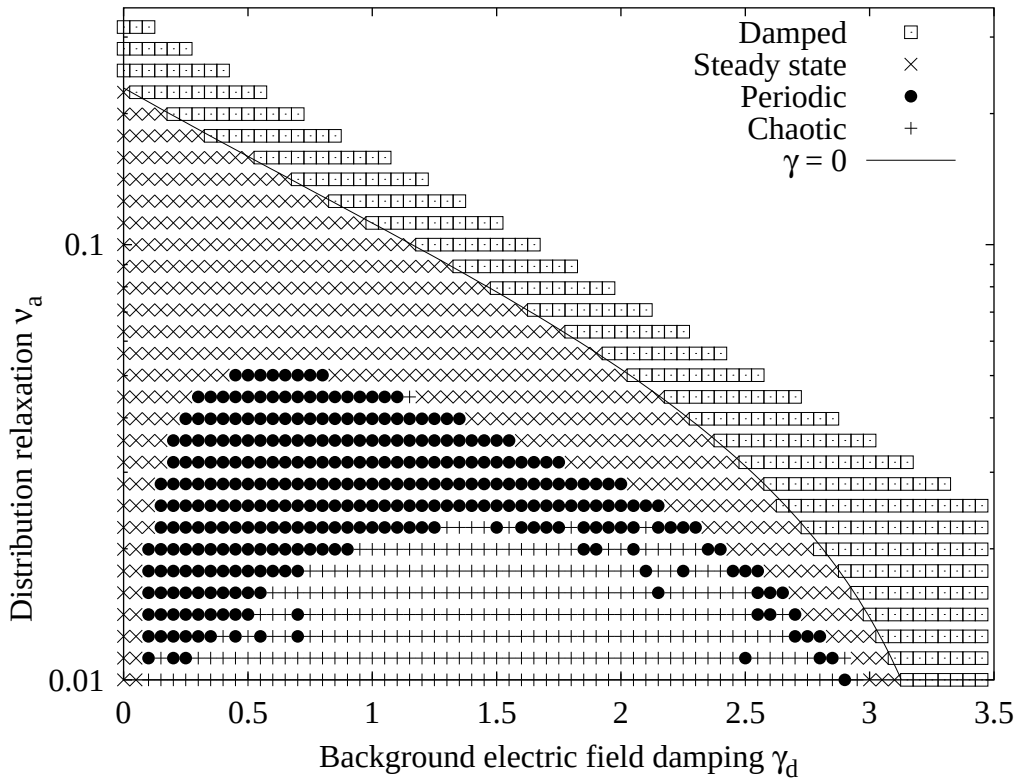

Figure 3.2: Characterization of the behaviour of the Berk-Breizman system across the entire (γ_d, ν_a) parameter space; note the logarithmic scale on the vertical ν_a axis. The four types of behaviour occur in well-defined regions of the parameter space. The solid line is the linear stability threshold, computed numerically directly from the dispersion relation Eq. (2.53); the damped-to-steady-state border agrees well with this calculation.

3.4 Time evolution

3.4.1 Evolution of electric field energy A(t)

To provide examples of the four types of behaviour and illustrate the bifurcation path between them, we have taken a cut along a vertical line in parameter space at $\gamma_d = 1$; representative plots are shown in Figures 3.3 to 3.8 for decreasing values of ν_a. In several of the cases there are transients at small t which later decay.

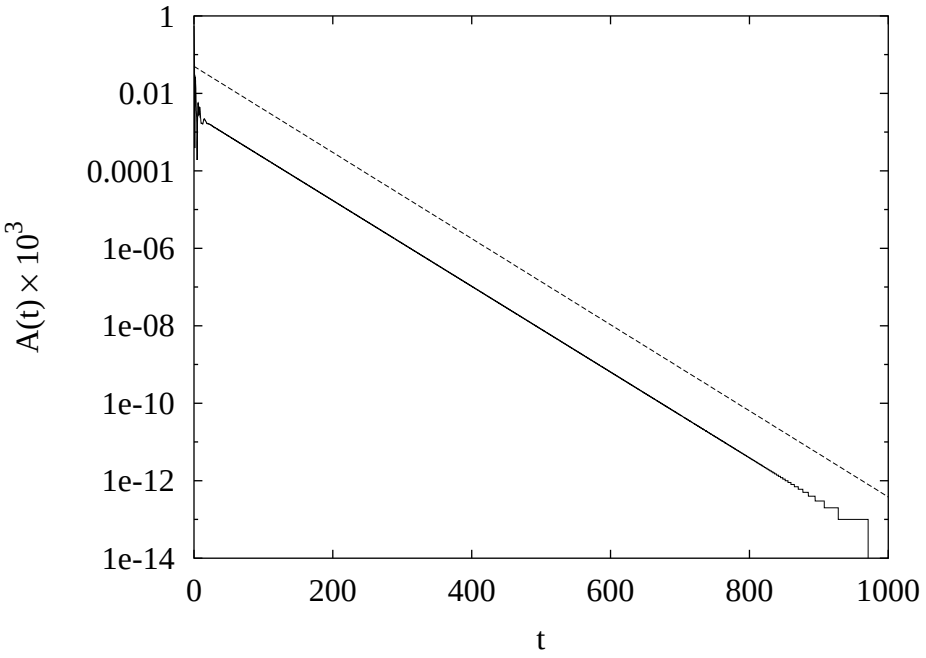

Figure 3.3: Damped behaviour at $(\gamma_d, \nu_a) = (1.0, 0.12589)$; the dashed line shows the growth rate predicted by the dispersion relation Eq. (2.53).

(a) (Fig. 3.3) For large ν_a, the fully nonlinear solution (solid line) exhibits damped behaviour. The electric field energy $A(t)$ goes to zero with a well-defined decay rate. The dashed line represents the corresponding approximate dispersion relation solution $\gamma = -0.0128$ from Eq.(2.53); we note that there is good agreement between the fully nonlinear solutions and the linear analytical approximation. The stepping at small amplitudes is due to the finite precision of the computer.

(b) (Fig. 3.4) As ν_a is reduced, $A(t)$ initially grows exponentially and then saturates at some nonzero value. The example here is underdamped in the sense

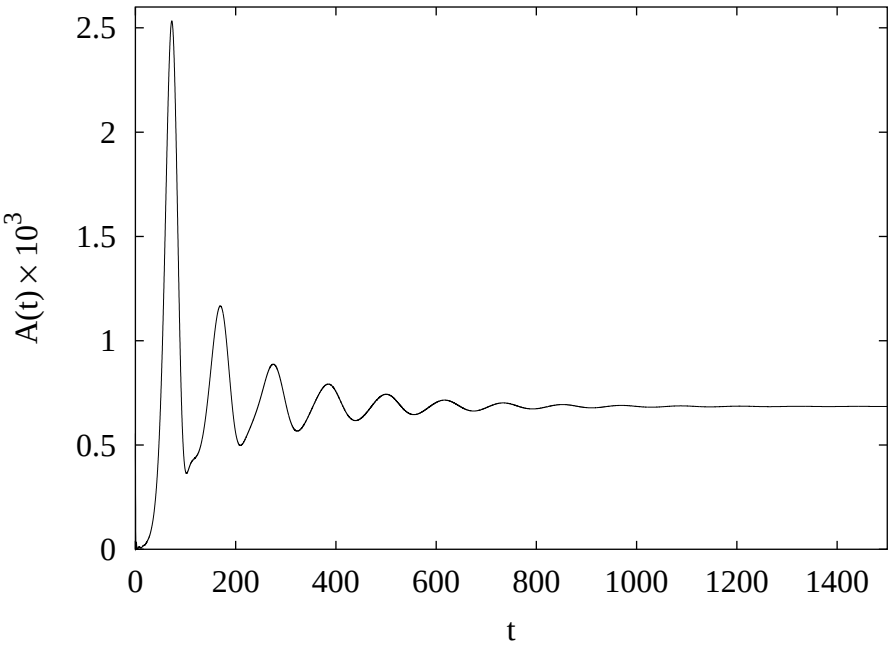

Figure 3.4: Steady state behaviour at $(\gamma_d, \nu_a) = (1.0, 0.05012)$

that it continues to oscillate many times about the saturation value. Both overdamped and critically damped cases also occur.

(c) (Fig. 3.5) As ν_a is further decreased, the system enters a transitional regime where it is difficult to classify the behaviour.

(d) (Fig. 3.6) The system enters a broad region of periodic behaviour. Periodic orbits of this system seem often to feature pairs of peaks - a large peak followed by a smaller peak.

(e) (Fig. 3.7) At still lower ν_a, the system goes through a complex set of bifurcations on the path to chaos. The first bifurcation (shown here) would appear to be the first of a period doubling sequence, as proposed by Heeter *et al.* [HFS00]. However, preliminary results from much longer runs across a small cut in parameter space suggest that this is not the case.

(f) (Fig. 3.8) As ν_a is further reduced, the system becomes chaotic. This confirms the earlier conjecture (made on the basis of a multiple scales argument) that such a regime exists [BBP96]. However, a basic qualitative analysis of our results suggests that this chaos has a characteristic time scale and so is not

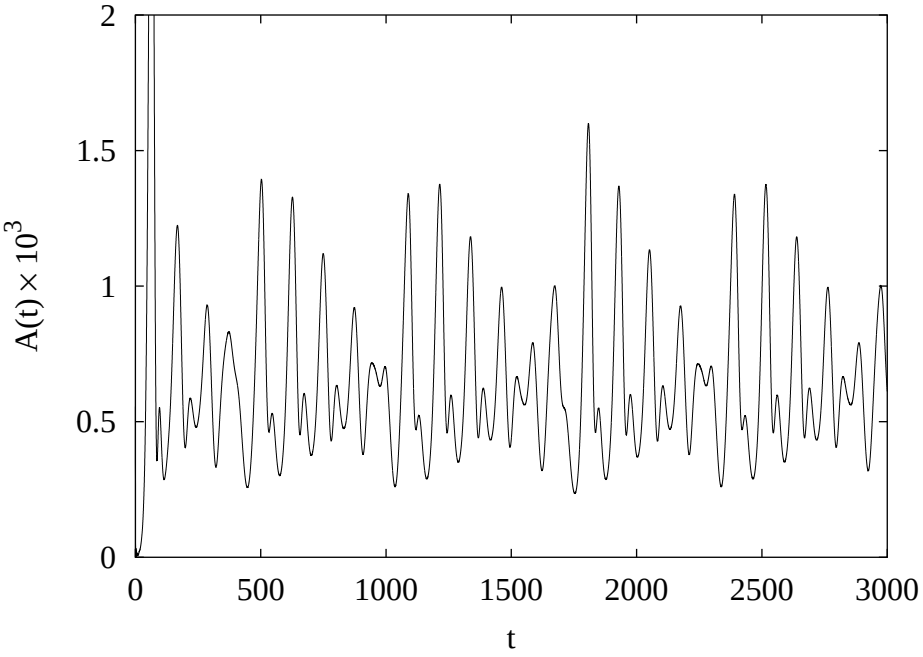

Figure 3.5: Complex behaviour near the steady state / periodic boundary at $(\gamma_d, \nu_a) = (1.0, 0.03981)$

the sort of avalanching chaos observed in the numerical simulations of Berk, Breizman and Pekker [BBP95]. The chaotic regime is extensive in parameter space: it is observed for a broad range of γ_d but only for weak ν_a (see Fig. 3.2).

3.4.2 Evolution of phase space structure

The temporal evolution of the distribution function $f(x, v, t)$ in (x, v) phase space is shown in Fig. 3.9 by four snap-shots of f taken when the system is in its periodic phase with $(\gamma_d, \nu_a) = (1.000, 0.03548)$. For a blow-up of the time series in this case, refer to Fig. 3.10, on which the observation points have been labelled. The snapshots are taken at the locally extreme values of the electric field energy density $A(t)$, which differ by an order of magnitude between the pictures. (The phase of the pictures shown here has been shifted for clarity so that the maximum value of the electric field $E(x, t)$ occurs at the edge of the plots.) These snapshots suggest that small A corresponds to a largely uniform distribution, whilst large A corresponds to significant spatial structure in (x, v) phase space. The structure whose evolution we are observing is a particle "phase space hole". A phase space hole is characterised by an elliptical region corresponding to a potential well. The bottom of the potential

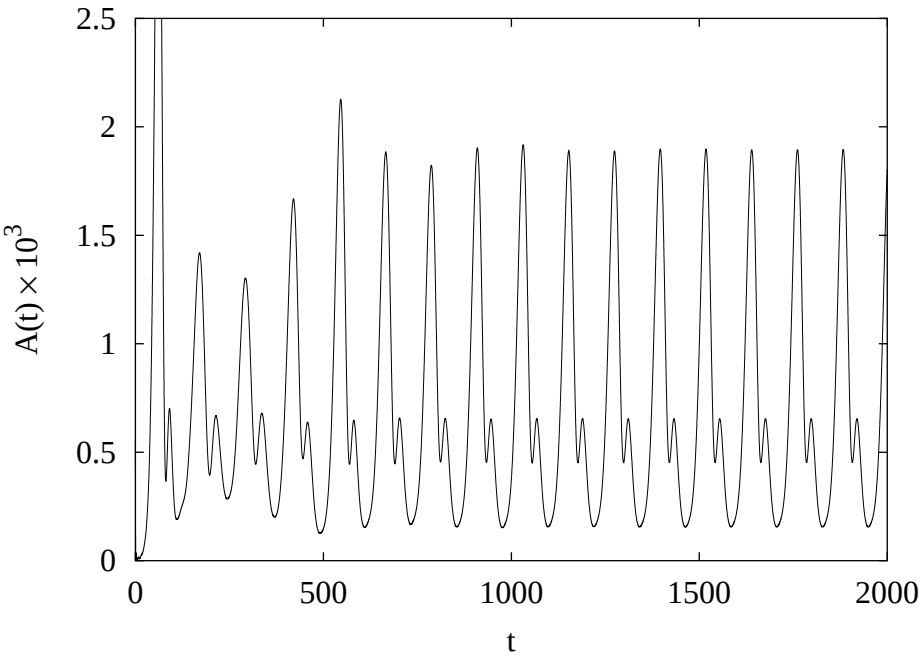

Figure 3.6: Periodic behaviour at $(\gamma_d, \nu_a) = (1.0, 0.03548)$

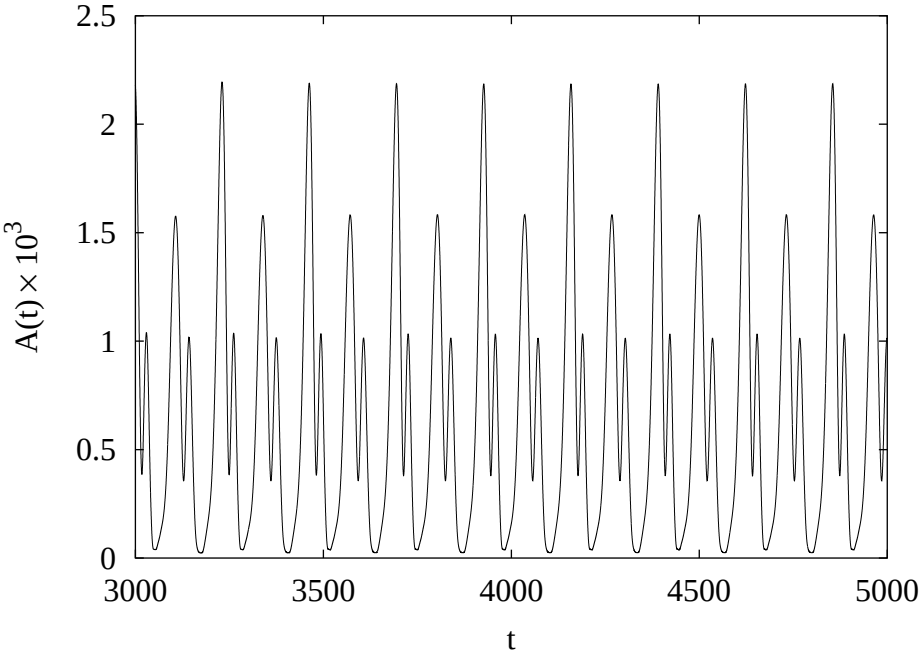

Figure 3.7: Still in the periodic regime, at $(\gamma_d, \nu_a) = (1.0, 0.12589)$, having passed through a period-doubling bifurcation

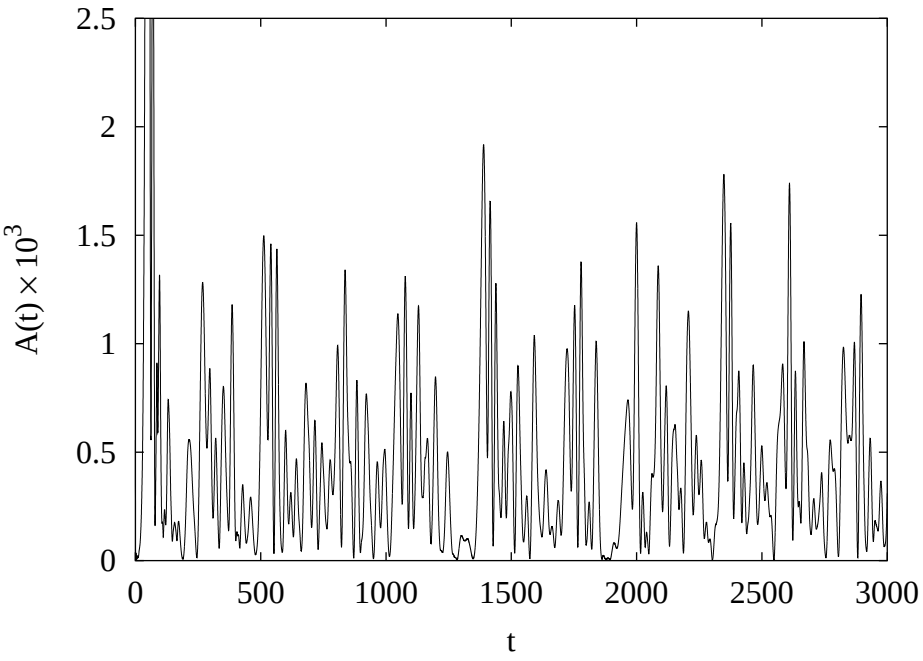

Figure 3.8: Chaotic behaviour at $(\gamma_d, \nu_a) = (1.0, 0.01)$

well is almost devoid of particles; relatively large numbers of particles are either just trapped in the potential well and circulate around it, or have enough energy to pass by it. The wave mode, and the phase space hole, have a characteristic velocity which can be read off the velocity axis In this case the phase speed $v_\phi \approx 4$.

Recall that, in the case $\gamma_d = \nu_a = 0$, the electric field may be determined via Poisson's equation (2.30) or the Displacement Current Equation (DCE) (2.28). From Poisson, it can be seen that the electric field is a functional of the number density (itself a functional of the distribution function) and hence directly reflects any inhomogeneities in the number density. We now ask how the electric field reflects inhomogeneities in the number density when it is computed within the VM(BB) system using (2.39) with non-zero γ_d (and ν_a. To address this question, we can calculate, at each time, what the electric field would be if Poisson's equation were still satisfied. We denote this Poisson-derived electric field by $E^\ddagger(x)$, given by

$$\frac{\partial E^\ddagger}{\partial x} = \int_{-\infty}^{+\infty} f\, dv - 1 \tag{3.4}$$

with associated field energy density $A^\ddagger(t)$:

$$A^\ddagger(t) = \frac{1}{L}\int_0^L E^\ddagger(x,t)^2 dx \tag{3.5}$$

As usual, the actual electric field $E(x,t)$ and electric field energy density $A(t)$ are calculated using Eqs. (3.2) and (3.3) respectively. The time series $A(t)$ and $A^\ddagger(t)$ are compared in Fig. 3.10. There is significant qualitative agreement, although the Poisson-calculated field energy has a larger amplitude. The spatial functions $E(x)$ and $E^\ddagger(x)$ are compared in Fig. 3.11 at time $t = 1296.0$. Again, there is significant similarity, although the Poisson-calculated field has a larger amplitude and a phase lag. These two properties are observed for all the time snap-shots that we have considered. We conclude that there is still a relationship between the strength of the electric field and the degree to which the system is spatially inhomogeneous. However, we have not investigated how the strength of this relationship depends on the parameters (γ_d, ν_a).

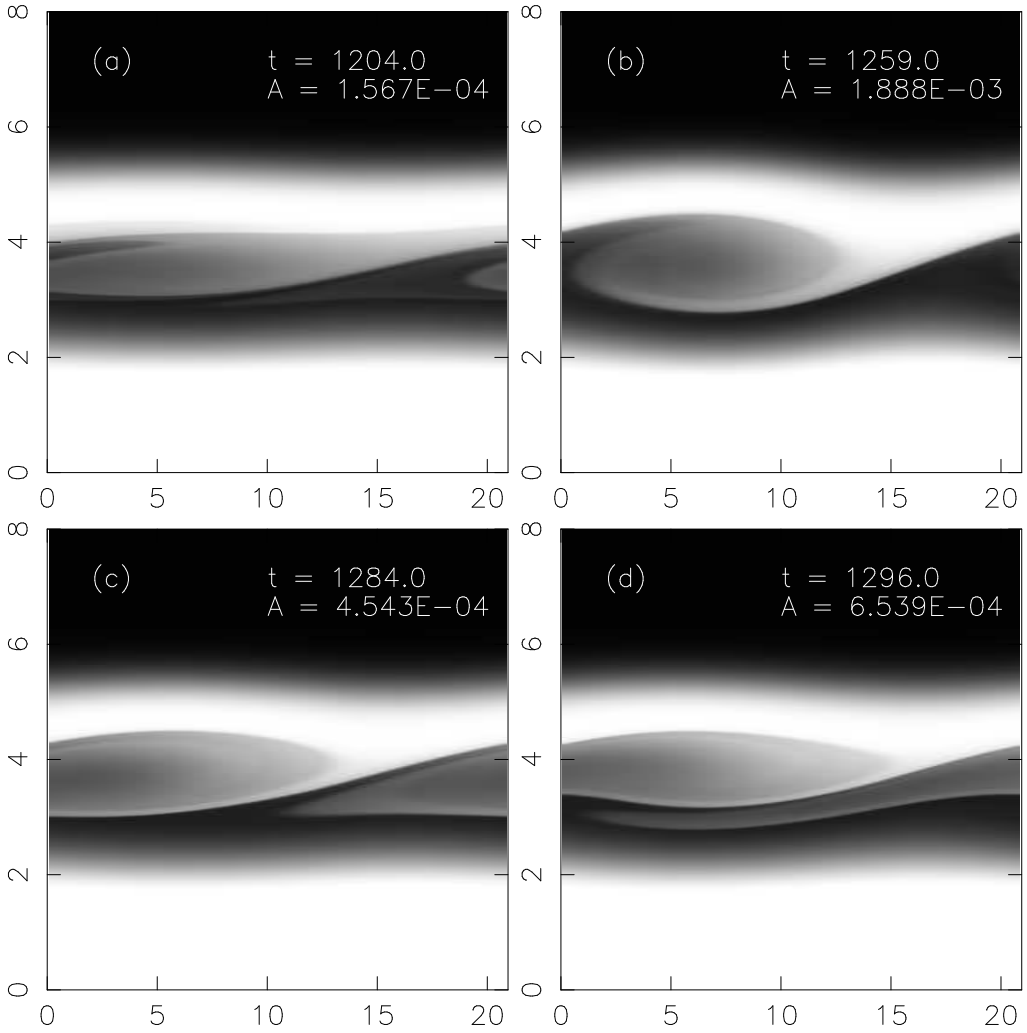

Figure 3.9: Plots of the distribution function in (x, v) phase space; light corresponds to high density and black to low density. The portion of the plot for $v < 0$ is omitted. These figures show the distribution function at times which correspond to the locally extreme values of $A(t)$ for the point in parameter space $(\gamma_d, \nu_a) = (1.000, 0.03548)$, which lies within the periodic regime. There is the bulk dense plasma for $|v| \lesssim 2$. For large A (plot (b)), a large number of particles are trapped in the phase space hole.

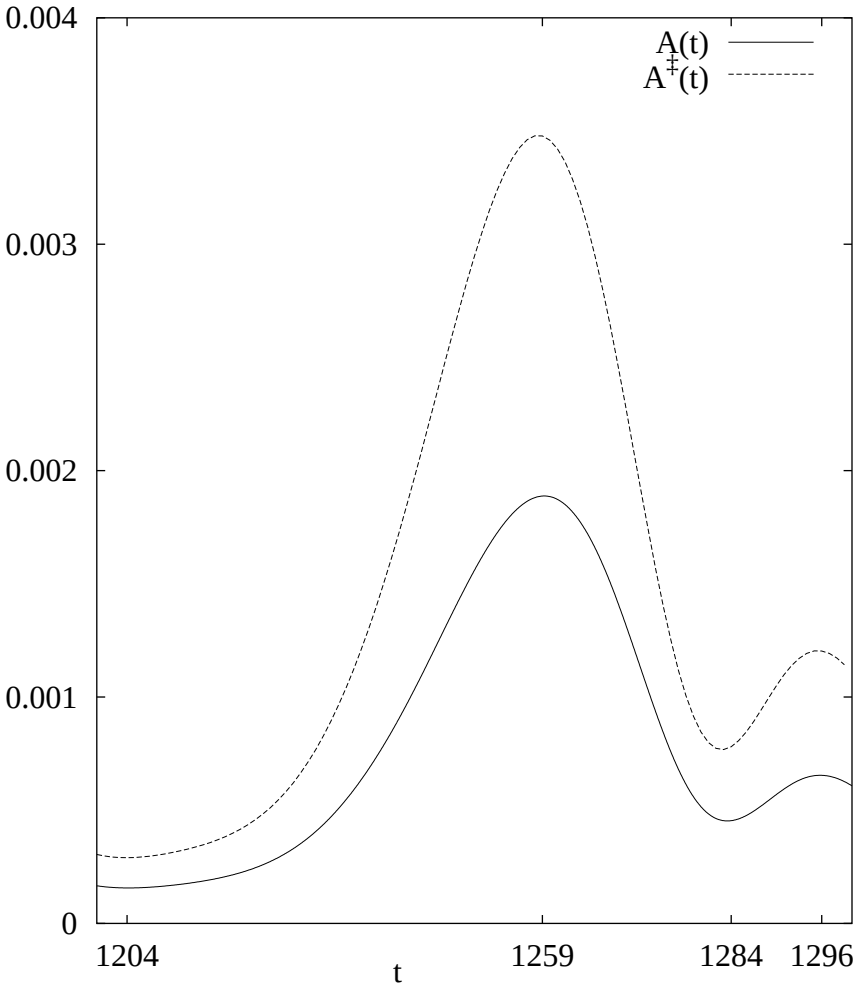

Figure 3.10: The solid line shows the temporal dependence of the electric field energy density $A(t)$ (calculated from Eq. (3.3)) for $(\gamma_d, \nu_a) = (1.000, 0.03548)$. The tick marks on the horizontal axis label local extrema. The time series $A^{\ddagger}(t)$ shows the mean electric field energy density calculated using the number density as if the electric field obeyed Poisson's equation (Eq. (3.5)). We note that there is significant qualitative similarity.

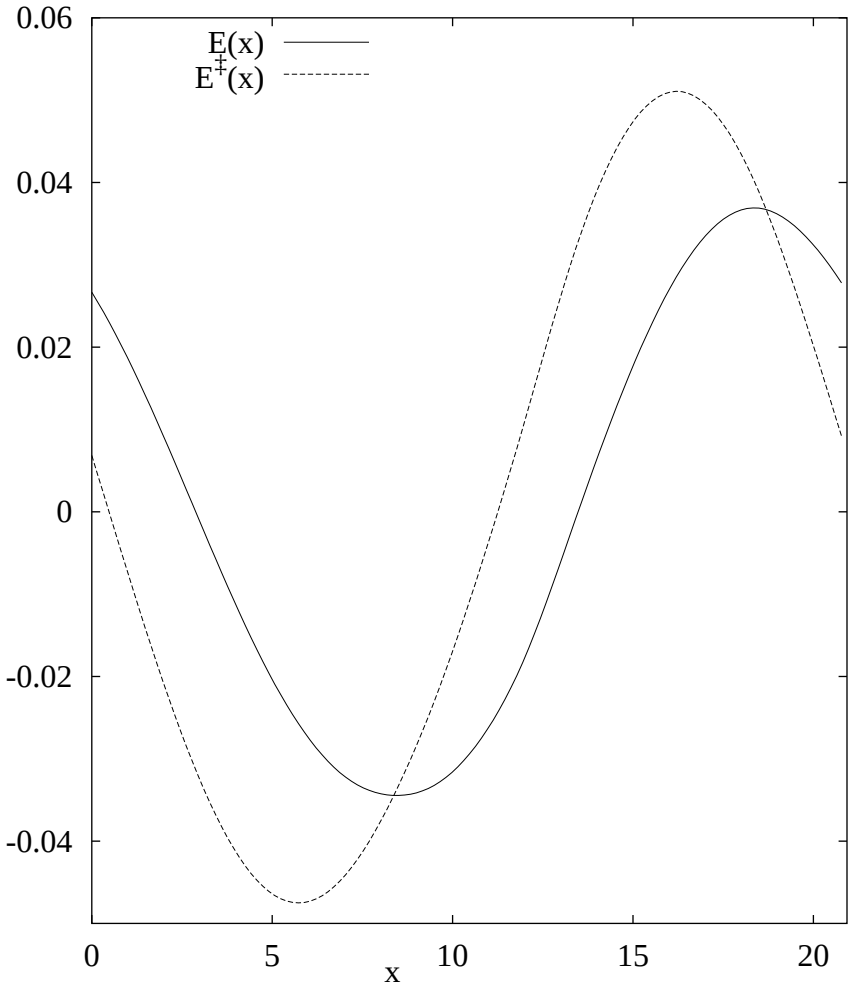

Figure 3.11: The solid line shows the spatial dependence of the electric field $E(x)$ (calculated from Eq. (3.2)) for $(\gamma_d, \nu_a) = (1.000, 0.03548)$ at $t = 1296.0$. The dashed line $E^{\ddagger}(x)$ shows the electric field calculated using the number density as if the electric field obeyed Poisson's equation (Eq. (3.4)). We note that there is significant qualitative similarity. In particular, $E^{\ddagger}(x)$ has a larger amplitude and a phase lag. This appears to be the case at all times.

3.5 Robustness to changes in initial distribution

One may also perform simulations for different shapes of bump-on-tail distribution. Two further examples we have investigated are shown in Fig. 3.12, namely a warm beam distribution and a warm bulk distribution. The corresponding phenomenology of the Berk-Breizman system is shown in Fig. 3.13.

There appears to be no qualitative difference between these two diagrams and the bifurcation diagram Fig. 3.2. Although we have not explicitly verified that the choice of the coding parameters (see discussion in Sec. 4.8.3) is optimal for these later initial conditions, our results suggest that the form of the bifurcation diagram is robust with respect to the particular choice of initial bump-on-tail distribution.

3.6 Summary of results

We have demonstrated that, by using the algorithms described below in Chapter 4, the fully nonlinear self consistent VM(BB) system of equations (2.33) and (2.39) has been solved, thus achieving the primary goal of this project. Application of the helper algorithm described in Appendix B enables us to categorise the system's evolution with time by analysing time series of the electric field energy, thereby enabling us to draw diagrams in (γ_d, ν_a) parameter space such as Figure 3.2. Previous work has been constrained to various limiting parameter regimes. Our direct numerical technique allows a fully nonlinear exploration of the entire parameter space. For our particular choice of initial distribution $F_0(v)$ (see Sec. 3.1), we have shown that the system behaviour can be categorised into four types (defined in Sec. 3.2.1): damped, steady state, periodic and chaotic. We have shown in Sec. 3.2.2, by consideration of Lyapunov exponents, that this fourth category is genuinely chaotic and not merely nonperiodic. Each of these four types of behaviour occur in well defined simply connected regions of parameter space. We have indicated in Sec. 3.5 that the qualitative nature of the categorisation diagram appears robust to changes in the initial distribution $F_0(v)$.

Consideration of the phase space evolution indicates that the underlying physical process driving the system is the reformation cycle of a phase space hole at the foot of the bump, which itself is a manifestation of the two stream instability.

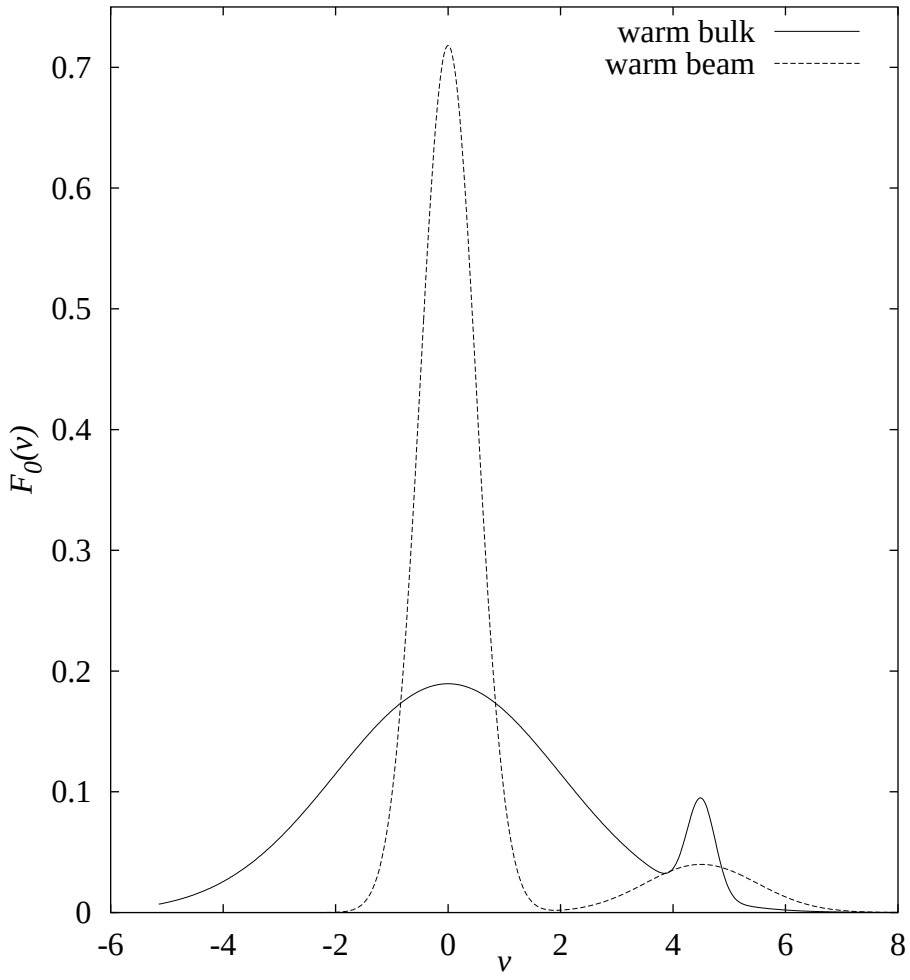

Figure 3.12: Alternative bump-on-tail distributions. The warm beam distribution ($\eta = 90\%$, $v_c = 0.5$, $v_t = 1.0$) is plotted as the dashed line, and the warm bulk distribution ($\eta = 95\%$, $v_c = 2.0$, $v_t = 0.5$) as the solid line. In both cases (as before) the mean beam velocity $v_b = 4.5$.

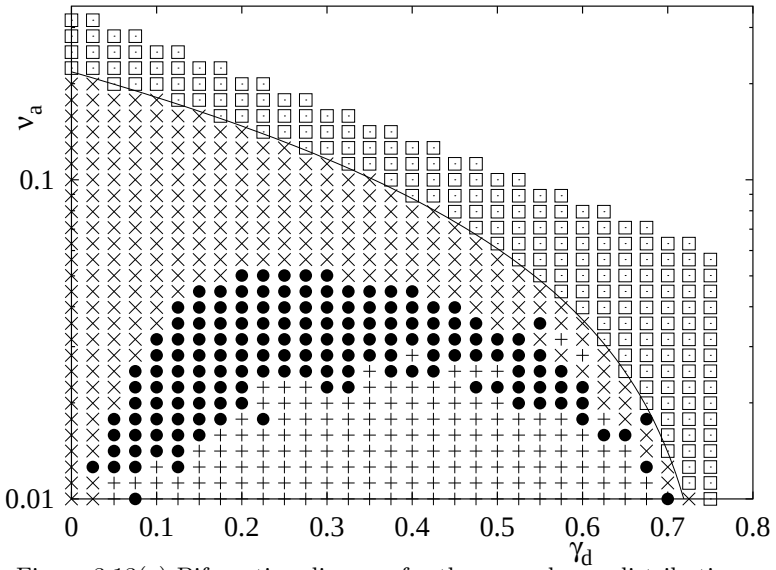

Figure 3.13(a) Bifurcation diagram for the warm beam distribution

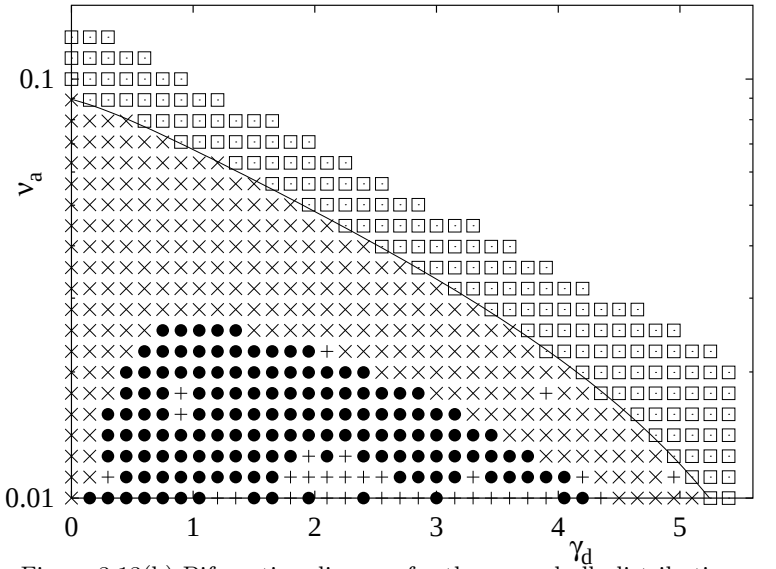

Figure 3.13(b) Bifurcation diagram for the warm bulk distribution

Figure 3.13: Classification of the behaviour found in (γ_d, ν_a) parameter space for the alternative initial distributions of Fig. 3.12: (a) warm beam (b) warm bulk. (For the symbol key, refer to Fig. 3.2.) There is strong similarity between these two categorization diagrams and that shown in Fig. 3.2, suggesting that the bifurcation path is robust to changes in the initial distribution. The small beam gradient (in the warm beam case) and the small beam width (in the warm bulk case) is likely to cause the numerical results to be slightly less accurate.

Now that the model has been solved, the way is open for deeper comparison with experiment. The feedback cycle that has now been made possible between the Berk-Breizman theory and experimental data in principle allows further modifications to the theory and thereby a greater understanding of the physical mechanisms at work in a real fusion plasma. We indicate briefly in Chapter 5 how this work might proceed. A key element in future comparisons would be a systematic approach, as here, to the categorisation of the time series that arise from experimental observations.

Chapter 4

Numerical method

4.1 Background

In this chapter we demonstrate how one may solve the VM(BB) Eqs. (2.33) and (2.39) accurately and with the minimum of computational cost. Our approach is to design a Vlasov-Poisson solver and then adapt it to solve the VM(BB) system. Our Vlasov-Poisson solver relies on combining the methods of Strang splitting [Str68] and the piecewise parabolic method [CW84]. It is a logical development of the ground-breaking method of Cheng & Knorr [CK76]; a full account is given in Arber & Vann [AV02].

The chapter is organised as follows. We begin by introducing the time splitting and reviewing conservative advection schemes. We describe each of a number of rival codes and compare their performance in a range of tests. Having picked the optimal Vlasov-Poisson solver, we proceed to show how the time splitting may be adapted to solve the Vlasov-DCE and then the full VM(BB) system. We conclude by rigorously benchmarking our choice of coding parameters for the main simulations.

4.2 Aside: non-Eulerian approaches

In this thesis we restrict ourselves to Eulerian grid methods, but should consider for a moment what other types of method are sometimes used, and why we do not consider them for bump-on-tail studies.

Particle in cell (PIC) methods approximate the plasma by a finite number of

macro-particles which move in the self-consistent fields computed by taking moments on a background mesh [BL91]. The key drawback with this approach is that the numerical noise only decreases as $1/\sqrt{N}$ where N is the number of macro-particles in any particular computational cell. This problem is particularly pronounced in studies where the fine-scale structure of $f(\mathbf{r}, \mathbf{v}, t)$ is important, or where the physics of interest is in the high energy tail of the distribution in which there are only a relatively small fraction of the total number of macro-particles. Even with these limitations the PIC approach continues to produce accurate results when the high energy tail is not significant and a sufficiently high N can be maintained to resolve the broad distribution function. Recent examples of the application of PIC methods range from studies of laser-plasma scattering [VDB] to simulations of the lunar wake [BC01].

Previous work on the direct solution of Vlasov's equation has also made use of spectral methods, e.g. [AHKM70], and semi-Lagrangian methods, e.g. [SRBG99]. In this thesis we restrict attention to grids in the physical x and v coordinates, but note briefly that these methods suffer the same problems as high ($> 1^{st}$) order unlimited Eulerian schemes. A positivity preserving, or monotonicity preserving, spectral scheme has yet to be developed.

4.3 Time splitting approach

We begin by consideration of the Vlasov-Poisson system given by Eqs. (2.23) & (2.30):

$$\frac{\partial f}{\partial t} = -v\frac{\partial f}{\partial x} - E\,\frac{\partial f}{\partial v} \tag{4.1}$$

$$\frac{\partial E}{\partial x} = \int_{-\infty}^{+\infty} f\,dv - 1 \tag{4.2}$$

In this case, the electric field E is uniquely defined by the distribution function f, so we can consider $E(x,t) = E[f]$. We can then write the equations in the form

$$\frac{\partial Z}{\partial t} = Y[Z] \tag{4.3}$$

where $Z = f$, $Y = Y_1 + Y_2$, and

$$Y_1[Z] = -v\frac{\partial f}{\partial x} \tag{4.4}$$

$$Y_2[Z] = -E\,\frac{\partial f}{\partial v} \tag{4.5}$$

(The reason for the rather perverse-seeming notation is that we are able to use it again later for more complicated systems.)

We can then apply the Strang splitting [Str68] formula

$$\Phi_Y^{\Delta t}\left[Z_0\right] = \Phi_{Y_1}^{\frac{1}{2}\Delta t} \circ \Phi_{Y_2}^{\Delta t} \circ \Phi_{Y_1}^{\frac{1}{2}\Delta t}\left[Z_0\right] + \mathcal{O}\left(\Delta t^3\right) \tag{4.6}$$

where the flow operator Φ is defined by

$$\left\{\partial_t Z = Y[Z] \text{ and } Z(t=0) = Z_0\right\} \;\Rightarrow\; Z(t) = \Phi_Y^t[Z_0] \tag{4.7}$$

So by this formula, if we are able to solve each of the systems

$$\frac{\partial Z}{\partial t} = Y_j[Z] \tag{4.8}$$

to second order in time, then we are able to solve the entire system Eq. (4.3) to second order in time.

This second order time splitting formula is valid for any system of the above form if Y_1 and Y_2 have continuous second derivatives. In our case, this is not strictly true. We approximate the advections governed by Y_1 and Y_2 by operations on the $N_x \times N_v$ Eulerian grid. Methods that can be written as constant coefficient finite difference operators (for example the flux balance method below) represent matrix operations on the grid, which clearly have continuous (in fact vanishing) second derivatives. However, the other methods detailed below incorporate nonlinear limiters which introduce kinks (i.e. discontinuities in the first derivative) into the numerical operators simulating the advection.

The Strang time splitting formula can also be extended to problems in which there are more terms in the operator sum by iteratively applying the splitting formula to the middle term in Eq. (4.6).

So the common time-stepping algorithm that we use below to compare the various codes for the Vlasov-Poisson case is as follows:

- Evolve $\partial_t f + v\partial_x f = 0$ for a time $\Delta t/2$.

- Solve Poisson's equation for the electric field.
- Evolve $\partial_t f + E\partial_v f = 0$ for a time Δt (noting that this does not change E).
- Finally evolve $\partial_t f + v\partial_x f = 0$ for a time $\Delta t/2$.

So the problem has been reduced to solving each of the x or v updates, each of which is a linear advection with constant speed, i.e. solves an equation of the form

$$\partial_t U + c\,\partial_x U = 0 \tag{4.9}$$

where c is not a function of U or x.

The numerical problem is therefore reduced to finding an accurate, and fast, constant speed advection solver. This is clearly not a new problem in computational physics! The question that we address is how well classical advection solvers can be made to perform when applied to the Vlasov equation with its alternating x and v advections coupled through a self-consistent field.

4.4 Review of conservative advection solvers

Thinking of U in Eq. (4.9) as a fluid density, recall that the evolution of the advection equation (4.9) for a time Δt is simply a uniform shift of the fluid by a displacement $c\,\Delta t$. Our problem is that we know U only at a set of discrete grid points $\{x_j = j\,\Delta x\}$. There are two particular properties that we hope to find in an advection solver.

(a) The method should not introduce false extrema. This is equivalent to it preserving monotonicity i.e. requiring that if, for $0 < \lambda < 1$, $U^n_{i-1} < U^n_i < U^n_{i+1}$, then $U^{n+1}_i \leq U^{n+1}_{i+1}$ (and similarly for monotone decreasing) where $\lambda = c\,\Delta t/\Delta x$.

(b) The method should not accentuate already existing extrema i.e. for $0 < \lambda < 1$, if $U^n_{i-1} < U^n_i > U^n_{i+1}$, then $U^n_i \geq \max\{U^{n+1}_i, U^{n+1}_{i+1}\}$ (and similarly for minima).

We remark that properties (a,b) together imply the method is positivity preserving and total variation diminishing.

One solution would be to spline interpolate between the grid points by some function $\tilde{U}(y)$ and write $U(y_i, t+\Delta t) = \tilde{U}(y_i - \lambda, t)$, where $y = x/\Delta x$ (so $y_i = i$) and λ is the distance in y by which the fluid must be shifted. However, by a corollary of Godunov's theorem, any interpolation scheme that is higher than first order breaks properties (a,b).

In this chapter we consider a number of schemes all of which are cast in conservative form. They work in the following way:

- At any time t^n, we consider $U_i^n = U(y_i, t^n)$ to be the amount of fluid in the cell $i - 1/2 < y < i + 1/2$.
- Using the $\{U_j\}$, we construct a function $\phi(y)$ to represent the amount of fluid at each point y. Note that ϕ need not be continuous everywhere
- Compute the amount of fluid flowing (in the positive direction) through the boundary between the i-th cell and the $(i+1)$-th cell.

$$\Phi_{i+1/2} = \int_{i+1/2-\lambda}^{i+1/2} \phi(y) dy \tag{4.10}$$

- Evolve the system by one timestep:

$$U_i^{n+1} = U_i^n - \left(\Phi_{i+1/2} - \Phi_{i-1/2}\right) \tag{4.11}$$

In all cases the timestep, Δt, is limited so that $\Delta t = \min(\Delta x/v^{max}, \Delta v/|E|_{\max})$, where v^{max} is the largest velocity allowed on the grid and $|E|_{\max}$ is the maximum value of the absolute magnitude of the electric field.

Since the advection sweeps are always with constant speed, the Courant-Friedrichs-Levy (CFL) condition on the size of the time step (namely $|\lambda| < 1$) can be circumvented by first shifting the solution by an integer number of grid points and then using the algorithms described below for the remaining fractional step. This approach has not been used in any of the results in Section 4.6 as it is the spatial accuracy of the schemes themselves which is being assessed there. However, in the main simulations, the results of which are display and discussed in Chapter 3, we control the time step using the formula

$$\Delta t = \max\left(\lambda_{\max} \cdot \min(\Delta x/v^{max}, \Delta v/|E|_{\max}), \Delta t_{\max}\right) \tag{4.12}$$

where we choose the numerical parameters $\lambda_{\max} = 3.0$ and $\Delta t_{\max} = 0.1$. (Justification for this choice of $\lambda_{\max}$ and $\Delta t_{\max}$ is given below in Sec. 4.8.3.

4.5 The Advective Codes

All of the codes solve for the distribution function f on a fixed Eulerian grid with grid spacings $(\Delta x, \Delta v)$ in spatial and velocity coordinates, respectively. All codes use the same time-splitting algorithm and the same FFT solver for the electric field. Thus the only differences between the schemes are in the implementation of the advection steps in the x and v directions. In this way all differences in accuracy can be attributed to the different advection schemes alone. We have not compared these results with PIC codes, semi-Lagrangian Vlasov solvers or spectral Vlasov solvers. The aim throughout has been to determine the best fixed Eulerian grid advection scheme for Vlasov problems. Attention is also restricted to time dependent 1D problems, i.e. problems involving one spatial dimension and one velocity dimension, but there is no reason why these schemes cannot be generalized to multidimensional problems.

4.5.1 Flux balance method (FB)

The first advection solver to be considered is the Flux Balance method (FB). The interpolation function $\phi(y)$ is piecewise linear and is discontinuous at cell boundaries:

$$D_i = (U_{i+1} - U_{i-1})/2 \tag{4.13}$$

$$\phi(y) = U_i + D_i\ (y - y_i), \quad y \in [i - 1/2, i + 1/2] \tag{4.14}$$

This then defines a trapezium, through the midpoint of the cell with the specified gradient, bounded in x by the cell boundaries. The flux $\Phi_{i+1/2}$ is the flux through the right hand side boundary determined from the area of the trapezium which would be advected through this boundary when moved at constant speed c; it is computed from Eq. (4.10):

$$\Phi_{i+1/2} = \begin{cases} \lambda U_{i+1} - \dfrac{\lambda D_{i+1}}{2}\,(1+\lambda) & \text{if } \lambda \le 0 \\ \lambda U_i + \dfrac{\lambda D_i}{2}\,(1-\lambda) & \text{if } \lambda > 0 \end{cases} \tag{4.15}$$

The amount U_i of fluid in the i-th cell is then updated via equation (4.11). There are several problems with this method: it is only second order accurate in space and there is no guarantee that it either preserves monotonicity or does not introduce false extrema. When coupled with smoothing and averaging techniques, to dissipate fine-scale structure, this approach has been shown [Fij99] to be successful for a variety of Vlasov problems.

4.5.2 Van Leer-limited scheme (`VL`)

To obtain what we shall hereafter refer to as the `VL` method, we adapt the `FB` method as follows:

- Estimate size of the gradient from a third order upwind scheme [You82]:

$$D_i = \begin{cases} \dfrac{2-\lambda}{3}\left(U_{i+1}-U_i\right) + \dfrac{1-\lambda}{3}\left(U_{i+2}-U_{i+1}\right) & \text{if } \lambda \leq 0 \\ \dfrac{2-\lambda}{3}\left(U_{i+1}-U_i\right) + \dfrac{1-\lambda}{3}\left(U_i-U_{i-1}\right) & \text{if } \lambda > 0 \end{cases} \tag{4.16}$$

- Apply the following van Leer gradient limiter to the gradients D_i before calculating the cell boundary fluxes $F_{i+1/2}$:

$$D_i = s\ \min(|D_i|\Delta x,\, 2|U_{i+1}-U_i|,\, 2|U_i-U_{i-1}|)$$

  where

$$s = \begin{cases} \text{sign}(U_{i+1}-U_i) & \text{if sign}(U_{i+1}-U_i) = \text{sign}(U_i-U_{i-1}) \\ 0 & \text{otherwise} \end{cases} \tag{4.17}$$

- Compute ϕ as in Eq. (4.14) and thence Φ_i as in Eq. (4.15).

Note that in this scheme the limiter restricts the overall order to second order and there is therefore little point insisting on a third order initial estimate for the gradient in the first step above. However this third order scheme has the same computational cost as second order and is therefore commonly used instead. The van Leer limiter forces the method to be monotonicity preserving and prevents it from accentuating already existing extrema. It is therefore positivity preserving. This limiter has also been applied directly to the `FB` method; there is no significant difference between the results from such a scheme and those from `VL` and only the

VL results are presented here. However, there are significant differences between results obtained from the FB method (without gradient limiters) and those from VL. These differences will be highlighted in this chapter.

4.5.3 Piecewise parabolic method (PPM)

As a next step in improving the accuracy of the scheme, the piecewise linear function used in FB and VL can be replaced by a piecewise parabolic function [CW84]:

- Compute a value for U at the cell boundaries (i.e. $U_{i+1/2}$ for each i) from a fourth order interpolation scheme, which itself is limited to ensure that $U_{i+1/2} \in [U_i, U_{i+1}]$.
- Compute $\phi(y)$ on each cell as a parabolic function which passes through the previously calculated boundary values for each cell and which has the correct mean i.e. $\int_{i-1/2}^{i+1/2} \phi(y)dy = U_i$
- Apply a cell-wise limiter to ϕ: if U_i is a local extremum, then set $\phi = U_i$ in the cell; if the interpolating parabola $\phi(y)$ achieves an extremum in the cell, then reset one of the boundary values (making ϕ discontinuous there) so that ϕ is then monotone and so that $d_y\phi = 0$ at the opposite edge to the resetting.

This method is monotonicity preserving and does not accentuate already existing extrema. For uniform grids, as used here, this scheme is formally third order accurate away from extrema and first order at extrema. A variation of this method which is used in some of the tests below is to calculate $\Phi_{i+1/2}$ without applying limiters to ϕ. This is called the PPM1 scheme. A similar high order geometric reconstruction has been used previously [FSB01] but this was a third order scheme and imposed positivity but not monotonicity.

4.5.4 Flux corrected transport (FCT)

The flux corrected transport algorithm [BB73, BB76] limits not the interpolating function ϕ, but the resulting flux Φ:

- Update U_i by the first order upwind method, which gives

$$\phi(y) = U_i \qquad y \in [i - 1/2, i + 1/2] \tag{4.18}$$

Call the result $\tilde{U}_i$. This method is well-behaved (in the sense that it is monotonicity preserving and does not accentuate already existing extrema), but is very diffusive.

- Now compute the first order upwind fluxes for $\tilde{U}_i$; call them $\Phi^{lo}_{i+1/2}$
- Also compute fluxes for $\tilde{U}_i$ from a high order method (the high order method used here is second order Lax-Wendroff: see Laney [Lan98] Sec. 17.2); call them $\Phi^{hi}_{i+1/2}$.
- Define the corrective flux

  $$\Phi^{c}_{i+1/2} = s\ \max\left(0, \min\left[s\left(\tilde{U}_{i+2} - \tilde{U}_{i+1}\right), |\Phi^{hi}_{i+1/2} - \Phi^{lo}_{i+1/2}|, s\left(\tilde{U}_i - \tilde{U}_{i-1}\right)\right]\right)$$

  where $s = \text{sign}(\tilde{U}_{i+1} - \tilde{U}_i)$
- Add the corrective anti-diffusive flux $U^{n+1}_i = \tilde{U}_i - (\Phi^{c}_{i+1/2} - \Phi^{c}_{i-1/2})$

The flux limiter allows the addition of as much anti-diffusive flux as possible without breaking monotonicity preservation or allowing the accentuation of already existing extrema. In all of the tests below a fourth order scheme has been used to calculate the high order flux so that the `FCT` approach is formally of higher order than the `PPM` method for smooth, well-resolved functions. The FCT approach has been used previously in Vlasov simulations [TLP]

4.5.5 High order compact finite difference (`Compact`)

As a higher order scheme we have tested a compact finite difference approach [Lel92]. Here the time update is fourth order Runge-Kutta with each intermediate step of the form $U^{n+1}_i = U^n_i - c\Delta t\, U'_i$. The local estimates of gradients U'_i are found from the sixth order compact equation

$$\frac{1}{3}U'_{i-1} + U'_i + \frac{1}{3}U'_{i+1} = \frac{1}{36\Delta x}(-U_{i-2} - 28U_{i-1} + 28U_{i+1} + U_{i+2})$$

Fine-scale structures in the distribution functions are removed by applying a compact filter to the data after each timestep of the form

$$\alpha\hat{U}_{i-1} + \hat{U}_i + \alpha\hat{U}_{i+1} = a_0U_i + a_1(U_{i-1} + U_{i+1}) + a_2(U_{i-2} + U_{i+2}) + a_3(U_{i-3} + U_{i+3})$$

where $a_0 = (11+10\alpha)/16$, $a_1 = (15+34\alpha)/64$, $a_2 = (-3+6\alpha)/32$, $a_3 = (1-2\alpha)/64$, and throughout this work $\alpha = 0.45$, where $\hat{U}_i$ are the new filtered values. This method does not maintain positivity or monotonicity. The motivation for testing a compact scheme comes from spectral transform methods for solving Vlasov's equation. The aim in this chapter has been to focus on Eulerian fixed grids and thus the compact approach is chosen as the closest that grid based methods can get to spectral accuracy. This approach can only remove fine scale filamentation by filtering. The coefficients for the filter were found to be the best choice from the original work on compact schemes [Lel92] for the problems tested.

4.6 The Test Problems

In this section we test each of the above schemes as the advection component in a Vlasov-Poisson solver for three test problems. The three tests are

1 Linear Landau damping. This problem tests the linear stability and accuracy of the schemes.

2 Nonlinear bump-on-tail instability. This problem tests the ability of the schemes to correctly simulate systems that are linearly unstable and that exhibit strongly nonlinear behaviour.

3 Ion acoustic turbulence. This two species problem tests the schemes' performance on a problem with many spatial modes.

In each case we are interested in the phase space resolution and associated computational cost that is required to obtain the correct result. We seek to understand what properties a scheme should possess in order that it reproduces the correct physical results in simulation.

In all of the following tests we solve for the electron distribution function f_e, and where appropriate for the ion distribution function f_i, on an (x, v) grid with (N_x, N_v) equally spaced points. The computational domain is defined in $0 < x < L$ with $-v_e^{max} < v_e < v_e^{max}$ for the electrons and $-v_i^{max} < v_i < v_i^{max}$ for the ions. The parameters of type v^{max} are deemed to be of sufficient magnitude if the flux across them is negligible. Unless otherwise stated $v_i^{max} = v_e^{max}/M_r^{1/2}$ where the mass ratio

$M_r = m_i/m_e$. Spatial boundaries are periodic. Tests which do not solve for f_i assume a uniform background ion number density. Δt is fixed on each timestep so that $\Delta t = \min(\Delta x/v_e^{max}, \Delta v_e/|E|_{max})$ where Δv_e is the grid spacing in the electron velocity.

4.6.1 Linear Landau damping

This is the problem of the linear Landau damping of a Langmuir wave. The initial configuration is

$$f_e = (1 + \alpha \cos(kx))\, exp\left(-v_e^2/2\right)/\sqrt{2\pi}$$

where $\alpha = 0.01$, $L_x = 4\pi$, $v_e^{max} = 4.5$ and $k = 0.5$. The ions are stationary. For these results we fix $N_x = 32$ and run tests with $N_v = 16, 32$ and 64. The solution directly obtained from the linear dispersion relation for this problem, and calculated using the method presented in Appendix C.2, gives an oscillation frequency of $\omega = 1.41566$ and a damping rate of $\gamma = -0.153359$. Each test code is compared against these values by fitting a straight line across the maxima of $\log_e(E_1)$ vs. t, where E_1 is the absolute value of the amplitude of the fundamental harmonic of the electric field. Figure 4.1 shows the evolution of $\log_e(E_1)$ for the codes `FB`, `Compact`, `FCT` and `PPM` for $N_v = 64$. Note that the values of E_1 are from the unnormalized FFT routine and should be divided by $N_x/4$ to get the real amplitudes. However since it is only the gradient which is tested here this is unimportant. The results from the `VL` scheme are similar to those from the `FB` method and are not presented here. In each case the solid straight line is the analytic result for γ given above.

The percentage errors in ω and γ for each scheme on a variety of resolutions are shown in Table 1. To avoid problems with the recurrence effect (see Sec. 4.8.2 for an explanation of the recurrence phenomenon) the best fit line used to calculate the effective γ for each test was limited to only those maxima in E_1 which occur before $T_R/2$ and thus the time over which γ is estimated is different for each of the resolutions. Note that the analytic result for γ is only valid for late time. Thus the early maxima and the deviation from linear decay before $T_R/2$ will both contribute to the error estimates in Table 1 even though the early maxima are actually not necessarily in error when they differ from the fitted line. The same is also true of later times as the linear theory of Landau damping breaks down before τ_b, the

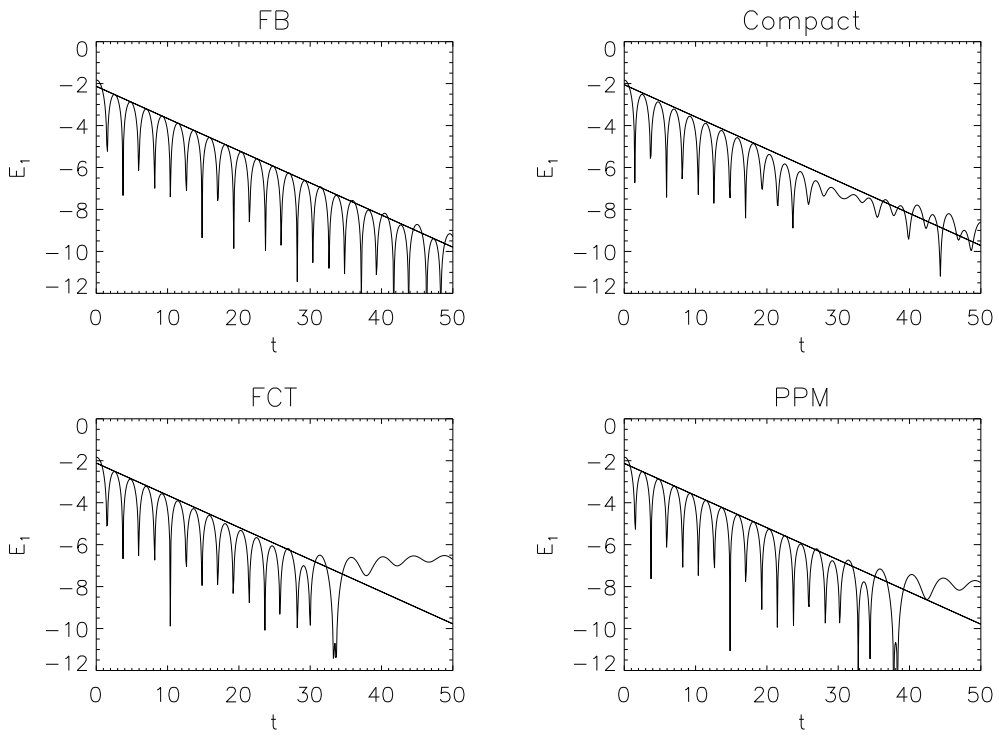

Figure 4.1: Time evolution of the amplitude of the fundamental mode of the electric field for the linear Landau damping test with $(N_x, N_v) = (32, 64)$. The solid line represents the decay rate obtained directly from the linear dispersion relation.

bounce time of trapped electrons. In this normalisation $\tau_b \simeq 2\pi/\alpha^{1/2}$ and thus $\tau_b \simeq 60$. For the highest resolution tested, i.e. $N_v = 64$, the upper limit of $t = T_R/2$ in estimating γ corresponds to $t = 44.7$. The poor performance of some schemes at higher resolution, e.g. the `VL` scheme is worse at higher resolutions, may therefore be due to the breakdown in the validity of the linear model used to estimate the percentage errors.

Table 4.1: Percentage errors in the damping rate γ for each scheme for the linear Landau damping test with $N_x = 32$

N_v	`FB`	`VL`	`Compact`	`FCT`	`PPM`	`PPM1`
16	16	15	47	70	4.7	3.7
32	2.6	1.6	3.3	10	2.2	0.038
64	0.32	6.0	5.1	28	1.7	0.13

All of the codes (for the 32×32 resolution) conserve energy to within 0.01%.

They also all conserve total mass to machine precision and the largest total momentum recorded (which ought to be zero) for any of the simulations is 3×10^{-7}. So the disparity in the results presented in Table 1 is not due to a simple lack of conservation. Indeed, there are a number of features of the various codes which are highlighted by this test. These relate to the order of the schemes and the dissipation inherent in each approach.

Linear Landau damping is a useful test of Vlasov solvers as the fine-scale structuring which is caused by phase-mixing is known to generate a perturbed distribution function, f_1 which varies as $f_1 \sim \exp(ikvt)$. Hence for each v there will come a time when the perturbed distribution function has an effective wavelength of twice the grid spacing. For the `FB` method numerical dissipation would then be at its largest. Since the gradients are of $f_0 + f_1$, where f_0 is the equilibrium Maxwellian distribution, the gradients calculated are never large enough for f to become negative. This will be shown below to be false for more stringent Vlasov test problems. Thus for linear Landau damping the numerical dissipation inherent in the `FB` method is sufficient to thermalize the fine-scale structuring without introducing negative f. However, there is no guarantee that individual x or v direction advection sweeps are monotonicity preserving. These results show that this is not a major problem for the linear Landau test as clearly the `FB` method gives an accurate result. Replacing the centered gradient used in `FB` with a van Leer limited gradient has only a minor effect on the results as can be seen from the `VL` results.

The results from the `Compact` code show that it is clearly worse than the lower order `FB` method. Since this is essentially a linear problem one would normally expect higher order schemes to give more accurate results. However, there is less intrinsic dissipation in the `Compact` method and it therefore encounters problems when the fine-scale structuring approaches the grid size. At this stage the need to fit a high order polynomial through rapidly oscillating values leads to large false gradients and these must be removed by the filtering. This filtering affects the linear properties of the damped mode, as can be seen at about $t = 20$ in Figure 4.1. It is this which causes the averaged Landau decay rate to be inaccurate. The averaging used to find the damping rates in Table 1 will thus be different if averaged over $T_R/4$ instead of $T_R/2$. Using $T_R/2$ has the advantage that schemes which do not maintain

linear decay for long enough lose out on this test. It may be possible to achieve better results for the `Compact` method by more carefully choosing the filtering scheme. Since the `Compact` method cannot be recommended for other reasons, which are outlined in the conclusions, we have not investigated this possibility further.

The `FCT` method gets the Landau decay correct initially but the limiters used in the algorithm prevent the fundamental from decaying after about $t = 30$ on the $(32, 64)$ grid. Using the average over $T_R/2$ as the measure of accuracy as in Table 1 shows that the FCT limiters make this scheme the worst for the linear Landau problem.

By far the most accurate scheme is `PPM1`. This is a natural generalisation of the `FB` method and it is therefore not surprising that it performs so well on this problem bearing in mind the success of the `FB` method. As with `FB` the `PPM1` scheme is accurate for this test but does not guarantee that individual x or v direction advection sweeps are monotonicity preserving. Including the standard monotonicity preserving limiters give the results presented for `PPM`. This limiting does degrade the accuracy of the scheme for this test but still gives results which are considerably more accurate than either the `FCT` or `Compact` methods.

4.6.2 Bump on tail instability

This test studies the evolution of an unstable bump on tail electron distribution. The ions are stationary, $L_x = 2\pi/0.3$, $v_e^{max} = 8$ and the initial electron distribution function is

$$f(x, v) = f_{b.o.t}(v)(1 + \alpha \cos(kx))$$

where the bump on tail distribution is

$$f_{b.o.t}(v) = \frac{n_p}{\sqrt{2\pi}} exp\left(-\frac{1}{2}v^2\right) + \frac{n_b}{\sqrt{2\pi}} exp\left(-\frac{1}{2}\frac{(v - v_b)^2}{v_t^2}\right)$$

For these tests we take $n_p = 0.9$, $n_b = 0.2$, $v_b = 4.5$, $v_t = 0.5$, $\alpha = 0.04$ and $k = 0.3$. This distribution function is unstable and leads to a rapid increase in the electric field. As all of the schemes have dissipation of some sort (implicit for `FB`, filtering for `Compact` and primarily through limiters for `FCT` and `PPM`) the system will eventually damp the fine-scale structures and be attracted to a stable phase space hole. Before considering the structure of the phase space hole formed by each scheme, it's worth

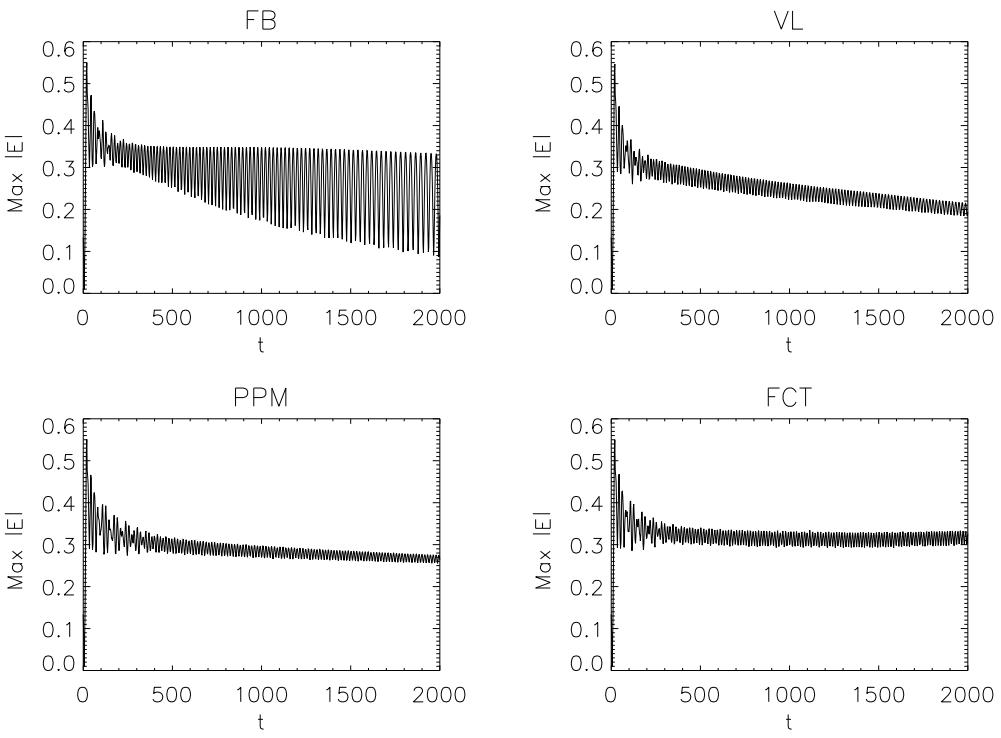

Figure 4.2: Time evolution of $|E|_{\max}$ for the bump on tail test on a $(128, 128)$ grid.

looking closely at the evolution of the maximum value of the absolute magnitude of the electric field, $|E|_{\max}$, against time. Figure 4.2 show the evolution of $|E|_{\max}$ for four schemes with a resolution of $(N_x, N_v) = (128, 128)$.

The result from the `FB` code at this resolution stands out as clearly in error. This is confirmed in Figure 4.3 where these tests are repeated with a $(512, 512)$ grid for the `FB` and `PPM` methods. This verifies that the results obtained on a $(128, 128)$ grid for the high order limited schemes are indeed reliable.

When a van Leer limited gradient is added to the `FB` method, i.e. the `VL` code, the false large oscillations in $|E|_{\max}$ are removed as can be seen from the plot in Figure 4.2. Since this scheme is formally lower order than either the `FCT` or `PPM` method the mean value of $|E|_{\max}$ is dissipated more quickly. Results from the `Compact` scheme are similar to those already presented for the `PPM` scheme.

Now that the distribution function can contain large gradients and complex structures (unlike the linear Landau damping test) the lack of monotonicity and

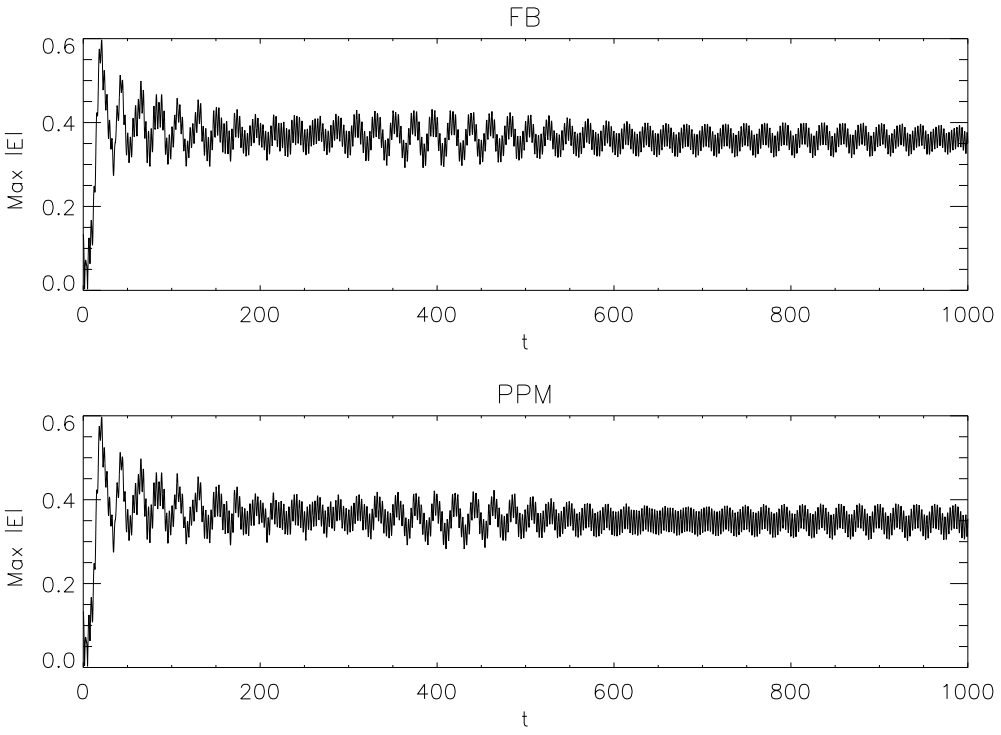

Figure 4.3: Time evolution of $|E|_{\max}$ for the bump on tail test on a $(512, 512)$ grid. On this finer grid the `FB` results are in line with those of the `PPM` method, confirming that the `FB` results on the (128,128) grid (see Fig. 4.2) are in error.

positivity is more significant. To quantify this Figure 4.4 shows the evolution of the fractional change in the discrete kinetic entropy, $S(t)$, for some of the schemes on $(128, 128)$ and $(512, 512)$ grids. Here $S(t) = -\sum f_i \log_e(g_i)$ where the sum is over all points on the computational grid and $g_i = \max(f_i, 10^{-64})$ is used to avoid taking the logarithm of negative f. Plotted in Figure 4.4 is the fractional change $\delta S = (S(t) - S(0))/S(0)$. On the $(128, 128)$ grid both the `FB` and `Compact` schemes immediately lead to a decrease in $S(t)$. The scale has been chosen to allow easy comparison between schemes and resolutions so the `FB` and `Compact` lines on the $(128, 128)$ grid actually go off the bottom of the scale. They continue to decrease approximately linearly for the duration of the simulation, although this is not shown. It is therefore not simply the lack of positivity which is responsible for the oscillation in $|E|_{\max}$ growing for the `FB` method in Figure 4.2 as the `Compact` scheme also has regions of negative f but does not show signs of growth in the

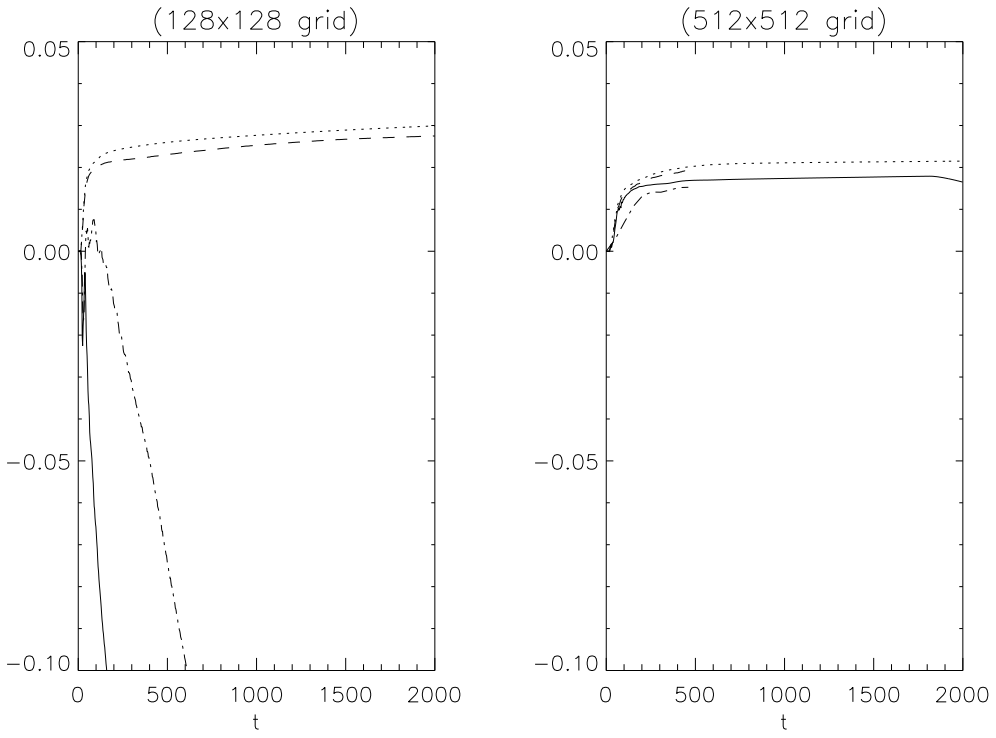

Figure 4.4: Time evolution of the fractional change in discrete kinetic entropy for the bump on tail test with resolution $(128, 128)$ and $(512, 512)$. The solid line is for `FB` dotted line is `PPM`, dashed line is `FCT` and the dash-dotted line is `Compact` .The `FCT` and `Compact` time series end prematurely at the high resolution solely because of the long time taken to generate them.

oscillations of $|E|_{\max}$. Also fixing the lack of monotonicity in the `FB` approach with van Leer limiters removes the growth in $|E|_{\max}$ and makes $S(t)$ monotonically increasing. The problems inherent in the `FB` method therefore do not stem from the formal order of the scheme but must result from an incorrect handling of short scale-lengths. Since `FB` performs well on a $(512, 512)$ grid it seems likely that for this particular test problem there is a critical scale-length which must be handled correctly, i.e. without introducing false maxima and minima, before reliable answers are obtained. All of the limited schemes automatically guarantee that they do not introduce false extrema, irrespective of the resolution, show no growth of $|E|_{\max}$ and only have increasing kinetic entropy.

In order to quantify the results from the bump-on-tail test problem we have run the `PPM`, `FCT`, `Compact`, `FB` and `VL` codes on a $(512, 512)$ grid up to $t = 500$

and then for each of the schemes calculated $\bar{f}(v_j) = \sum_i f(x_i, v_j)/N_x$. To remove any biasing in the solutions the average of this over all schemes is taken to be the accurate solution, $\bar{f}^{\rm acc}$, and this is then used to find the L_1 norm of the error for each of the schemes on lower resolutions, where $L_1 = \sum_j |\bar{f}(v_j) - \bar{f}^{\rm acc}(v_j)|/N_v$.

Table 4.2: L_1 errors for each scheme for the bump-on-tail test

(N_x, N_v)	`Compact`	`PPM`	`FCT`	`FB`	`VL`
(32,32)	0.017	0.010	0.0072	0.030	0.018
(64,64)	0.0025	0.0049	0.0036	0.014	0.011
(128,128)	0.00060	0.0016	0.0011	0.0038	0.0033
(512,512)	0.00052	0.00039	0.00033	0.00058	0.00026

The results of this analysis are shown in Table 2 which includes the results on the $(512, 512)$ grid to show that all codes converge to the same answer and that the L_1 norm estimates for courser grids are not biased strongly by a lack of convergence. However the result for the `Compact` scheme on a $(128, 128)$ grid is too close to the variance in the results used to find $\bar{f}^{\rm acc}$ to be used as anything other than a rough estimate. These results confirm that the `FCT` and `PPM` methods are of about the same accuracy as are the `FB` and `VL` methods. However, unlike the linear Landau damping test the results here follow the formal accuracy of the schemes with the best results being from the higher order schemes and the low order schemes (`FB` and `VL`) being more diffusive. This can be seen in Figure 4.5. We focus on the height of the bulk peak and the feature at $v \approx 5$. Both of these are better reproduced by the higher order (i.e. the `PPM`) method. However, it should be remembered that while the `Compact` scheme gives accurate results based on the L_1 norm of the error it gives poor results if the kinetic entropy is used as the measure of accuracy.

Shaded surface plots of f are also useful in determining the properties of these schemes. Figure 4.6 shows such plots, on a (512,512) grid, for the whole x domain but is restricted to $v_e > 0$ as this is the side in which a phase space hole forms. All of the schemes are broadly similar except for two notable features. Firstly the phase space hole is not in the same place for the `FB` method as in the others. This is not purely an effect of the order of the schemes as the `VL` method does not agree with the `FB` method. The second important point is that the higher order schemes

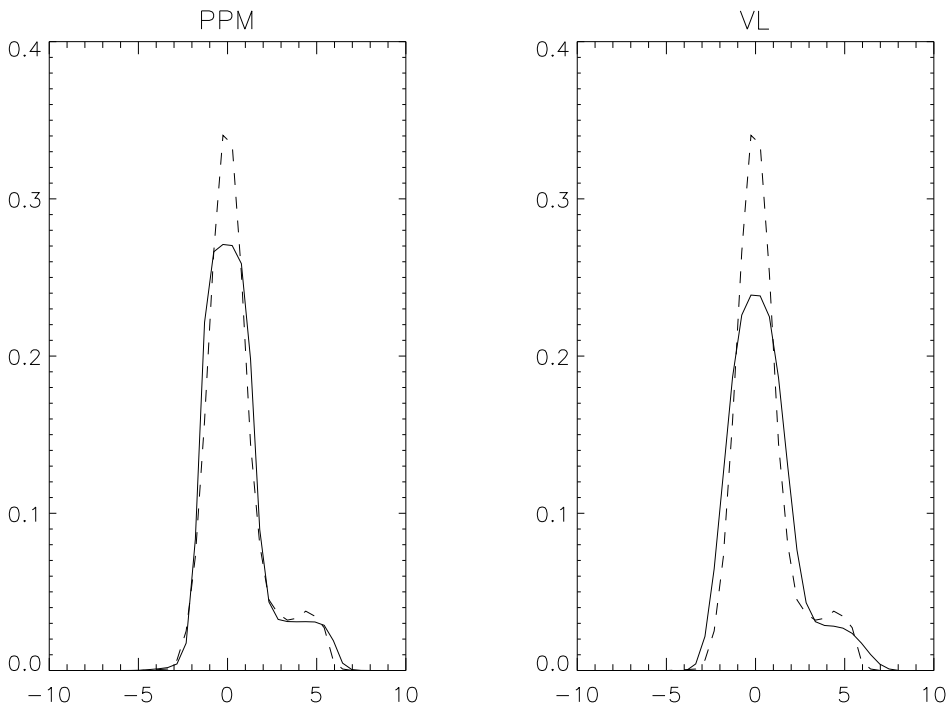

Figure 4.5: Spatially averaged $\bar{f}$ for the (third order) `PPM` and (second order) `VL` methods. The dashed line is $\bar{f}^{\rm acc}$ defined from an average of the (512,512) grid results and the solid lines are the results from the (32,32) grids. We note that the bulk peak and the feature at $v \approx 5$ are both somewhat better reproduced by the higher order (i.e. the `PPM`) method. In particular, the velocity gradient in the region of the bump $v \approx 5$ is better reproduced by `PPM` than `FB` . This feature is important because the gradient in that region makes an important contribution to the drive or growth of modes with that phase velocity (see e.g. Eq. 2.55).

do, as expected, show more detail in the vicinity of the hole. However, while the `PPM` method has a smooth solution the `FCT` solution shows signs of terracing. This well-known problem with FCT approaches will be discussed in more detail in the next section.

On lower resolutions the advantages of the `PPM` method are more apparent as can be seen in Figure 4.7 which compares it to the `VL` method on a (64,64) grid. This is a demonstration of the kind of accuracy one would expect when resolving small scale structures on more complex problems.

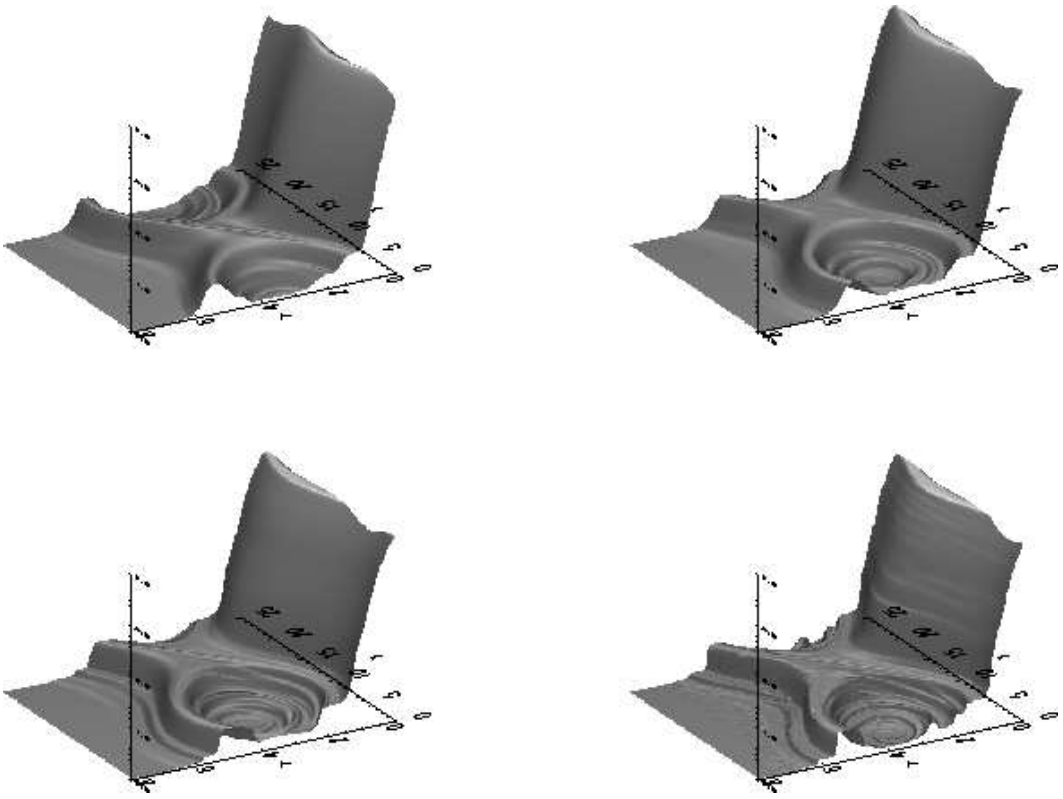

Figure 4.6: Bump on tail phase space holes at $t = 500$ with a (512,512) grid for the `FB` (top left), `VL` (top right), `PPM` (bottom left) and `FCT` (bottom right) methods. Shown are shaded surfaces of f for the whole of x but with only $0 < v_e < 8$. The `FB` result has the hole in a different place. As we would expect, the higher order methods (`PPM` and `FCT`) show more phase space structure.

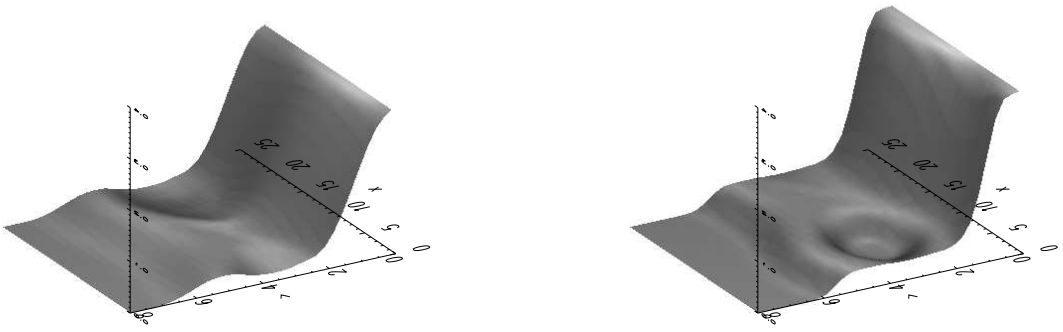

Figure 4.7: Repeat of Figure 4.6 on a (64,64) grid for the `VL` (left) and `PPM` (right) methods.

4.6.3 Ion-acoustic turbulence

Here the motivation is to compare the results from the different schemes not for a single well-defined mode but for a turbulent spectrum. The problem chosen is the onset and saturation of the ion-acoustic instability. The initial conditions are $L_x = 2\pi/0.05$, $v_e^{max} = 8$, $M_r = 1000$ and the ion distribution function is defined at all spatial grid points to be

$$f_i = \left(\frac{M_r}{2\pi}\right)^{1/2} \exp\left(-\frac{M_r}{2} v_i^2\right)$$

The electrons are setup as a drifting Maxwellian such that

$$f_e = (1 + a(x)) \left(\frac{1}{\sqrt{2\pi}}\right) exp\left(-\frac{1}{2}(v_e - U_e)^2\right)$$

where $U_e = -2$ and

$$\begin{aligned} a(x) = 0.01(\sin(x) &+ \sin(0.5x) + \sin(0.1x) + \sin(0.15x) + \sin(0.2x) \\ &+ \cos(0.25x) + \cos(0.3x) + \cos(0.35x))) \end{aligned}$$

The intention here is to provide initial conditions which are clear so that anyone wishing to repeat the tests with other codes may do so easily. This motivated the choice of $a(x)$ to be fixed and not a low level random noise.

This choice of initial conditions leads to an unstable growth of ion-acoustic waves. The electric field fluctuations which are established lead to a transfer of momentum from the electrons to the ions. This is seen in a plot of the difference of ion and electron fluid speeds, u_i and u_e respectively, in Figure 4.8. On the higher resolution tests all schemes agree on the decay rate. On the lower resolution tests there is a clear discrepancy in the time of onset of the decay. In this regard the `PPM` and `FCT` methods are more accurate since the higher order approach more accurately resolves the linearly unstable ion-acoustic modes and thus the initial growth of the fluctuating electric field responsible for the momentum transfer. Estimating the asymptotic value of $|u_i - u_e|$ from the (512,512) results alone is not helpful due to the low value predicted by the `FCT` scheme. However, we can rule out the `FCT` result by looking at shaded surface plots of f_i at $t = 2000$ in Figure 4.9. These show f_i in the whole of the x domain but only $v_i < 0$. Clearly from these plots the `FCT` scheme has clipped the maximum severely and similar plots of f_e show that the terracing,

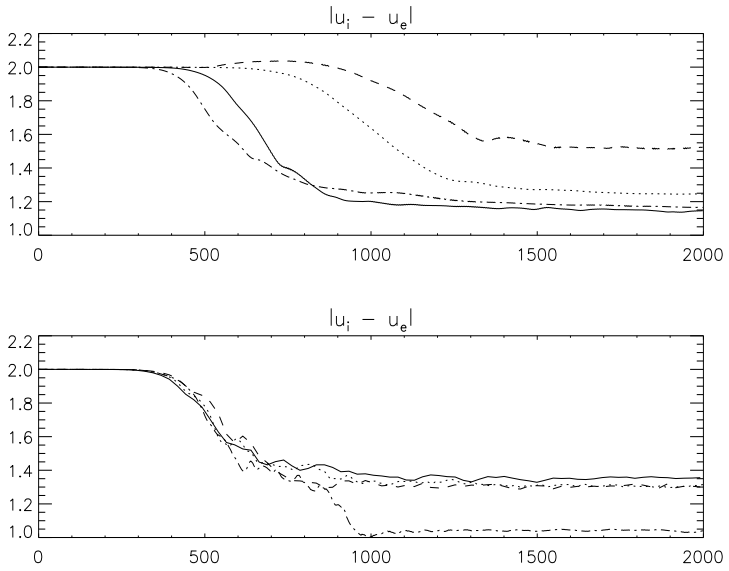

Figure 4.8: Evolution of the $|u_i - u_e|$ for the `PPM`, `FB`, `VL` and `FCT` schemes computed using two grid resolutions. In both plots the solid lines are `PPM`, dotted lines are `VL` and dashed lines are `FB` and dot-dashed lines are `FCT`. The upper figure is on a (64,64) grid and the lower figure is on (512,512).

already hinted at in Figure 4.6, is now far more pronounced. We use these facts to rule out the high resolution `FCT` results and conclude that the estimated final value of $|u_i - u_e|$ is 1.35, from the average of the `PPM` and `VL` results. On the (64,64) grid results of Figure 4.8 there is little difference in the accuracy of the `FB` and `PPM` in estimating the asymptotic value of $|u_i - u_e|$. `PPM` is however more accurate in determining the time dependence of $|u_i - u_e|$.

4.6.4 Summary of Vlasov-Poisson test results

In this section a series of test problems for conservatively differenced, fixed Eulerian grid based Vlasov solvers have been presented. All of the codes have adopted the dimensional splitting approach as introduced by Cheng and Knorr [CK76]. This is an efficient mechanism for solving Vlasov problems as each of the spatial and velocity advection sweeps are at constant speed. The central issue is then how best to solve for each of these 1D steps. What qualifies as a 'best' technique is not however a straightforward question when dealing with Vlasov solvers. Ideally any

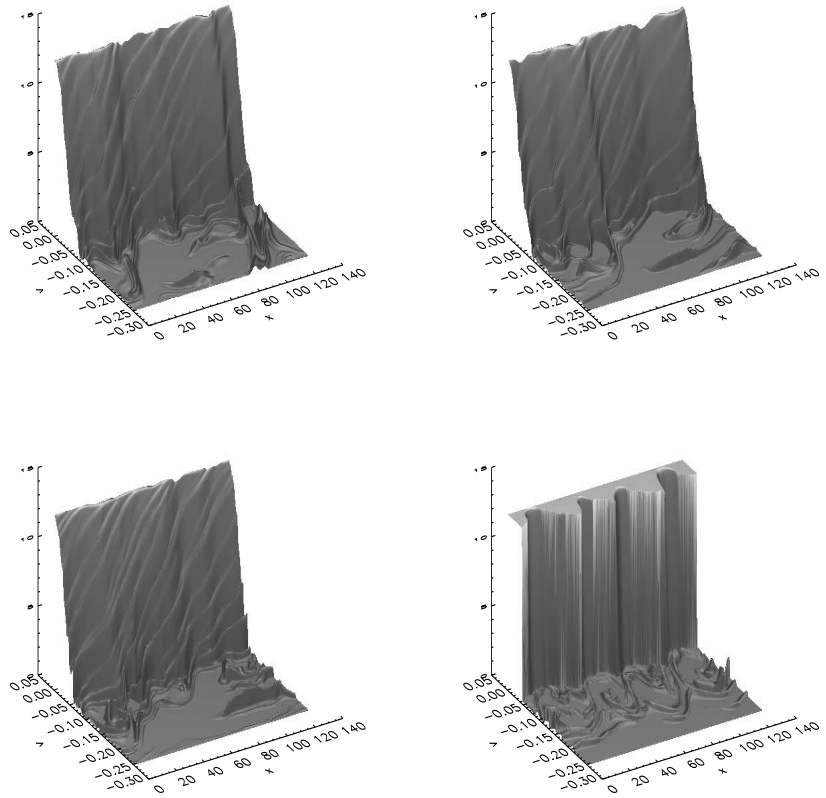

Figure 4.9: Ion acoustic turbulence test at $t = 2000$ with a (512,512) grid for the `FB` (top left), `VL` (top right), `PPM` (bottom left) and `FCT` (bottom right) methods. Show are shaded surfaces of f_i for the whole of x but with only $-8 < v_i < 0$

Vlasov solver should maintain positivity, actually the solution is bounded for all time by the initial maximum and minimum of f, and the advection steps should be monotonicity preserving. Determining how important these two conditions are in a quantifiable way for these test problems is a central focus of this work. The other major concern of this work has been the treatment of the fine-scale structure in f which arises naturally in many Vlasov problems. Treatment of the fine-scales (actually their averaging, smoothing or filtering) is intimately related with maintaining monotonicity.

Using Cheng and Knorr's [CK76] time splitting scheme as a common template for all of the tests allows us to isolate issues of performance and accuracy solely to the choice of advection algorithm. We have compared second order spatially accurate schemes (`FB` and `VL`), third/fourth order schemes (`PPM` and `FCT`) and a sixth order compact scheme (`Compact`). Some of these maintain monotonicity and positivity by geometrical construction (`VL` and `PPM`) while others achieve this by flux limiting (`FCT`). The schemes which are not positivity or monotonicity preserving (`FB` and `Compact`) must use filtering or smoothing to remove fine-scale structures. This has been applied in the `Compact` scheme, which fails all of the tests without it, but not to the `FB` method. However the `FB` method does work, even without smoothing, on some of the problems and gives some useful insight into the numerical problems associated with Vlasov solvers. If the `FB` method were to be used for Vlasov research it must of course be employed coupled with smoothing as for example in [Fij99].

The test problems were chosen to represent the most common applications of Vlasov solvers. The Landau problem tests the ability to deal with linear problems. The bump-on tail test highlights different codes accuracy in dealing with a single unstable mode and the formation of a stable BGK mode. Finally the ion-acoustic turbulence test was used to compare the codes when the physics was being driven by a broad spectrum of unstable modes. In all these tests it is also important to measure the relative costs of the numerical schemes. For 100 steps on the (512,512) grid bump-on-tail problem the runtimes were; `FB` 8 seconds, `VL` 14 seconds, `PPM` 19 seconds and `Compact` 164 seconds. These timings were on a Compaq EV6 500Mhz CPU with 4MB cache using the Compaq F90 compiler. As always with such comparisons one needs to be cautious that such scalings will remain true on all architectures

but the general picture is probably reliable. The fastest is the FB method without smoothing or averaging. Adding limiters to the FB method (it does not work for all problems on all grid sizes without this) approximately doubles the runtime. Going from second order VL to third order PPM increases the runtime by about 50% and the Compact scheme is almost an order of magnitude slower.

The linear Landau test showed that all schemes get a reasonably accurate decay of the fundamental mode. The percentage errors in Table 1 are mostly dominated by the departure from exponential decay at later times. The FB and Compact schemes maintain the decay, although in the Compact solution the filtering required for this scheme to work changes the decay rate at around $t = 25$. Both the PPM and FCT schemes give an accurate initial decay but then maintain an approximately constant level for $|E_1|$ until T_R. However, since $|E_1|$ has decreased by about three orders of magnitude before this happens, i.e. $|E_1| \simeq 10^{-5}$ this is not seen as a major drawback for practical situations.

The bump-on-tail test showed the problem of using schemes of second order or higher which do not correctly handle the fine-scale structures. Here the FB method fails on a (128,128) grid as can be seen in Figure 4.2. Some evidence that it is the handling of these fine-scales that is most important, in contrast to merely maintaining positivity, is given by the results from the Compact scheme. This also has regions with $f < 0$, see Figure 4.4, but in all other quantifiable ways gives a satisfactory result. The same is true of the FB method when suitable smoothing is included [Fij99]. The remainder of the results in Section 4.6.2 emphasis the advantages of going to higher order schemes with the VL method needing approximately double the number of points in x and v to achieve the same detail in the structure of the BGK mode as the PPM method.

The final test re-emphasized the advantages of using higher order schemes in getting accurate results for $|u_i - u_e|$ as a function of time. More importantly this test showed that the FCT approach actually gives the wrong answer due to excessive clipping of the maxima of f_i and terracing of f_e. Hence maintaining positivity and monotonicity by themselves are not sufficient to guarantee an accurate solution. It is vital that the limiter, or indeed smoother etc. for the FB method and variants, dissipates the fine-scale structure in a physically realistic way. This is true of the

PPM method and the filtering in Compact.

From all of these observations and results we draw the following conclusions

- Applying geometric limiters to the FB method, i.e. VL, maintains positivity and monotonicity and removes the need for additional smoothing or averaging.
- The PPM method, which also needs no additional averaging, is approximately 50% slower than VL but gives results which are quantitatively more accurate.
- The FCT approach fails on the ion-acoustic test due to excessive clipping and terracing and therefore cannot be recommended as a method for solving Vlasov problems.
- The Compact method is the most accurate on the bump-on-tail test when using the L_1 norm of the error as the measure of accuracy. However it does not maintain $f > 0$, has very poor entropy results on course grids and is approximately an order of magnitude slower than PPM.
- Keeping $f > 0$, while desirable, is less important than correctly treating the fine-scale structures which form in Vlasov solutions.

Since maintaining monotonicity and positivity is a property of linear advection and implementing it in Vlasov solvers removes the need for additional averaging or smoothing the optimal scheme from these tests is the PPM method. It consistently gives accurate results (it is formally third order accurate) and is only 50% slower than VL. It is over two times slower than FB but comparison with VL is more appropriate as the FB method needs additional smoothing to be reliable, which would of course slow it down. For VL to achieve the same resolution of phase space as PPM it requires double the number of points in x and v which increases the VL runtime by a factor of eight. A similar conclusion has been reached previously regarding the benefits of higher order geometric reconstructions by Filbet et al. [FSB01]. However, in that paper Filbet et al. consider only third order reconstructions and the limiters applied maintain positivity but not monotonicity. The results presented in here are the first to implement the full PPM algorithm to Vlasov solvers and demonstrate the robustness and accuracy of such an approach.

The high order compact scheme is the most accurate in the L_1 norm analysis of the bump-on-tail problem. However, as has already been mentioned, this scheme only works with compact filtering of the fine-scale structures. `Compact` also requires more memory as it is only stable with third, or higher, order Runge-Kutta which requires extra temporary arrays. All of the other schemes, including `PPM`, require storage only for f_e and f_i so it is hard to recommend `Compact` despite its increased accuracy for the bump-on-tail test. Note also that the filtering made `Compact` less accurate than `PPM` for the Landau test. The fact that filtering in this way does work, although allowing $f < 0$, raises important questions about applying filtering or smoothing to Vlasov solvers. It may be possible to choose a filtering which improves further the accuracy of `Compact`. We have not attempted this as the runtime and memory costs make `Compact` impractical. Considerable effort has in the past been applied to the filtering/smoothing problem of other schemes. Most noticeable amongst these is the filtering technique first introduced by Klimas [Kli87] which has the advantage of correctly evolving the fields, i.e. low order moments are correct, by solving directly for the smoothed/filtered distribution function. This approach has only been shown to work in Fourier-Fourier transform space and thus does have the disadvatge of requiring multiple FFT's per step. We have concentrated on fixed Eulerian grid based solvers and the merits of the `PPM` method compared to a suitably filtered Fourier-Fourier transform space solver remains an open question. A physically and mathematically justifiable approach, such as the `PPM` geometric reconstruction, is successful in treating fine-scales, automatically maintains positivity and monotonicity and requires no additional smoothing. Unless a scheme which employs smoothing/filtering can be shown to be more accurate than this third order approach it is difficult to see a strong case for using filtering on fixed Eulerian grid Vlasov solvers. Such techniques will however continue to be vital for semi-Lagrangian methods where 2D generalizations of a dimensionally unsplit `PPM` method would be cumbersome. We do however note that the third order positive, but not monotonicity preserving, scheme used by Filbet et al. [FSB01] has already been shown to be almost as accurate as cubic spline semi-Lagrangian methods anyway. There is therefore a very strong case for the third order accurate, positivity and monotonicity preserving `PPM` method proposed in this chapter.

4.7 Solving DCE instead of Poisson

There has been some interest [HF01] in developing codes that solve DCE Eq. (2.32) instead of Poisson's equation since using DCE leads to a scheme that is easier to parallelize efficiently. We note, however, that using DCE may introduce a systematic error into the electric field which might significantly change the results. It is therefore important to check that the results we obtain are independent of which of the two equations we use to close the system algebraically. The time splitting that we use is:

$$\Phi_Y^{\Delta t}\left[Z_0\right] = \Phi_{Y_1}^{\frac{1}{2}\Delta t} \circ \Phi_{Y_3}^{\frac{1}{2}\Delta t} \circ \Phi_{Y_2}^{\Delta t} \circ \Phi_{Y_3}^{\frac{1}{2}\Delta t} \circ \Phi_{Y_1}^{\frac{1}{2}\Delta t}\left[Z_0\right] + \mathcal{O}\left(\Delta t^3\right) \tag{4.19}$$

where Y_1, Y_2 are defined by Eq. (4.4) and

$$Y_3[(f,E)] = \left(0, \int v(f-\bar{f})dv\right) \tag{4.20}$$

Explicitly, this notation is equivalent to:

- Evolve $\partial_t f + v\partial_x f = 0$ for a time $\Delta t/2$.
- Solve $\partial_t E = \int v(f-\bar{f})dv$ for a time $\Delta t/2$
- Evolve $\partial_t f + E\partial_v f = 0$ for a time Δt.
- Again solve $\partial_t E = \int v(f-\bar{f})dv$ for a time $\Delta t/2$
- Finally evolve $\partial_t f + v\partial_x f = 0$ for a time $\Delta t/2$.

Here we make a comparison between using DCE and Poisson's equation by considering the bump-on-tail example, with one species, using the `PPM` method on a (128,128) grid up to $t = 2000$.

At each time step, we compare the fundamental component of the electric field obtained from DCE to the value computed from Poisson's equation for the system at that time. The relative error in $|E_1|$ is always less than 0.15% and the phase error is always less than 0.001 radians. In Figure 4.10, we have plotted $|E|_{\max}$ against $t \in [1900, 1903]$ both for the time stepping method given here and for the time stepping method used in the comparison of the different advection algorithms. We note that there is a time-shift of 0.05, which corresponds to approximately 1% of the period of a plasma oscillation. We conclude that there is no significant loss of

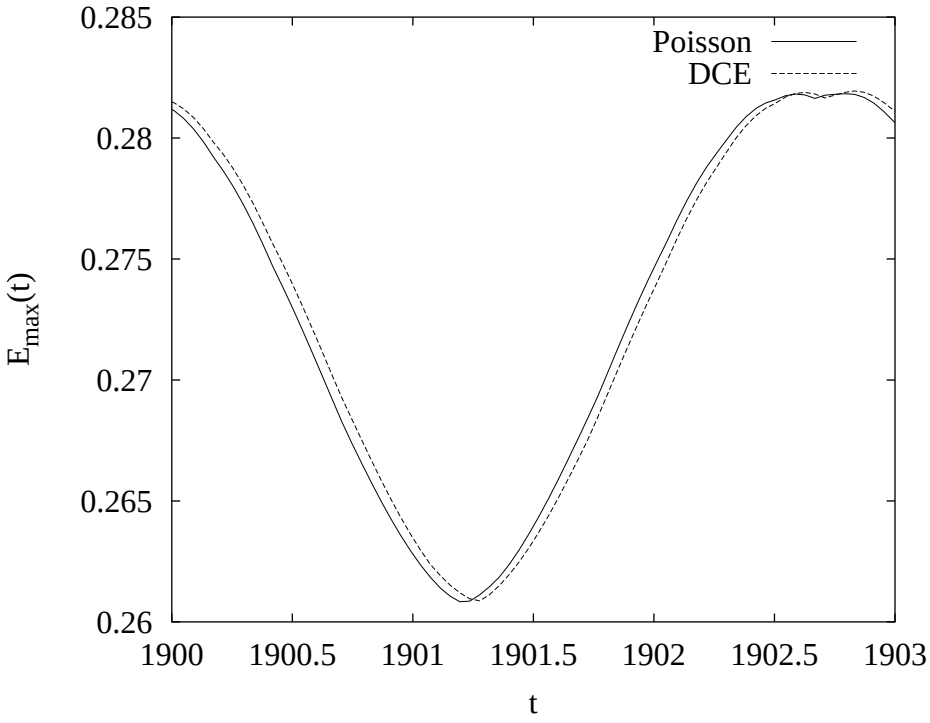

Figure 4.10: $|E|_{\max}$ vs. time for the bump-on-tail example. The solid line is from the method used when comparing the various advection algorithms; the dashed line solves DCE. We note that the only discernible difference is a time shift of about 1% of a plasma oscillation period.

accuracy. However, for electrostatic problems one should still of course check the accuracy against Poisson as a diagnostic.

4.8 Numerical solution of the VM(BB) equations

4.8.1 Time splitting

In this thesis we wish to solve the Berk-Breizman augmentation of the Vlasov-Maxwell equations, the so-called VM(BB) system, as given by Eqs. (2.33) and (2.39). As discussed in Sec. 2.2.2, for these equations there exists no analogue of Poisson's equation, and so it is not possible to calculate the electric field $E(x,t)$ as a function of a given distribution function $f(x,v,t)$. We are therefore obliged to solve for $E(x,t)$ in a way similar to the DCE Eq. (2.32). We redefine

$$Y_3[(f,E)] = \left(0, \int v(f-\bar{f})dv - \gamma_d E\right) \tag{4.21}$$

and introduce

$$Y_4[(f,E)] = (-\nu_a(f-F_0), 0) \tag{4.22}$$

The time splitting then used is

$$\Phi_Y^t\left[Z_0\right] = \Phi_{Y_1}^{\frac{1}{2}\Delta t} \circ \Phi_{Y_4}^{\frac{1}{2}\Delta t} \circ \Phi_{Y_3}^{\frac{1}{2}\Delta t} \circ \Phi_{Y_2}^{\Delta t} \circ \Phi_{Y_3}^{\frac{1}{2}\Delta t} \circ \Phi_{Y_4}^{\frac{1}{2}\Delta t} \circ \Phi_{Y_1}^{\frac{1}{2}\Delta t}\left[Z_0\right] + \mathcal{O}\left(\Delta t^3\right) \tag{4.23}$$

This scheme reduces to the Vlasov-DCE scheme Eq. (4.19) in the case $\nu_a = \gamma_d = 0$. Benchmarking of this scheme against other numerical methods is not possible because no other quantitative results exist.

4.8.2 The recurrence phenomenon

If the electric field is very small, the particles are *free streaming*: they experience phase space advection only in the x-direction. Therefore the phase space line $v = v_j$ keeps recovering the same state with period $T = L/v_j$. Since we are working on a discrete uniform Eulerian grid, the system then develops an unphysical temporal periodicity under this spatial advection: the phase space lines are regularly spaced at a distance Δv, so the entire grid is periodic with the period $T_R \equiv L/\Delta v$ (i.e. the period of the phase space line with smallest non-zero $|v|$). This phenomenon is known as *recurrence* and T_R is called the *recurrence time*. Note first that recurrence only

occurs when the particles are free streaming. This is the case when the advection in the v-direction is small compared to the advection in the x-direction so that $\overline{E}\,T_R \lesssim \Delta v$, where $\overline{E}$ is some measure of the average electric field amplitude. Second, the addition of distribution reconstitution to the Vlasov equation gives our system a finite memory of length $\sim \nu_a^{-1}$. So, given our other choices of numerical parameters, in particular $N_v = 1025$, the recurrence time $T_R = 1344\,\omega_p^{-1}$, and the numerics will only show this recurrence if $\overline{E} \lesssim 5 \times 10^{-5}$ and $\nu_a \lesssim 2 \times 10^{-3}$.

4.8.3 Choice of coding parameters

We wish to test whether our choice of coding parameters applied for the production of results in Chapter 3 is appropriate. In particular, we wish to check that the numerical results converge as the resolutions in space, velocity, and time are increased. Moreover we wish to verify that the values that we have chosen, specifically $N_x = 128$, $N_v = 1025$, and $\Delta t_{\max} = 0.1$, give sufficient accuracy that the correct qualitative features of the time series $A(t)$ corresponding to any particular value of the physical parameters (γ_d, ν_a) are recovered and moreover that some degree of quantitative convergence has been achieved. The success of this second objective is measured here only by eye; there has been no attempt to quantify rates of convergence, for example.

In this section we display the results for three particular parameter values that are chosen to be near the boundary between two regions of different qualitative behaviour, for which it is helpful to recall the structure of the bifurcation diagram shown in Fig. 3.2. This choice is made since (a) it is important that the choice of coding parameters should not govern the qualitative nature of the system's behaviour or the bifurcation path in parameter space, and (b) we presume that it is on category boundaries that the system behaviour is most sensitive to the choice of coding parameters. We remark that the condition for the robustness of the categorization diagram Fig. 3.2 is much less stringent than the condition for the quantitative convergence of time series.

No attempt has been made here to perform benchmarking within the chaotic region. The observed sensitive dependence on initial conditions implies that one would not expect to achieve quantitative agreement between time series generated

using different coding parameters over long times, even at very high resolutions. However, one might certainly expect measures of chaos (such as the Lyapunov exponent measured in 3.2.2) to be robust.

4.8.3.1 Steady state / damped boundary $(\gamma_d, \nu_a) = (3.1, 0.01)$

This point is chosen to be near the linear stability threshold $\gamma = 0$ as computed from the dispersion relation Eq. (2.53). It is just in the steady state region. The growth rate $\gamma = -0.0015$ is calculated using the dispersion relation solver presented in Appendix C.2 We refer to the results shown in Fig. 4.11. (The underline in each of these figure captions denotes on which side of the relevant boundary the point lies.)

(a) Varying the velocity space resolution. At $N_v = 257$, recurrence effects dominate and the wrong qualitative behaviour is produced. At $N_v = 513$, the correct qualitative behaviour is recovered, but there is still significant quantitative error. As N_v is further increased, the time series converges quantitatively at the resolution of the graphical plot.

(b) Varying the temporal and spatial resolutions. We find that neither an increase in the numerical parameter $\Delta t_{\max}$ (corresponding to an increase in $\lambda_{\max}$: refer to Eq. (4.12)) nor an increase in the number of points in x space leads to a significant quantitative change in $A(t)$. We infer that our choices of $\Delta t_{\max} = 0.1$ and $N_x = 128$ provide sufficiently high resolution for convergence.

4.8.3.2 Steady state / damped boundary $(\gamma_d, \nu_a) = (1.5, 0.07943)$

This point is similarly near the line $\gamma = 0$; however in this case it is just in the damped region. In this case, we know from the dispersion relation Eq. (2.53) that the growth rate $\gamma = 1.50 \times 10^{-3}$ and therefore that for long times $A(t) \propto \exp(-0.0030t)$. We refer to Fig. (4.12).

(a) We vary N_v and observe that the correct growth rate and amplitude are both recovered correctly even at the relatively low resolution $N_v = 257$. (b) We change the time step and observe that, whilst decreasing it has no effect on the result, increasing it produces the wrong growth rate. Therefore our chosen time step $\Delta t_{\max} = 0.1$

is sufficient. We also recover the correct growth rate with half the number of grid points. So we infer convergence at $N_v = 257$, $N_x = 64$, $\Delta t_{\max} = 0.1$.

4.8.3.3 Periodic / chaotic boundary $(\gamma_d, \nu_a) = (2.8, 0.01122)$

Although we believe that the point $(\gamma_d, \nu_a) = (2.8, 0.01122)$ is within the periodic region, it is very near the boundary with the region of chaotic behaviour. As a result, we expect more difficulty in achieving quantitative convergence. We refer to Fig. (4.13).
(a) Reducing $N_v \to 513$ produces a clear quantitative difference in the time series. We make the judgement that the increase $N_v \to 2049$ does not produce a significant quantitative change. (b) Increasing the time step $\Delta t_{\max} \to 0.25$ produces a significant qualitative error. Neither decreasing the time step nor doubling the number of spatial grid points has a significant quantitative effect and so we infer convergence at $N_v = 1025$, $N_x = 64$, $\Delta t_{\max} = 0.1$.

4.8.3.4 Within the periodic region $(\gamma_d, \nu_a) = (1.0, 0.03162)$

For points (γ_d, ν_a) far from category boundaries, we find even better quantitative agreement between time series generated with differing coding parameters than for the points near category boundaries considered here. This final example demonstrates this with a point in parameter space from the middle of the periodic region. We refer to the results shown in Fig. (4.14). The time series are phase-shifted by a best-fit choice of τ. The reductions in $N_v \to 257$ and $\Delta t_{\max} \to 0.25$ require a phase shift that is judged to be significant. So we infer convergence at $N_v = 513$, $N_x = 64$, $\Delta t_{\max} = 0.1$.

4.9 Summary of numerical development

The objective of this chapter has been to develop an algorithm that efficiently and accurately solves the VM(BB) system of equations (2.33) and (2.39). A large part of this chapter is devoted to the development of a fast accurate solver of the Vlasov-Poisson system of equations. A systematic comparison of a range of Eulerian grid based solvers shows that the Piecewise Parabolic Method (PPM) of Colella and

Woodward [CW84] is ideal as the advection solver component of such a method. This is then applied through the Strang time splitting employed in the original work by Cheng and Knorr [CK76].

We proceeded in Sec. 4.7 to show that we obtain no inconsistency in our results by solving for DCE instead of Poisson. In Sec. 4.8 we showed how the time splitting may naturally be adapted to solve the full VM(BB) system of equations. The choice of coding parameters that we have used for our main simulations in Chapter 3 has then been rigorously tested.

We stress again that whilst the emphasis here has been to develop an accurate and computationally cheap solver of the VM(BB) equations, the methodology that we have employed is applicable to a wide range of advection-based problems.

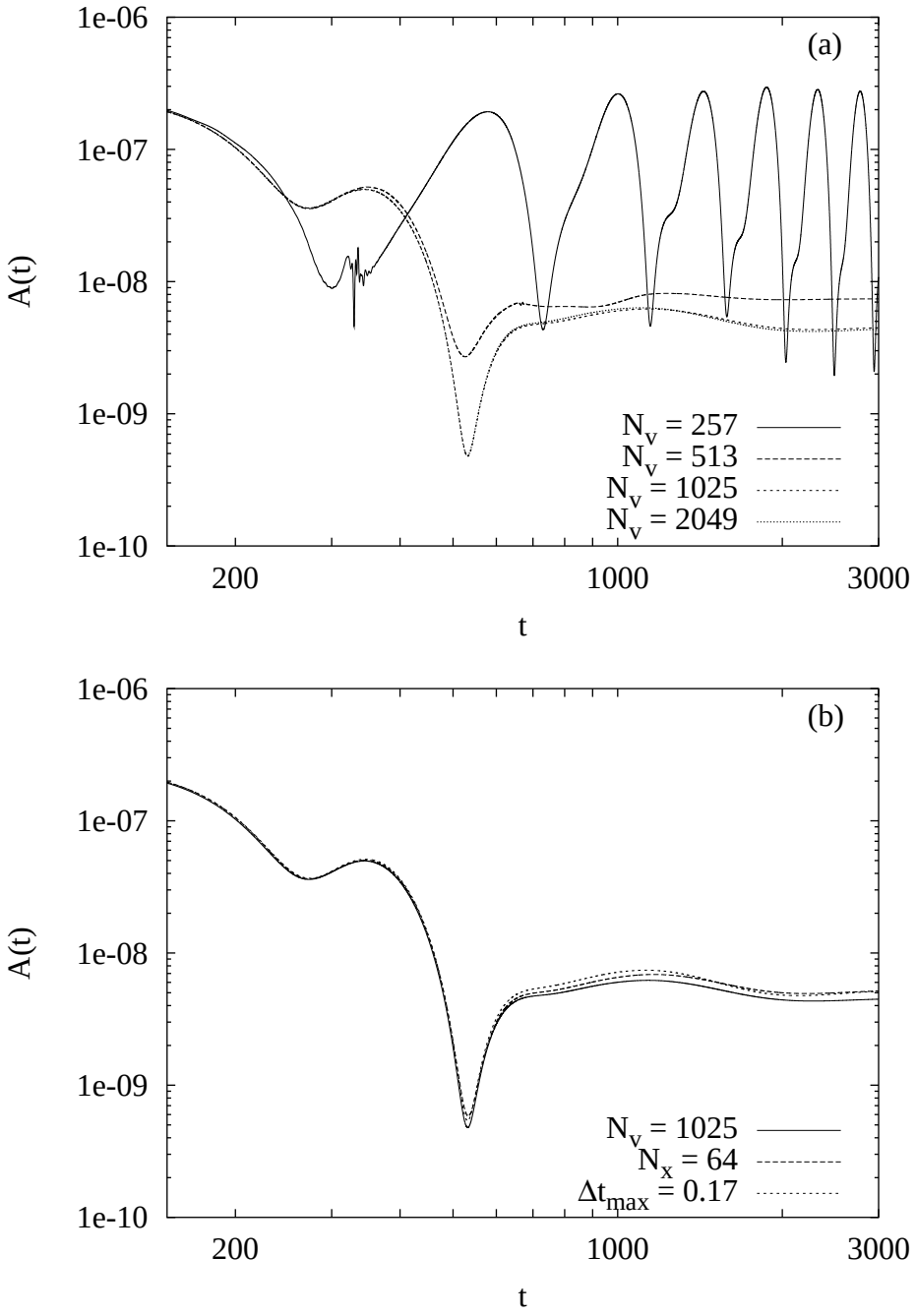

Figure 4.11: Benchmarking near the steady state / damped boundary at $(\gamma_d, \nu_a) = (3.1, 0.01)$. Time series $A(t)$ for physical parameters $(\gamma_d, \nu_a) = (3.1, 0.01)$ and various coding parameters. (a) We vary N_v and observe quantitative convergence (at the resolution of the plot) at $N_v = 1025$. (b) We lower the resolution in both time and space and observe no significant quantitative change in solution. Again we infer convergence.

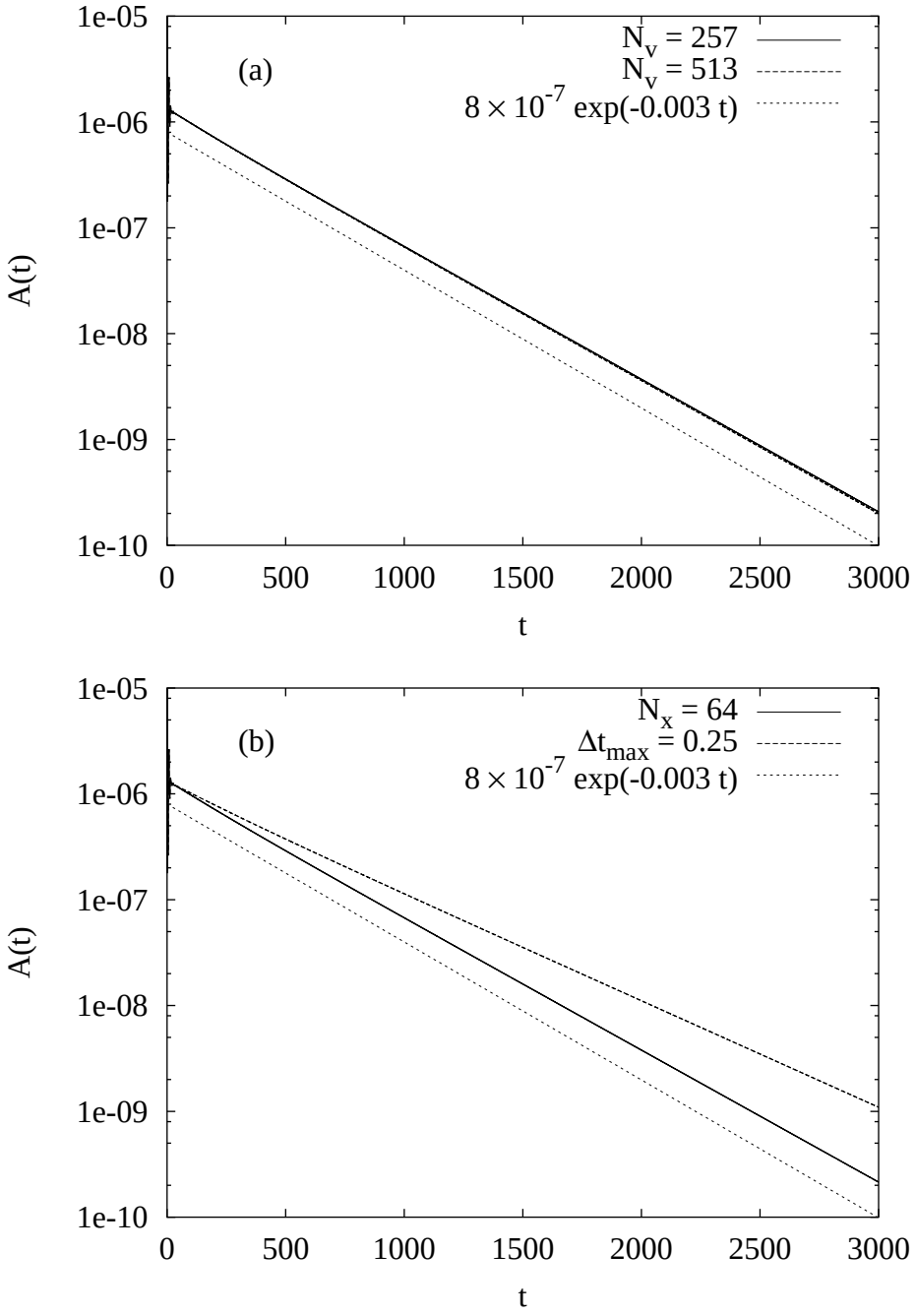

Figure 4.12: Benchmarking near the steady state / damped boundary at $(\gamma_d, \nu_a) = (1.5, 0.07943)$. We vary various coding parameters and infer convergence at $N_v = 257$, $N_x = 64$, $\Delta t_{\max} = 0.1$. In this case we know that the system is linearly stable with growth rate $\gamma = -1.5 \times 10^{-3}$; the numerical results agree well with this result.

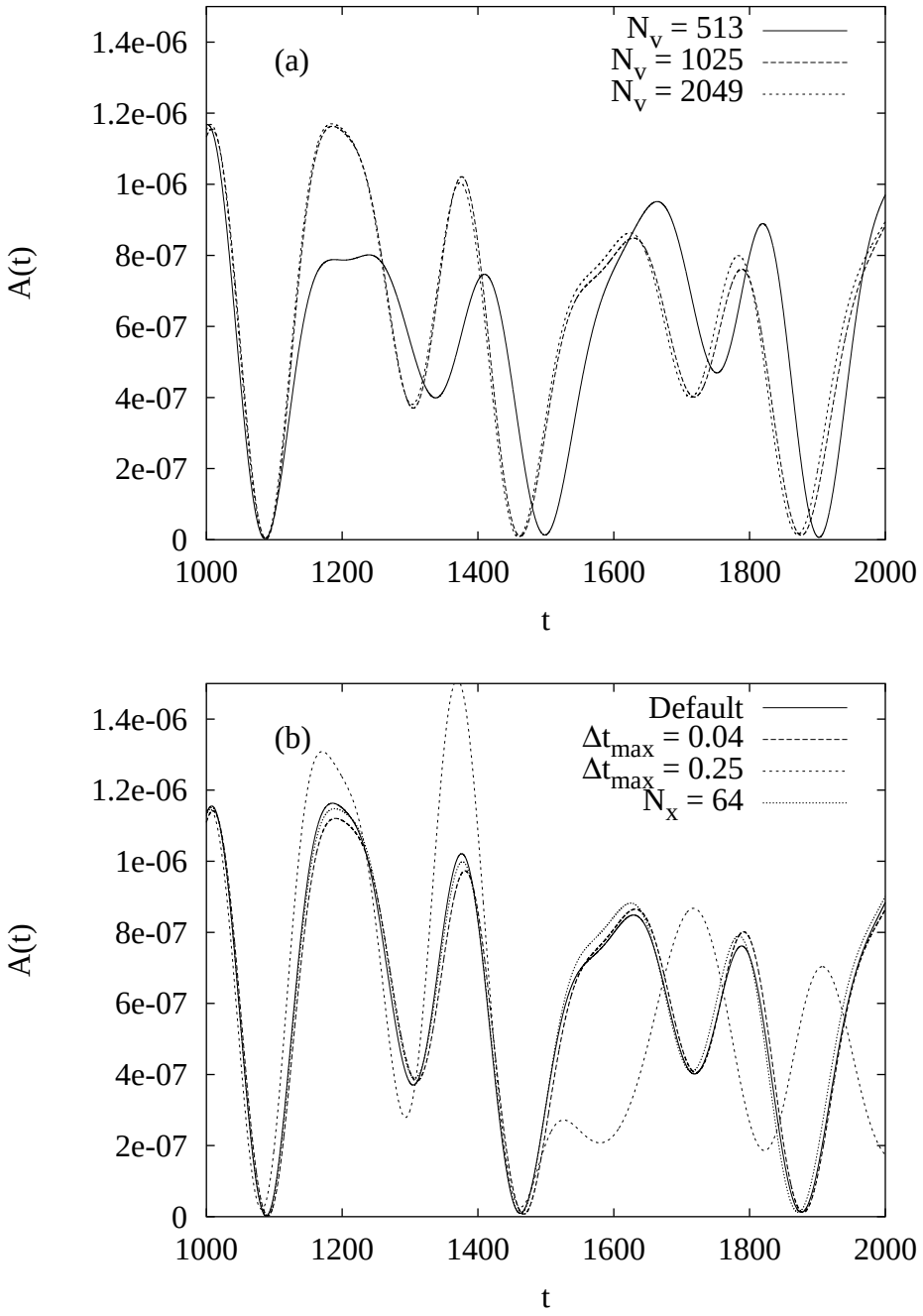

Figure 4.13: Benchmarking near the periodic / chaotic boundary at $(\gamma_d, \nu_a) = (2.8, 0.01122)$. Near the chaotic region we expect particular difficulty in achieving quantitative convergence. However, we observe convergence in this case at $N_v = 1025$, $N_x = 64$, $\Delta t_{\max} = 0.1$.

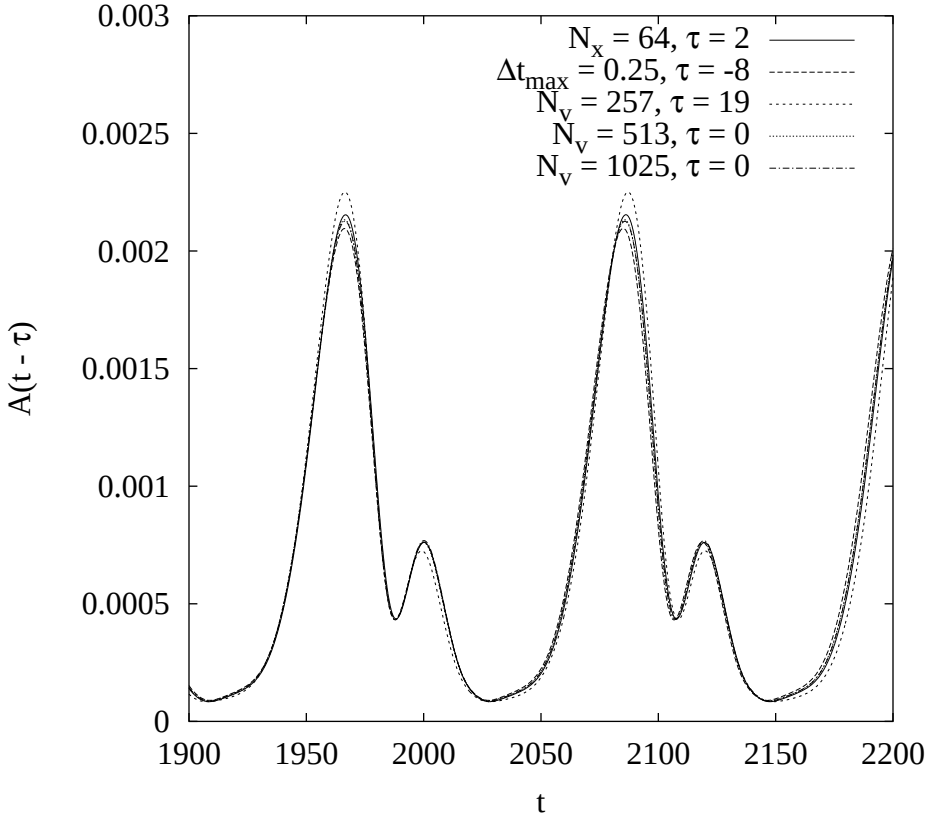

Figure 4.14: Benchmarking within the periodic region at $(\gamma_d, \nu_a) = (1.0, 0.03162)$. The phase shift τ is chosen for best fit between the various time series. Varying the various parameters, we observe convergence at $N_v = 513$, $N_x = 64$ and $\Delta t_{\max} = 0.25$.

Chapter 5

Conclusions

In this thesis, we have reported new numerical techniques which, using modern computer resources, make it possible to generate accurate self-consistent solutions for the fully nonlinear Berk-Breizman augmentation of the Vlasov-Maxwell system. For the first time, the full range of (ν_a, γ_d) parameter space has been explored, and the corresponding system behaviour categorised into one of four types: damped, steady state, periodic and chaotic. This classification is achieved by analysing the time dependence of the total electric field energy. Further physical understanding is aided by the deployment of numerical diagnostics in (x, v) phase space. Our results confirm Berk and Breizman's qualitative expectations of the system's time evolution, but our work permits precise definition of the boundaries between different types of behaviour and even quantitative analysis within regions of similar behaviour. Examples include the measurement of the periods of periodic orbits, investigation of global bifurcations such as period doublings, and the computation of Lyapunov exponents within the chaotic regime.

The key to this progress has been the development of a Vlasov-solver algorithm based on timestep decomposition of the equations according the Strang splitting formula, followed by computation of the separate advections by the Piecewise Parabolic Method. We have shown in Chapter 4 that this method performs extremely well in systematic competition with other Eulerian grid schemes as a solver of the Vlasov-Poisson system. The Vlasov equation leads to filamentation in phase space, with the creation of structures of ever decreasing size. This method's correct treatment of

short scale lengths, and in particular its properties of montonicity preservation and non-accentuation of already existing extrema, lead to it being both computationally affordable and numerically accurate. Correct treatment of short scales further implies that the correct large-scale phase space structure (such as the size and position of phase space holes) is correctly obtained at much lower grid resolutions than is possible with other methods (see Fig. 4.7).

The algorithm on which the Vlasov-Poisson code is based is easily adapted to solve related problems. In this thesis, we have shown that the DCE can be used reliably instead of Poisson's equation without the introduction of significant phase errors (Sec. 4.7). It was then simple for us to adapt the algorithm further to solve the full system of equations in which we have captured the Berk Breizman Augmentation of the Vlasov-Maxwell system (Sec. 4.8.1). My VM(BB) code has been extensively benchmarked to show that the coding parameters used in simulations provide sufficient resolution for numerical convergence (Sec. 4.8.3).

Previous work relating the BB model to experimental data has been restricted to using a linear truncation of the BB model that allows for the presence of only one mode. The approach described in this thesis will permit a direct quantitative and systematic comparison of the results predicted by the fully nonlinear BB model and data from experiment. Preliminary work [FBB$^+$98, HFS00] has already shown that there is a connection between the behaviour of the BB model and the behaviour of experimental systems; however the quantitative nonlinear comparison made possible by our code is important because, instead of just being able to decide the effective (γ_d, ν_a) values of the experimental plasma, it will be possible to start making deductions about mechanisms at work in the real plasma based on observations of the structure of the simulated system's phase space. However, this is not a simple extension of the current work. Rather, it will involve extensive analysis of the available experimental data and then feeding the resulting understanding of the experimental physics into the choice of VM(BB) parameters.

The combination of efficient numerical algorithms and physically well-motivated paradigmatic models opens the way for the direct quantitative investigation of other phenomena observed in fusion plasmas that are not currently well understood. For example, it is thought that plasma characteristics such as energy transport can only

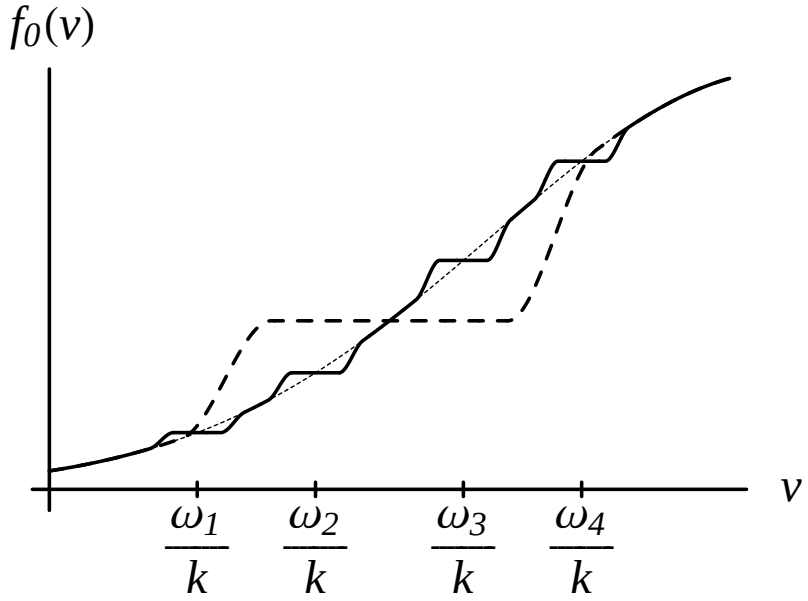

Figure 5.1: *A multiple mode scenario.* The solid line shows how the spatially averaged distribution function $f_0(v)$ is characteristically flattened at the phase velocities of several modes; the original distribution is shown by the light dotted line. We wish to establish under what conditions, and in particular at what mode amplitudes, might the distribution represented by the solid line cascade into the distribution shown by the dashed line. This is of interest because the mode overlap and subsequent cascade leads to a large energy release (related to the area between the various curves) from the energetic particle population.

be understood in a theoretical picture that allows for the presence of many spatial modes. Such a scenario is illustrated in Fig. 5.1: the excitation of four modes leads to the flattening of the particle number distribution in velocity space at the four phase velocities (represented by the solid line). However, as the amplitudes of the modes increases, the mode flattening may stretch across the entire velocity region (as shown by the dashed line). Such mode overlap releases a large amount of energy from the particles to the wave modes. This problem of many modes has in the past been addressed by, for example, continuum harmonic approximations such as quasilinear theory [VVS61, DP62]. (Quasilinear theory makes a random phase approximation whose general applicability is not well proven. Indeed, it has been shown that there are regimes in which the results provided by quasilinear theory require significant correction [LP80].) In principle the current code could already be used for multiple mode simulations by massively increasing the spatial period. However, as the resulting run times would be very long and impractical, a significant amount of code development would be required to address these problems. This

would probably involve parallelisation across many processors and optimisation such as avoiding calculating the dynamics of strongly damped modes.

We have described in this thesis a fully nonlinear self consistent model of the interaction between energetic particle populations and collective wave modes, and how we have quantitatively solved and analysed this model. We predict that other experimentally observed phenomena such as chirping [M$^+$99] could be described by models similar in framework to this BB model [BBC$^+$99]. We envisage that quantitative comparison between these theoretical models and experiment will lead to an ever deeper understanding of the physics of burning fusion plasmas.

Appendix A

Small parameter integral identities

The following small parameter integral identities are used without proof within this thesis.

$$\lim_{\epsilon \to 0} \int_{-\infty}^{+\infty} \frac{\epsilon \, g(x)}{\epsilon^2 + x^2} \, dx = \pi \, \mathrm{sgn}(\epsilon) \, \mathrm{g}(0) \tag{A.1}$$

$$\lim_{\epsilon \to 0} \int_{-\infty}^{+\infty} \frac{\epsilon \, x^2 \, g(x)}{\left(\epsilon^2 + x^2\right)^2} \, dx = \frac{\pi}{2} \, \mathrm{sgn}(\epsilon) \, \mathrm{g}(0) \tag{A.2}$$

$$\lim_{\epsilon \to 0} \int_{-\infty}^{+\infty} \frac{\epsilon^3 \, g(x)}{\left(\epsilon^2 + x^2\right)^2} \, dx = \frac{\pi}{2} \, \mathrm{sgn}(\epsilon) \, \mathrm{g}(0) \tag{A.3}$$

$$\lim_{\epsilon \to 0} \int_{-\infty}^{+\infty} \frac{\epsilon \, x \, g(x)}{\left(\epsilon^2 + x^2\right)^2} \, dx = \frac{\pi}{2} \, \mathrm{sgn}(\epsilon) \, \mathrm{g}'(0) \tag{A.4}$$

Appendix B

Numerical categorisation of time series

We wish to classify a large number of time series into one of the following four types: damped, steady state, periodic, and chaotic. (Refer to Sec. 3.2.1 for definitions of these categories.) The series that we are interested in happens to be electric field energy density, as defined by Eq. (3.3), against time. However, the procedure that we describe below is effective for any bounded $A(t)$. (Recall that we show in Sec. 2.2.3 that the electric field energy is bounded.

Sometimes it is possible to categorise a time series into one of these four types by eye. However, we wish the categorisation to be quantitative. Moreover, we need to classify over a thousand time series. This calls for an automated system.

Suppose the computational time step of the simulation is Δt. Then the raw data from the simulation is a series of ordered pairs $(j\Delta t, A(j\Delta t))$, $0 \leq j \leq j_{\max}$, where $j_{\max}$ is determined by the end time of the simulation. A subset of this raw data is used in the categorisation procedure: in the analysis we consider a time window $0 < t_{\min} < t_{\max}$, with $A(t)$ sampled with a period δt (which may be larger than the computational time step Δt). We aim to choose $t_{\min}$ sufficiently large that transient behaviour has died out before the start of the analysis time window. We note that this is not always possible to guarantee and discuss below the impact of this difficulty on categorisation. We have $t_{\max} - t_{\min} = (N-1)\,\delta t$ for some positive integer N so that we have N data points $A_j = A(t_{\min} + j\,\delta t)$ where $j \in [0, N-1]$.

Then we can define

- the mean value $\langle A \rangle = \sum_{j=0}^{N-1} A_j/N$,
- the global minimum $A_{\min} = \min_j\{A_j\}$ and maximum $A_{\max} = \max_j\{A_j\}$,
- the set labelling local minima $S_{\min} = \{j \in \mathbb{N} : A_j < \min\{A_{j\pm1}\}\}$, and similarly $S_{\max}$.

For any $0 < j \leq N/2$, we define the correlation window length N_j to be the largest integer such that $N_j \leq N/j$ and the window function by $B_i = A_l - \langle A \rangle$ where $l = N - (i \mod N_j)$. We then write the two point correlation function as

$$R_j = \left(\sum_{i=0}^{N_j-1} B_i B_{i+j} \right) / \left(\sum_{i=0}^{N_j-1} B_i^2 \right) \tag{B.1}$$

The overall correlation $R = \max_j\{R_j\}$. We save time in the computation of R by making the assumption that R_j will be large only when j corresponds to the time difference between local extrema. We have chosen $t_{\min} = 1000\,\omega_p^{-1}$, $t_{\max} = 3000\,\omega_p^{-1}$ and $\delta t = 0.5$. We then proceed through the following decision tree:

1 `IF` $\langle A \rangle < \epsilon_1 = 10^{-12}$ `THEN` *damped*

2 `ELSE IF` $A(t)$ is monotonic `AND` $(A_{\max} - A_{\min})/\langle A \rangle < \epsilon_2 = 5\%$ `THEN` *steady state*

3 `ELSE IF` $A(t)$ is monotonically decreasing `THEN` *damped*

4 `ELSE IF`

(a) the system is oscillating about a value to which it is tending (i.e. for all $i > j$, $(i, j \in S^{\min} \Rightarrow A_i < A_j)$ `AND` $(i, j \in S^{\max} \Rightarrow A_i > A_j)$), `OR`

(b) $(A_{\max} - A_{\min})/\langle A \rangle < \epsilon_3 = 1\%$, `OR`

(c) $(A_{\max} - A_{\min}) < \epsilon_4 = 10^{-9}$

`THEN` *steady state*

5 `ELSE IF` $R > 1 - \epsilon_5 = 75\%$ `THEN` *periodic*

6 `ELSE IF` number of extrema is not less than four `THEN` *nonperiodic*

We note that this decision tree cannot correctly classify periodic behaviour if the period is greater than half the length of the sampling window - it is either classified as nonperiodic or not classfied at all. Similarly, working with simulations of finite time, we cannot guarantee that the system will not at some later time settle down to a periodic orbit, for example. Given more computer time, one could run longer simulations and increase the threshold correlation value. As a result, the choice of correlation threshold is the most difficult to make. The behaviour of the system on the border of the periodic region is complicated, as discussed above, and we are subject to both the numerical issues just outlined.

Despite these limitations, this algorithm provides a fast, efficient and reliable method for automating the quantitative categorisation of time series. In Chapter 3, it is an invaluable tool for the fast generation of Figures 3.2 and 3.13.

Appendix C

Dispersion relation solvers

Both the algorithms described in this appendix are solvers of the linearised Landau-type dispersion relation Eq. (2.53) (restated below in Eq. (C.1).

The first algorithm tells us about the linear stability of a particular system. That is, given a distribution $F_0(v)$ and BB parameters γ_d and ν_a, it tells us the most positive growth rate γ and associated frequency ω. This algorithm is used to calculate growth rates in Sections 4.6.1 and 4.8.3.1.

The second algorithm calculates the linear stability threshold (i.e. the curve $\gamma = 0$) in (γ_d, ν_a) parameter space. It does this by being given a value for ν_a and then solving for γ_d and ω. It is used to generate the linear stability threshold curves in Figures 2.3 and 3.2.

The third section in this appendix describes the an integration routine with error checking. This routine is a critical component of both the dispersion relation solvers.

C.1 Dispersion relation solver I: solving for frequency ω and growth rate γ

Recall the dispersion relation Eq. (2.53) obtained for the Berk-Breizman augmentation to the Vlasov-Maxwell system of equations:

$$\gamma' + \gamma_d - i\omega' = \int_\Gamma \frac{v\, d_v F_0}{(\gamma' + \nu_a) + i\,(kv - \omega')}\, dv \tag{C.1}$$

where Γ is the appropriate Landau contour (see Clemmow & Dougherty [CD69] pp. 247-9). We recall also that this equation has many solutions (γ', ω'), but there exists a maximum γ' (which we denote by γ) for which a solution exists. The frequency corresponding to $\gamma' = \gamma$ we denote by ω. Given a parameter pair (γ_d, ν_a), we seek the solution (γ, ω).

We split Eq. (C.1) into real and imaginary parts, and into the parts from the real integral and from the pole, as

$$K(\gamma', \omega') \equiv \int_{-\infty}^{+\infty} \frac{(\gamma' + \nu_a)\ v\ d_v F_0}{(\gamma' + \nu_a)^2 + (kv - \omega')^2} dv + \Re(z) - \gamma' - \gamma_d = 0 \quad \text{(C.2)}$$

$$J(\gamma', \omega') \equiv \int_{-\infty}^{+\infty} \frac{(kv - \omega')\ v\ d_v F_0}{(\gamma' + \nu_a)^2 + (kv - \omega')^2} dv - \Im(z) - \omega' = 0 \quad \text{(C.3)}$$

where the contribution from the pole

$$z = \begin{cases} 0 & \text{if } \gamma' + \nu_a > 0, \\ \dfrac{2\pi v_\phi}{k} \left(\dfrac{dF_0}{dv} \right)_{v = v_\phi} & \text{if } \gamma' + \nu_a < 0. \end{cases} \quad \text{(C.4)}$$

and the (complex) "phase velocity" v_ϕ satisfies

$$k v_\phi = \omega' + i(\gamma' + \nu_a) \quad \text{(C.5)}$$

Our numerical method for the solution of this equation is based on finding intersections of the lines $K = 0$ and $J = 0$ in (γ', ω') space.

We begin by considering a rectangular region in phase space $\gamma_{\min} < \gamma' < \gamma_{\max}$, $\omega_{\min} < \omega' < \omega_{\max}$. Each side of this rectangle is divided into N_d subdivisions, creating N_d^2 rectanglar subregions. Such a region is illustrated in Fig. C.1; in this example $N_d = 4$. For each of the N_d^2 subdivisions (one of which is shaded in the figure), we evaluate $J(\gamma', \omega')$ and $K(\gamma', \omega')$ at each of its corners. (The integral terms are evaluated using the method described in Sec. C.3. However, we do not permit an attempt at evaluating the integrals below some chosen minimum value of $(\gamma' + \nu_a)$ since the number of nodes required becomes unreasonably large as $(\gamma' + \nu_a) \to 0$.)

Then we ask two questions:

1 Do all the corners of the subregion have values of K with the same sign?

2 Similarly for J.

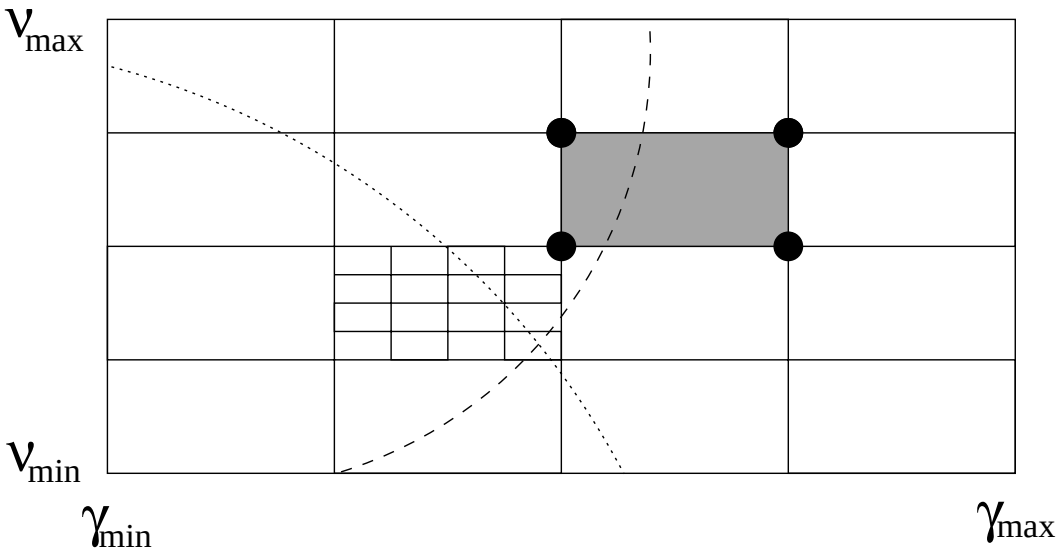

Figure C.1: A region in (γ', ω') space showing a shaded subregion and its corners (at which J and K are evaluated). Suppose that on the dotted line $K = 0$ and on the dashed line $J = 0$. Then the shaded subregion is discarded because K has the same sign at all its corners (even though J does not). The subregion below and to the right of it, however, has changes of sign of both K and J on its corners, and so it is subdivided as shown. At the next level, the bottom right of the subsubregions will be the only one not discarded.

If the answer to either question is "yes", then we discard the subregion. Otherwise we subdivide the subregion yet again (a subdivided subregion is illustrated in the figure) and repeat the process.

We stop either when no more subregions remain (in which case we say that no solution exists within the original rectangular region) or when the size of the subregions is less than some small tolerance size. Recall that we are interested in the solution with the most positive value of γ'. We note that

- if the first level of subregions is not sufficiently small, then this method may not find some solutions We choose $N_d = 100$ for the first level to minimise this being a problem; thereafter it is fastest to choose $N_d = 2$.

- if the size of the final level subregions is not sufficiently small, then this method may report solutions which do not exist, although this becomes increasingly unlikely as the tolerance value is decreased.

Despite these potential problems, in practice this two dimensional interval bi-

section method has shown itself to be a fast and reliable solver of the dispersion relation Eq. (C.1).

C.2 Dispersion relation solver II: solving for the linear stability threshold $\gamma = 0$

We wish to solve $\gamma = 0$, given $\nu_a > 0$, for unknowns ω and γ_d. In this case Eqs. (C.2) and (C.3) reduce to equations in the one variable ω':

$$K(\gamma_d, \omega') \equiv \int_{-\infty}^{+\infty} \frac{\nu_a \; v \; d_v F_0}{\nu_a^2 + (kv - \omega')^2} dv - \gamma_d = 0 \tag{C.6}$$

$$J(\gamma_d, \omega') \equiv \int_{-\infty}^{+\infty} \frac{(kv - \omega') \; v \; d_v F_0}{\nu_a^2 + (kv - \omega')^2} dv - \omega' = 0 \tag{C.7}$$

We note that the equation for J is independent of γ_d. So we solve $J = J(\omega') = 0$ by interval cutting (again choosing many subdivisions for the first cut and then fewer for later cuts) and then substitute for ω' into Eq. (C.6) to find γ_d. We use again the integration technique detailed in Sec. C.3. We record the solution ω' which maximises the corresponding value of γ_d.

C.3 An integration technique with error checking

All the dispersion relations in this appendix are of integral form. It is therefore crucial that we have a reliable and numerically efficient way of computing integrals, and in particular integrals of functions with large gradients. The method described here uses two forms of the trapezium rule to put a tolerance on the error of the numerically computed integral. If the error is too large, then we sample the function at more points. What makes this method efficient is that, as we move to higher resolution, we find that we have already sampled the function at many of the points about which we need to know.

Suppose we wish to know $\mathcal{I} = \int_a^b U(x)dx$. Then, choosing some $N \gg 1$ so that $\Delta x = (b-a)/N \ll 1$, the trapezium rule gives us

$$\mathcal{I}_1 = \Delta x \left[\frac{1}{2} U(x_0) + \sum_{n=1}^{N-1} U(x_n) + \frac{1}{2} U(x_N) \right] = \mathcal{I} + \mathcal{O}(\Delta x^3) \tag{C.8}$$

where $x_n = a + n\Delta x$. But if we shift all the nodes by $\Delta x/2$, then we can apply the trapezium rule again:

$$\mathcal{I}_2 = \Delta x \left[\frac{1}{8} U(x_{-\frac{1}{2}}) + \frac{7}{8} U(x_{+\frac{1}{2}}) + \sum_{n=1}^{N-2} U(x_{n+\frac{1}{2}}) + \frac{7}{8} U(x_{N-\frac{1}{2}}) + \frac{1}{8} U(x_{N+\frac{1}{2}}) \right] \quad \text{(C.9)}$$

$$= \mathcal{I} + \mathcal{O}(\Delta x^3) \quad \text{(C.10)}$$

If $|\mathcal{I}_1 - \mathcal{I}_2|$ is less than some tolerance value, then we say that the trapezium rule result has converged. Otherwise we double the number of sample nodes, i.e. $N \to 2N$, $\Delta x \to \Delta x/2$, and reevaluate $\mathcal{I}_1$ and $\mathcal{I}_2$.

Note that when we double the number of nodes, we take advantage of the fact that we have already computed for $\mathcal{I}_2$ almost all the values we need for the computation of $\mathcal{I}_1$ with double the number of points.

This method has the advantage of being extremely simple, as well as being robust to the choice of integrand.

Bibliography

[AHKM70] Thomas P. Armstrong, Rollin C. Harding, Georg Knorr, and David Montgomery. Solution of Vlasov's equation by transform methods. In *Methods in computational physics*, volume 9, pages 29–86. Academic Press, 1970.

[Arn89] V. I. Arnold. *Mathematical methods of classical mechanics*. Springer, second edition, 1989. See pp.68–70 for statement of Liouville's theorem.

[AV02] T. D. Arber and R. G. L. Vann. A critical comparison of Eulerian grid based Vlasov solvers. *J. Comput. Phys.*, 180(1):339–357, 2002.

[BB73] J. P. Boris and D. L. Book. Flux-corrected transport I: SHASTA - a fluid transport algorithm that really works. *J. Comp. Phys.*, 11:38–69, 1973.

[BB76] J. P. Boris and D. L. Book. Solution of continuity equations by the method of flux-corrected transport. In John Killeen, editor, *Methods in computational physics*, volume 16, pages 85–129. Academic Press, 1976.

[BB90a] H. L. Berk and B. N. Breizman. Saturation of a single mode driven by an energetic injected beam. I. Plasma wave problem. *Phys. Fluids B*, 2(9):2226–2234, 1990.

[BB90b] H. L. Berk and B. N. Breizman. Saturation of a single mode driven by an energetic injected beam. II. Electrostatic "universal" destabilization mechanism. *Phys. Fluids B*, 2(9):2235–2245, 1990.

[BB90c] H. L. Berk and B. N. Breizman. Saturation of a single mode driven by an energetic injected beam. III. Alfvén wave problem. *Phys. Fluids B*, 2(9):2246–2252, 1990.

[BBC+99] H. L. Berk, B. N. Breizman, J. Candy, M. Pekker, and N. V. Petviashvili. Spontaneous hole-clump pair creation. *Phys. Plasmas*, 6(8):3102–3113, 1999.

[BBP95] H. L. Berk, B. N. Breizman, and M. Pekker. Numerical simulation of bump-on-tail instability with source and sink. *Phys. Plasmas*, 2(8):3007–3016, 1995.

[BBP96] H. L. Berk, B. N. Breizman, and M. Pekker. Nonlinear dynamics of a driven mode near marginal stability. *Phys. Rev. Lett.*, 76(8):1256–1259, 1996.

[BBY92] H. L. Berk, B. N. Breizman, and H. Ye. Scenarios for the nonlinear evolution of alpha-particle-induced Alfvén wave instability. *Phys. Rev. Lett.*, 68(24):3563–3566, 1992.

[BBY93] H. L. Berk, B. N. Breizman, and H. Ye. Collective transport of alpha particles due to Alfvén wave instability. *Phys. Fluids B*, 5(9):3217–3225, 1993.

[BC01] P. C. Birch and S. C. Chapman. Detailed structure and dynamics in particle-in-cell simulations of the lunar wake. *Phys. Plasmas*, 8(10):4551–4559, 2001.

[BGK] P. L. Bhatnagar, E. P. Gross, and M. Krook. A model for collision processes in gases. i. small amplitude processes in charged and neutral one-component systems. *Phys. Rev.*, 94(3):511–525.

[BGK57] Ira B. Bernstein, John M. Greene, and Martin D. Kruskal. Exact nonlinear plasma oscillations. *Physical Review*, 108(3):546–550, 1957.

[BL91] C. K. Birdsall and A. B. Langdon. *Plasma physics via computer simulation*. IoP, 1991.

[BO99] A. V. Bobylev and T. Ohwada. On the generalization of Strang's splitting scheme. *Riv. Mat. Univ. Parma*, 6(2):235–243, 1999.

[But97] David R. Butenhof. *Programming with POSIX Threads*. Addison-Wesley, 1997.

[CD69] P. C. Clemmow and J. P. Dougherty. *Electrodynamics of particles and plasmas*. Addison-Wesley, 1969. See Chapter 8 for a discussion of Landau damping.

[CK76] C. Z. Cheng and G. Knorr. The integration of the Vlasov equation in configuration space. *J. Comput. Phys.*, 22:330–351, 1976.

[CW84] P. Colella and P. R. Woodward. The piecewise parabolic method (PPM) for gas-dynamical simulations. *J. Comput. Phys.*, 54:174–201, 1984.

[DP62] W. E. Drummond and D. Pines. Non-linear stability of plasma oscillations. *Nucl. Fusion 1962 Suppl. Pt 3*, pages 1049–1057, 1962.

[FBB+98] A. Fasoli, B. N. Breizman, D. Borba, R. F. Heeter, M. S. Pekker, and S. E. Sharapov. Nonlinear splitting of fast particle driven waves in a plasma: observation and theory. *Phys. Rev. Lett.*, 81(25):5564–5567, 1998.

[Fij99] E. Fijalkow. A numerical solution to the Vlasov equation. *Comput. Phys. Comm.*, 116:319–328, 1999.

[FSB01] F. Filbet, E. Sonnendrücker, and P. Bertrand. Conservative numerical schemes for the Vlasov equation. *J. Comp. Phys*, 172:166–187, 2001.

[Gle94] Paul Glendinning. *Stability, instability and chaos*. CUP, 1994.

[GMS94] Michel Goossens, Frank Mittelbach, and Alexander Samarin. *The LaTeX companion*. Addison-Wesley, 1994.

[HF01] R. B. Horne and M. P. Freeman. A new code for electrostatic simulation by numerical integration of the Vlasov and Ampère's equations using MacCormack's method. *J. Comp. Phys.*, 171:182–200, 2001.

[HFS00] R. F. Heeter, A. F. Fasoli, and S. E. Sharapov. Chaotic regime of Alfvén eigenmode wave-particle interaction. *Phys. Rev. Lett.*, 85(15):3177–3180, 2000.

[Kli87] A. J. Klimas. A method for overcoming the velocity space filamentation problem in collisionless plasma model solutions. *J. Comp. Phys.*, 68(1):202–226, 1987.

[Lan98] Culbert B. Laney. *Computational gasdynamics*. CUP, 1998.

[Lel92] Sanjiva K. Lele. Compact finite difference schemes with spectral-like resolution. *J. Comput. Phys.*, 103:16–42, 1992.

[LP80] G. Laval and D. Pesme. Breakdown of quasilinear approximation for incoherent 1-d Langmuir waves. *Phys. Lett.*, 80A(4):266–268, 1980.

[M+99] K. G. McClements et al. Physics of energetic particles in the START spherical tokamak. *Plasma Phys. Control. Fusion*, 41:661–678, 1999.

[Man97] G. Manfredi. Long-time behavior of nonlinear Landau damping. *Phys. Rev. Lett.*, 79(15):2815–2818, 1997.

[MPI] The Message Passing Interface (MPI) standard. `http://www-unix.mcs.anl.gov/mpi/`. See subdirectory `mpich/` for the MPICH implementation.

[OB01] Elaine S. Oran and Jay P. Boris. *Numerical simulation of reactive flow*. CUP, 2001.

[P+92] William H. Press et al. *Numerical recipes in C*. CUP, 1992. See Chapter 12: Fourier Transform Spectral Methods.

[PB95] P. J. Plauger and Jim Brodie. *Standard C: a reference*. Prentice Hall, 1995.

[Pea] T. J. Pearson. PGPLOT graphics subroutine library. `http://www.astro.caltech.edu/ tjp/pgplot/`.

[RCL93] Michael T. Rosenstein, James J. Collins, and Carlo J. De Luca. A practical method for calculating largest Lyapunov exponents from small data sets. *Physica D*, 65:117–134, 1993.

[Ros] Mike Rosenstein. The `L1D2` code for calulating largest Lyapunov exponents. `http://www.physionet.org/physiotools/lyapunov/l1d2/`.

[Sho79] M. M. Shoucri. Nonlinear evolution of the bump-on-tail instability. *Phys. Fluids*, 22:2038–2039, 1979.

[Spr] Julien Clint Sprott. Chaos and time series analysis. To be published by OUP in 2003.

[SRBG99] E. Sonnendrücker, J. Roche, P. Bertrand, and A. Ghizzo. The semi-Lagrangian method for the numerical resolution of the Vlasov equation. *J. Comp. Phys*, 149(2):201–220, 1999.

[Str68] G. Strang. On the construction and comparison of difference schemes. *SIAM J. Numer. Anal.*, 5(3):506–517, 1968.

[TLP] K. Theilhaber, G. Laval, and D. Pesme. Numerical simulations of turbulent trapping in the weak beam-plasma instability. *Phys. Fluids*, 30(10):3129–3149.

[VDB] H. X. Vu, D. F. DuBois, and B. Bezzerides. Transient enhancement and detuning of laser-driven parametric instabilities by particle trapping. *Phys. Rev. Lett.*, 86(19):4306–4309.

[VDR+03] R. G. L. Vann, R. O. Dendy, G. Rowlands, T. D. Arber, and N. d'Ambrumenil. Fully nonlinear phenomenology of the Berk-Breizman augmentation of the Vlasov-Maxwell system. *Phys. Plasmas*, 10(3):623–630, 2003. This paper was published between the submission and acceptance of this thesis.

[VVS61] A. A. Vedenov, E. P. Velikhov, and R. Z. Sagdeev. *Nucl. Fusion*, 1:82–100, 1961.

[W+97] K. L. Wong et al. Evolution of toroidal Alfvén eigenmode instability in Tokamak Fusion Test Reactor. *Phys. Plasmas*, 4(2):393–404, 1997.

[You82] D. L. Youngs. Time dependent multi-material flow with large fluid distortion. In K. W. Morton and M. J. Baines, editors, *Numerical Methods in Fluid Dynamics*, pages 273–285. Academic Press, 1982.